**MOLDOVA STATE UNIVERSITY**

With the rights of manuscript
UDC: 539.21

**COCEMASOV ALEXANDR**

# PHONON PROCESSES IN GRAPHENE AND SILICON-BASED NANOSTRUCTURES

**131.04 - COMPUTATIONAL PHYSICS AND MODELING OF PROCESSES**

**Doctor thesis in physics**

| | |
|---|---|
| Scientific supervisor: | Nica Denis,<br>Doctor in physics and mathematics,<br>Associate professor,<br>Speciality: 01.04.02 – Theoretical and Mathematical Physics |

Author:

**CHISINAU, 2015**

**UNIVERSITATEA DE STAT DIN MOLDOVA**

Cu titlu de manuscris
C.Z.U: 539.21

**COCEMASOV ALEXANDR**

# PROCESELE FONONICE ÎN GRAFEN ȘI NANOSTRUCTURI PE BAZA DE SILICIU

## 131.04 – FIZICĂ COMPUTAȚIONALĂ ȘI MODELAREA PROCESELOR

**Teză de doctor în fizică**

Conducătorul științific:

Nica Denis,
Doctor în științe fizico-matematice,
Conferențiar cercetător,
Specialitatea: 01.04.02 – Fizica teoretică și matematică

Autorul:

**CHIȘINĂU, 2015**

**© Cocemasov Alexandr, 2015**

## CONTENTS

**SUMMARY (English, Romanian, Russian)** . . . . . . . . 6
**LIST OF ABBREVIATIONS** . . . . . . . . 9
**INTRODUCTION** . . . . . . . . 10

1. **PHONON AND ELECTRON PROCESSES IN GRAPHENE AND Si-BASED NANOSTRUCTURES**

1.1. Electron processes in Si-based nanostructures . . . . . . . . 17
1.2. Theoretical models for phonons in nanostructures . . . . . . . . 23
1.3. Phonon processes in Si-based nanostructures and graphene . . . . . . . . 27
1.4. Conclusions to chapter 1 and objectives of the Thesis . . . . . . . . 39

2. **PHONON PROCESSES IN Si NANOLAYERS AND PLANAR Si/Ge SUPERLATTICES**

2.1. Born – von Karman lattice dynamics model for nanolayers and planar superlattices . . . . . . . . 40
2.2. Phonon processes in Si nanolayers . . . . . . . . 42
    2.2.1. Phonon energy spectra and scattering processes . . . . . . . . 42
    2.2.2. Phonon thermal conductivity . . . . . . . . 46
2.3. Phonon processes in planar Si/Ge superlattices . . . . . . . . 51
    2.3.1. Phonon energy spectra . . . . . . . . 51
    2.3.2. Phonon scattering processes. Scattering on Si/Ge interface . . . . . . . . 54
    2.3.3. Phonon thermal conductivity . . . . . . . . 62
2.4. Conclusions to chapter 2 . . . . . . . . 66

3. **PHONON AND ELECTRON PROCESSES IN Si-BASED MODULATED NANOWIRES**

3.1. Effective mass method and electron energy spectra in Si/SiO$_2$ core/shell modulated nanowires . . . . . . . . 67
3.2. Phonon processes in Si and Si/Ge core/shell modulated nanowires . . . . . . . . 71
3.3. Electron-phonon interaction in Si-based modulated nanowires . . . . . . . . 90
3.4. Conclusions to chapter 3 . . . . . . . . 93

4. **PHONON PROCESSES IN MULTILAYER GRAPHENE WITH DIFFERENT ATOMIC STACKING**

4.1. Theoretical model for phonons in multilayer graphene . . . . . . . . 95
4.2. Phonon processes in single-layer, two-layer, three-layer graphene and graphite . . . . . . . . 99
    4.2.1. Energy spectra and vibrational properties . . . . . . . . 99

4.2.2. Phonon scattering processes and thermal properties . . . . . . . . . . . . . . . . . . . . . . 105
4.3. Twisted two-layer graphene. Engineering phonons with atomic plane rotations . . . . . . 112
4.4. Conclusions to chapter 4 . . . . . . . . . . . . . . . . . . . . . . . . . . . . . . . . . . . . . . . . . . . . . . . 120
**GENERAL CONCLUSIONS AND RECOMMENDATIONS** . . . . . . . . . . . . . . . . . . . . . 122
**REFERENCES** . . . . . . . . . . . . . . . . . . . . . . . . . . . . . . . . . . . . . . . . . . . . . . . . . . . . . 125
**Declarația privind asumarea răspunderii** . . . . . . . . . . . . . . . . . . . . . . . . . . . . . . . . . . 138
**CURRICULUM VITAE** . . . . . . . . . . . . . . . . . . . . . . . . . . . . . . . . . . . . . . . . . . . . . . . 139

# SUMMARY (English, Romanian, Russian)

## SUMMARY

Cocemasov Alexandr, „Phonon processes in graphene and silicon-based nanostructures", doctor thesis in physics, Chisinau, 2015. Introduction, 4 Chapters, General conclusions and recommendations, 200 References, 140 Pages, 66 Figures, 7 Tables. The results presented in the thesis are published in 33 scientific works.

*Key words*: phonons, electrons, nanolayer, superlattice, nanowire, graphene, lattice dynamics, modulation, thermal properties.

**Domain of study:** physics of nanosystems.

**Goal and objectives:** investigation of phonon processes in graphene (single-, two-, three-layer graphene and twisted graphene) and silicon-based nanostructures (Si nanolayers, Si/Ge superlattices and Si-based modulated nanowires), and search of the methods for targeted control of their phonon properties.

**Scientific novelty and originality:** a Born – von Karman lattice dynamics model for nanolayers, planar superlattices, cross-section modulated nanowires and multilayer graphene with different atomic stacking was developed; the influence of shell material and cross-section modulation on phonon and electron processes in Si-based nanowires was studied; a theoretical approach for calculation of scattering time of phonons on interfaces of Si/Ge superlattices was developed and the influence of Si/Ge interface quality on phonon and thermal properties of these superlattices was investigated; the influence of different atomic stacking on phonon and thermal processes in multilayer graphene was studied.

**Important scientific problem solved:** it was demonstrated and investigated theoretically the possibility to control the phonon processes in two-layer graphene by rotation of graphene layers one against another around the axis perpendicular to the graphene plane. Theoretical model of lattice dynamics in rotated ("twisted") two-layer graphene was developed.

**Theoretical importance:** were developed theoretical approaches for targeted control of phonon processes in graphene and silicon-based nanostructures.

**Practical significance:** the practical implementation of the obtained theoretical results can lead to fabrication of new classes of nanostructures with specifically desired phonon properties.

# ADNOTARE

Cocemasov Alexandr, „Procesele fononice în grafen și nanostructuri pe baza de siliciu”, teză de doctor în științe fizice, Chişinău, 2015. Introducere, 4 Capitole, Concluzii generale și recomandări, 200 Titluri bibliografice, 140 Pagini, 66 Figuri, 7 Tabele. Rezultatele prezentate în teză sunt publicate în 33 de lucrări științifice.

*Cuvintele-cheie*: fononi, electroni, nanostrat, suprarețea, nanofir, grafen, dinamica rețelei, modulație, proprietăți termice.

**Domeniul de studiu:** fizica nanosistemelor.

**Scopul și obiectivele:** investigarea proceselor fononice în grafen (cu un singur, două, trei straturi și grafen ”twisted”) și nanostructuri pe baza de siliciu (nanostraturi din Si, suprarețele Si/Ge și nanofire modulated pe baza de Si), și căutarea metodelor de control precondiționat a proprietăților lor fononice.

**Noutatea și originalitatea științifică:** a fost dezvoltat modelul Born – von Karman a dinamicii rețelei cristaline pentru nanostraturi, suprarețele planare, nanofire cu secțiunea transversală modulată și grafen multistrat cu aranjarea cristalină diferită; a fost studiată influența materialului de înveliș și modulației secțiunii transversale asupra proceselor fononice și electronice în nanofirele pe baza de Si; a fost dezvoltată o metodă teoretică pentru calcularea timpului de relaxare în procesele de împrăștiere a fononilor pe interfețele suprarețelelor Si/Ge și a fost studiată influența calității interfețelor Si/Ge asupra proprietăților fononice și termice al acestor suprarețele; a fost studiată influența aranjării cristaline asupra proceselor fononice și termice în grafenul multistrat.

**Problema științifică importantă soluționată:** a fost demonstrată și investigată teoretic posibilitatea de control a proceselor fononice în grafenul bistrat prin rotația straturilor de grafen unul împotriva altuia în jurul axei perpendiculare către planul straturilor. A fost dezvoltat modelul teoretic a dinamicii rețelei cristaline în grafenul bistrat cu rotația dintre straturi (”twisted”).

**Semnificația teoretică:** au fost dezvoltate metode teoretice de control precondiționat a proceselor fononice în grafen și nanostructuri pe baza de siliciu.

**Valoarea aplicativă:** implementarea practică a rezultatelor teoretice obținute poate contribui la fabricarea a nanostructurilor cu proprietăți fononice precondiționate.

# АННОТАЦИЯ

Кочемасов Александр, „Фононные процессы в графене и наноструктурах на базе кремния”, диссертация на соискание ученой степени доктора физических наук, Кишинев, 2015. Введение, 4 Главы, Общие выводы и рекомендации, 200 Ссылок, 140 Страниц, 66 Рисунков, 7 Таблиц. Результаты, представленные в диссертации, опубликованы в 33 научных работах.

*Ключевые слова*: фононы, электроны, нанослой, сверхрешетка, нанонить, графен, динамика решетки, модуляция, тепловые свойства.

**Область исследований:** физика наносистем.

**Цель и задачи:** исследование фононных процессов в графене (одно-, двух-, трех-слойном и “twisted” графене) и наноструктурах на базе кремния (Si нанослоях, Si/Ge сверхрешетках, модулированных нанонитях на базе Si), и поиск методов целенаправленного управления их фононными свойствами.

**Научная новизна и оригинальность:** развита модель динамики решетки Борна – фон Кармана для нанослоев, плоских сверхрешеток, нанонитей с модуляцией поперечного сечения и многослойного графена с различной упаковкой графеновых слоев; исследовано влияние материала обкладки и модуляции поперечного сечения на фононные и электронные процессы в нанонитях на базе Si; развит теоретический подход для расчета времени рассеяния фононов на интерфейсах Si/Ge сверхрешеток и исследовано влияние качества Si/Ge интерфейса на фононные и тепловые свойства этих сверхрешеток; изучено влияние способа упаковки графеновых слоев на фононные и тепловые процессы в многослойном графене.

**Решенная важная научная задача:** теоретически продемонстрирована и исследована возможность управления фононными процессами в двухслойном графене путем поворота графеновых слоев друг относительно друга вокруг оси перпендикулярной к плоскости слоев. Развита теоретическая модель динамики решетки в двухслойном графене с поворотом (“twisted”).

**Теоретическая значимость:** разработаны теоретические подходы для управления фононными процессами в графене и наноструктурах на базе кремния.

**Прикладная ценность:** практическая реализация полученных теоретических результатов может способствовать появлению новых классов наноструктур с определенно заданными фононными свойствами.

# LIST OF ABBREVIATIONS

BZ – Brillouin zone
DFT – density-functional theory
BvK – Born - von Karman
FCC – face-centered cubic
VFF – valence force field
RT – room temperature
LAPACK – Linear Algebra PACKage
ML – monolayer
NW – nanowire
MNW – modulated nanowire
DOS – density of states
TF – thermal flux
BTE – Boltzmann transport equation
BLG – bilayer graphene
FLG – few-layer graphene
T-BLG – twisted bilayer graphene
T-FLG – twisted few-layer graphene

# INTRODUCTION

## Relevance and importance of the subject of the Thesis

The relevance and importance of the subject of the Thesis is determined by a huge interest from both scientific and engineering community toward the nanoscale structures and materials with enhanced electron and phonon properties. The investigation of electron and phonon processes in nanostructures, as well as the search for novel nanoscale geometries and materials with properly engineered electron and phonon properties represents one of the most important problems of modern nanoscience. The technological progress in dimensional scaling of different material structures in the past few decades determined many important advancements in various areas: electronics, phononics, thermal management, thermoelectricity, photovoltaics, energy storage, etc. Further development of these fields requires a thorough understanding of the electron and phonon processes at nanoscale level.

Electrons and phonons manifest themselves in all properties of materials: mechanical, optical, thermal, chemical, etc. Spatial confinement of electrons and phonons in nanostructures strongly affects their energy spectra, density of states and electron-phonon interaction. Thus, nanostructures offer a new way of controlling electron and phonon processes together with electron - phonon interaction via tuning electron and phonon dispersion relations, i.e. electron and phonon engineering. While electron engineering idea has been widely used during the last 60 years, the phonon engineering is a relatively new approach. Phonon engineering is considered to be as powerful as the idea of the band-gap engineering for electrons, which is now utilized in a variety of devices.

One of the areas where phonon engineering is playing an extremely important role is heat management at nanoscale, since phonons are the main heat carriers in many nanostructured material systems such as semiconductor and carbon nanostructures. Aggressive miniaturization of electronic devices and increasing their operation speed makes the problem of heat removal from the electronic circuits particularly important. Therefore the scientific search of materials with high thermal conductivity becomes extremely crucial for the future development of nanoelectronics. One of the two-dimensional nanostructures investigated in this Thesis is single-layer and few-layer graphene. Graphene, among its excellent electron conductive properties, reveals extremely high thermal conductivity. Few-layer graphene flakes, which are easy to produce, also posses unusual physical properties: depending on the stacking configuration they demonstrate metallic- or semiconductor-like behavior. Despite of the fact that numerous scientific studies of the thermal properties in few-layer graphene have been carried out in the last few years, the phonon and thermal properties in twisted few-layer graphene, when one carbon layer is rotated relatively to another layer by a specific angle were not studied yet. This investigation is very important and timely because change in the phonon properties in twisted few-layer graphene for different angles of rotation may significantly modify its thermal properties and can give an important insight into the physics of interlayer interaction in few-layer graphene.

Another area where electron and phonon engineering has given a significant performance boost is thermoelectricity, i.e. thermal-to-electrical energy conversion and vice-versa. Among other renewable energy sources, thermoelectricity provides unique opportunity since it can be used as a generator deriving power out of waste heat from different sources: integrated chips, cars, buildings, etc. This opens up the exciting area of thermoelectric waste heat recovery. One-dimensional and two-dimensional nanostructures are one of the most promising thermoelectric materials that allow separate engineering of electronic and thermal properties. The ability to manipulate the materials at the atomic scale using nanostructures such as nanowires, thin films and superlattices plays a key role in enhancing the thermoelectric efficiency.

## Goal and objectives of the Thesis

The **goal** of this Thesis is the investigation of phonon processes in graphene and silicon-based nanostructures, as well as determination of novel nanostructures for effective electron and phonon engineering.

In order to achieve this goal, the following **objectives** are formulated:

1. Determination of novel one-dimensional and two-dimensional nanostructures with specific geometrical and material parameters, as perspective candidates for electron and phonon engineering.
2. Development of theoretical models to describe phonon and electron states in novel one-dimensional and two-dimensional nanostructures.
3. Investigation of electron, phonon and thermal properties of novel as well as generic one-dimensional and two-dimensional nanostructured materials.

The following theoretical **methods** and **models** are used to accomplish the objectives:

1. Lattice dynamics theory for theoretical modeling the phonon states in novel one-dimensional and two-dimensional nanostructures.
2. Extension and application of the effective mass approach in order to investigate electron states in novel nanostructures.
3. Extension and application of the Boltzmann transport equation approach for modeling the thermal properties of novel one-dimensional and two-dimensional nanoscale structures.

**Scientific novelty of the results:**

1. A Born - von Karman lattice dynamics model for cross-section modulated nanowires and multilayer graphene with different atomic stacking was developed.
2. The influence of cross-section modulation on phonon and electron processes in Si-based nanowires was studied for the first time.
3. A theoretical approach for calculation of scattering time of phonons on interfaces of Si/Ge superlattices was developed and the influence of Si/Ge interface quality on phonon and thermal properties of these superlattices was analyzed.
4. The influence of different atomic stacking on phonon and thermal processes in multilayer graphene was elucidated for the first time.

An **important scientific problem** was solved in the Thesis namely it was demonstrated and investigated theoretically the possibility to control the phonon processes in two-layer graphene by rotation of graphene layers one against another around the axis perpendicular to the graphene plane.

**Main items to be defended:**

1. An up to 5 times drop of the phonon heat flux at room temperature is predicted in Si cross-section modulated nanowires in comparison with generic uniform Si nanowires, using the lattice dynamics Born – von Karman model and the Boltzmann transport equation for phonons. The effect is explained by the redistribution of the phonon energy spectra, strong decrease of the average phonon group velocities and exclusion of the phonon modes trapped in cross-section modulated nanowires segments from the heat flow.
2. Using the lattice dynamics Born – von Karman model and the Boltzmann transport equation approach it was demonstrated theoretically that in Si/Ge core/shell cross-section modulated nanowires the combination of cross-section modulation and acoustic mismatch between Si and Ge materials can lead to a three orders of magnitude drop of room temperature phonon thermal conductivity as compared to bulk Si.
3. A new type of hybrid folded rotationally-dependent phonon modes in twisted bilayer graphene were predicted employing lattice dynamics Born – von Karman model for intralayer interaction and an angle-dependent interlayer interatomic potential. These modes appear due to reduction of the Brillouin zone size and changes in the interaction between graphene layers.
4. Applying the Boltzmann transport equation approach for phonons it was theoretically demonstrated that in single-layer, bilayer and twisted bilayer graphene the phonon specific

heat at temperatures less than 15 K varies as $T^n$, where $n = 1$ for graphene, $n = 1.6$ for bilayer graphene and $n = 1.3$ for twisted bilayer graphene.

## Theoretical importance and practical significance of the results

Theoretical importance of the results presented in the Thesis consists in the elaboration of new (such as Born – von Karman model of lattice dynamics for modulated nanowires and twisted bilayer graphene) and the extension of existent (such as effective mass approach for electrons and Boltzmann transport equation for thermal transport in modulated nanowires) theoretical approaches for investigation of phonons and electrons in graphene and silicon-based nanostructures. Another significant scientific result of the Thesis is the determination of novel nanoscale structures, such as core/shell modulated nanowires and twisted bilayer graphene, with high electron and phonon engineering abilities.

The practical significance of the Thesis consists in the fact that the obtained theoretical results may contribute to the design and practical realization of novel nanostructures with optimized and properly engineered electron and phonon properties.

## Approbation of the results

The results obtained in the Thesis were presented at following international scientific conferences:

- VII-th International Conference of Young Researchers „**ICYR-2009**”, *Chisinau, Moldova*, 2009.
- VIII-th International Conference of Young Researchers „**ICYR-2010**”, *Chisinau, Moldova*, 2010.
- IX-th International Conference of Young Researchers „**ICYR-2011**”, *Chisinau, Moldova*, 2011.
- 9th European Conference on Thermoelectrics „**ECT-2011**”, *Thessaloniki, Greece*, 2011.
- **DPG Spring Meeting - 2012**, *Berlin, Germany*, 2012.
- 13th International Conference on Modern Information and Electronic Technologies „**MIET-2012**”, *Odessa, Ukraine*, 2012.
- **I-st All-Russian Congress of Young Scientists**, *Saint-Petersburg, Russia*, 2012.
- International Scientific Conference for Undergraduate and Postgraduate Students and Young Scientists „**Lomonosov-2012**”, *Moscow, Russia*, 2012.
- X-th International Conference of Young Researchers „**ICYR-2012**”, *Chisinau, Moldova*, 2012.

- International Scientific Conference for Undergraduate and Postgraduate Students and Young Scientists „**Lomonosov-2013**”, *Moscow, Russia*, 2013.
- 14th International Conference on Modern Information and Electronic Technologies „**MIET-2013**”, *Odessa, Ukraine,* 2013.
- **CECAM-Workshop**: **Nanophononics**, *Bremen, Germany,* 2013.
- 15th International Conference on Modern Information and Electronic Technologies „**MIET-2014**”, *Odessa, Ukraine,* 2014.
- **DPG Spring Meeting - 2014**, *Dresden, Germany*, 2014.

**Publications**

Based on the results presented in the Thesis 33 scientific works were published, including 6 articles in ISI journals and 15 abstracts at international conferences. 2 articles and 2 abstracts were published without coauthors.

**Structure of the Thesis**

The Thesis consists of Introduction, 4 Chapters and Conclusions. The Thesis contains 200 references, 140 pages, 66 figures and 7 tables.

In **Chapter 1** is presented a detailed review of recent theoretical and experimental investigations of phonon and electron processes in graphene and silicon-based nanostructures.

In **Chapter 2** a Born-von Karman model of lattice dynamics for nanolayers and planar superlattices with diamond crystal lattice is developed. The Boltzmann transport equation approach is proposed for the investigation of the phonon and thermal processes in Si nanolayers and Si/Ge planar superlattices. Phonon energy spectra within Born – von Karman model of lattice dynamics are calculated for silicon nanolayers of different widths. An analytical expression for phonon thermal conductivity coefficient for nanolayers is obtained from Boltzmann transport equation in relaxation time approximation. Thermal transport is investigated in nanometer-wide silicon nanolayers and a good agreement between theoretical calculations and the experimental data for 20-nm-thick and 30-nm-thick silicon nanolayers is obtained. The major phonon scattering processes in nanolayers, such as Umklapp and phonon-boundary scattering are described and their influence on the total thermal conductivity is analyzed. The optical phonons contribution to total thermal conductivity of silicon nanolayers of different widths and at different temperatures is elucidated. In case of planar Si/Ge superlattices phonon energy spectra and average phonon group velocity are calculated and analyzed. The perturbation theory and second quantization formalism are used in order to model the scattering of phonons on interfaces in Si/Ge superlattices. The role of interface mass-mixing scattering of phonons in limiting the total phonon lifetime in Si/Ge planar superlattices is established. It is concluded that interface mass-mixing scattering of phonons can lead to a peculiar behavior of phonon thermal conductivity of these structures owing to the non-trivial dependence of interface scattering rate on the amplitudes of the atomic displacements. For a wide temperature range from 50 K to 400 K a good agreement between theoretical and experimental phonon thermal conductivity is obtained for a Si/Ge planar superlattice when phonon-phonon scattering is not taken into account, indicating that the interface mass-mixing scattering can be the dominant mechanism of phonon scattering in real Si/Ge planar superlattices.

In **Chapter 3** the effective mass approximation is extended and applied for calculation and investigation of electron energy spectra and electron wave functions in core/shell Si/$SiO_2$ nanowires with constant and periodically modulated cross-section. The influence of cross-section modulation on the electron energy spectra and electron wave functions in Si nanowires is established. An inhomogeneity in the ground state wave function distribution along the wire’s axis is found. The lattice dynamics Born – von Karman model and the Boltzmann transport equation are applied for the investigation of phonon and thermal processes in Si nanowires, Si cross-section modulated nanowires and novel Si/Ge core/shell cross-section modulated nanowires. The possibility of a significant suppression of the phonon heat flux in Si cross-section modulated nanowires in comparison with the generic uniform cross-section Si nanowires is theoretically demonstrated. A strong decrease of the average phonon group velocities together with a corresponding suppression of the phonon thermal flux is found and the mechanisms behind this suppression are elucidated. The phonon and thermal properties in novel Si/Ge core/shell cross-section modulated nanowires are investigated. The combination of cross-section modulation and acoustic mismatch between Si and Ge materials is proposed as an effective tool for engineering phonon flux in the one-dimensional modulated heterostructures. A drastic reduction of the room temperature thermal conductivity in Si/Ge core/shell cross-section modulated nanowires in comparison with bulk Si is predicted. A detailed explanation of this effect is presented.

The **Chapter 4** is devoted to the investigation of phonon and thermal properties of single-, two- and three-layer graphene as well as of twisted bilayer graphene structure with different angles of rotation between the graphene planes. A Born – von Karman model of lattice dynamics for these structures is developed and phonon energy spectra in all high-symmetry crystallographic directions are calculated. The comparison between theoretical and experimental phonon frequencies is presented. The tabulated phonon frequencies for twisted bilayer graphene for different rotational angles are provided. The Boltzmann transport equation approach is applied for thermal transport modeling in single- and few-layer graphene. The influence of the rotational angle on the phonon energy spectra, as well as phonon mode-specific contribution to the thermal transport of single-, two- and three-layer graphene is established. The role of different phonon scattering processes in limiting the thermal conductivity of single-layer and non-rotated few-layer graphene is determined. The appearance of a new type of hybrid folded rotationally-dependent phonon modes in twisted bilayer graphene is theoretically predicted and the physics behind this phenomenon is elucidated. The temperature dependence of the phonon heat capacity in twisted bilayer graphene, calculated for the first time, is presented.

## ACKNOWLEDGEMENTS

Author expresses his deepest gratitude to the scientific advisor Dr. Denis Nica for guidance, help and encourangement throughout the work and beyond. Author is indebted to the late, great Prof. Evghenii Petrovich Pokatilov, whose inspiring example and impact are continuously motivating the author in his scientific search.

Author kindly appreciates the help and support from his colleagues at the ”E. Pokatilov Laboratory of Physics and Engineering of Nanomaterials” of Moldova state University – S. I. Boldirev, D. Crismari, C. Isacova, V. I. Brinzari, L. I. Leu, L. V. Tarakanova, A. Askerov, N. Gaiu, A. Cliucanov. Their friendly atmosphere and useful discussions are very much acknowledged.

Author would like to thank Prof. Alexander Balandin and Prof. Vladimir Fomin for a valuable experience at the University of California – Riverside and Institute for Integrative Nanosciences – Dresden. Their fruitfull collaboration and co-authorship are greatly recognized.

# 1. PHONON AND ELECTRON PROCESSES IN GRAPHENE AND Si-BASED NANOSTRUCTURES

## 1.1. Electron processes in Si-based nanostructures

The key effect which determines the electronic properties of nanoscale structures is quantum confinement. When the characteristic dimensions of the material become comparable to the *de Broglie* wavelength of the electron wave function the quantum confinement effect manifests itself in quantization of the electron energy spectrum i.e. appearance of discrete energy levels and band gaps [1]. Thus, shrinking the geometrical dimensions of structures results in the size-dependence of their electronic properties, which may deviate substantially from their bulk values [2]. One of the most important steps in investigation of the electronic properties of nanostructures is the choice of an appropriate bandstructure model.

The electronic bandstructure calculations are based on the solution of the Schrodinger equation. One of the most widely used approaches to solve the Schrodinger equation is the *effective mass approach*. The general form for the electronic Hamiltonian in the effective mass approach has the form:

$$\hat{H} = -\frac{\hbar^2}{2}[\frac{\partial}{\partial x}M_x(x,y,z)\frac{\partial}{\partial x}+\frac{\partial}{\partial y}M_y(x,y,z)\frac{\partial}{\partial y}+\frac{\partial}{\partial z}M_z(x,y,z)\frac{\partial}{\partial z}]+V_b(x,y,z)\,,$$

where $\hbar$ is Planck constant, $V_b(x,y,z)$ is potential barrier in $(x,y,z)$ point, $M_i(x,y,z)$ is the inverse electron effective mass along the *i* axis. Once the Hamiltonian $\hat{H}$ is constructed the electron energy states and wave functions are obtained from a numerical solution of a time-independent Schrodinger equation:

$$\hat{H}\Psi_n = E_n\Psi_n,$$

where $E_n$ and $\Psi_n$ is electron energy and electron wave function for quantum number *n*, respectively. Using the appropriate boundary conditions for a given nanostructure's geometry one can obtain the dispersion relation $E_n(\vec{k})$ for a set of electron wave vectors $\vec{k}$. However, it should be pointed out that in the effective mass approach the actual atomistic structure of a material is not taken into account. As a result, the effective mass approach works well only in the vicinity of conduction band minima and does not ensure a correct calculation of the electronic bandstructure in the entire BZ of nanostructures.

During the last two decades empirical *tight-binding methods* have become the primary tool in obtaining the correct electronic bandstructure of different nanostructures. Properly adjusting the parameters of a tight-binding model allows one to correctly reproduce the electronic band gaps and effective masses in the entire BZ. The original tight-binding method was first proposed by Slater and Koster and accounted for eight electronic orbitals: one *s* and three *p* orbitals with spin up and spin down polarizations ($sp^3$) [3]. In Ref. [4] the approach was extended to include a fictitious *s*-like state $s^*$, which accounted for all other outer orbital interactions and allowed for a more accurate description of the conduction band in zincblende semiconductors. Recent developments in tight-binding methods [5-7] include also the excited *d* orbitals ($sp^3d^5s^*$) and can reproduce accurately the complete bulk bandstructure of many crystals.

In particular, it is usually enough to include the interactions between nearest neighbor atoms only. For example, the nearest neighbor $sp^3d^5s^*$ tight-binding model is composed of orthogonal orbitals [3, 8] localized on atoms which form the basis set of the electronic structure calculation. The orbitals are: 1 *s* orbital, 3 *p* orbitals, 5 *d* orbitals and 1 $s^*$ orbital. The orbitals on one atom can interact with orbitals on other neighbor atoms and the resulting wave functions are called the “two-centered integrals” [3]. Within the semi-empirical tight-binding models these two-centered integrals are used as fitting parameters [8]. The algorithm for calculating these parameters was given in Refs. [8-9]. The tight-binding model with properly adjusted parameters allows one to obtain correct energy dispersions and effective masses at high-symmetry points in the entire BZ of nanostructure. A detailed methodology of tight-binding implementation in bulk and nanostructures was provided in Refs. [8, 10].

The most recent developments in electronic bandstructure calculations include *ab initio* techniques, such as DFT [11]. The fundamental importance and predictive power of the *ab initio* techniques, especially when applied to the novel nanostructured materials, is hard to overestimate. However, due to a great computational complexity of the DFT calculations, mainly arising from the many-body interactions problem, its use in studying the electronic properties of real-size nanostructures is still very limited. Therefore, the specifics of the DFT approach are not covered in this Thesis; for detailed information on the DFT models one can refer to works [11-14].

Due to their excellent electronic properties, silicon nanolayers and nanowires currently constitute the main material base for modern nanoelectronic devices, such as metal-oxide-semiconductor field-effect transistors (MOSFETs) and fin field-effect transistors (FinFETs) [15-20]. The characteristic size of the active silicon channels in the state-of-art FETs is *14 nm* (as to 2014 year), considering the silicon lattice constant ~ 0.543 nm, they consists of just *100* atomic layers. At this dimensional scale the quantum confinement of carriers (electrons, phonons, etc.) is one of the main mechanisms which determine the characteristics of a nanoelectronic device.

Below are reviewed some of the recent developments in theoretical and experimental studies on electron-assisted processes in different nanostructures, with central attention paid to the Si-based one-dimensional and two-dimensional nanoscale materials.

In Ref. [21] the authors have studied the effect of confinement dimensions and crystallinity on the magnitude of the band gap expansion (as a function of decreasing size) in Si and Ge nanolayers, nanowires and quantum dots. Models with medium and strong confinement provided the best fit to experimental results. In Figures 1.1 and 1.2 it is presented the experimental and theoretical electronic energy gap in disordered and crystalline silicon nanolayers as a function of layer thickness.

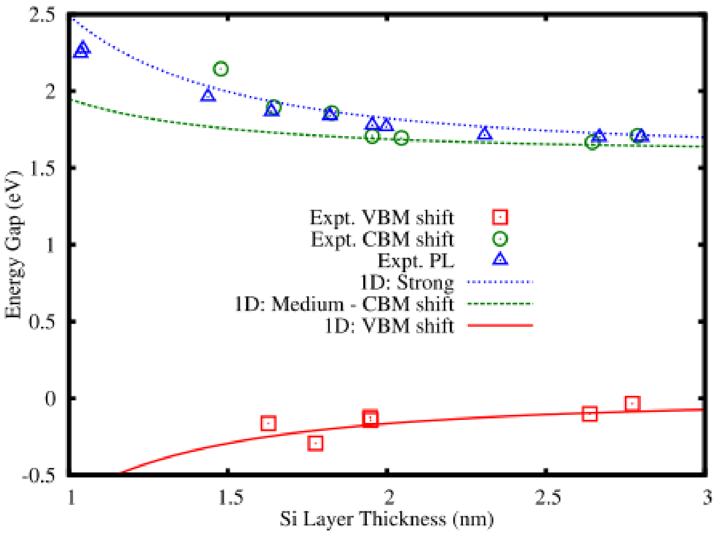

Fig. 1.1. The dependence of energy gap on layer thickness in *disordered* Si nanolayers. The dots, triangles and squares represent experimental data, while lines denote theoretical calculations from Ref. [21].

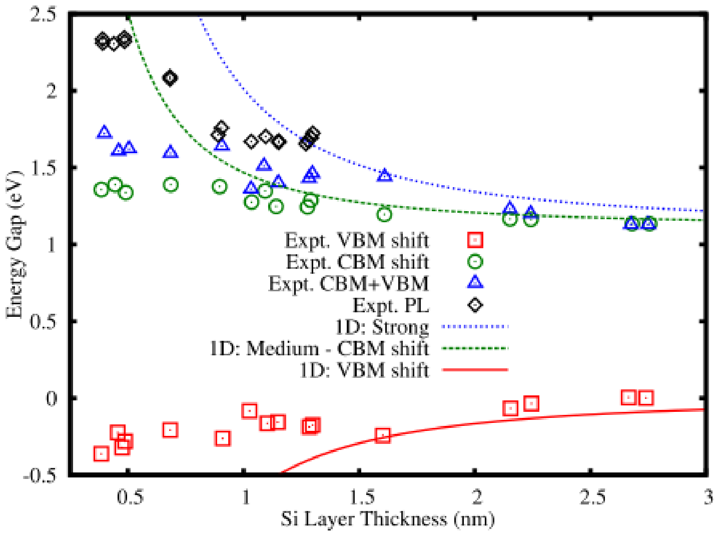

Fig. 1.2. The dependence of energy gap on layer thickness in *crystalline* Si nanolayers. The dots, triangles and squares represent experimental data, while lines denote theoretical calculations from Ref. [21].

It was concluded that crystalline materials exhibit medium confinement, while amorphous materials exhibit strong confinement regardless of the confinement dimensions of the system.

In Ref. [22] the authors have used methods derived from first-principles to examine the effect of different surface preparation, namely, passivation of silicon surface bonds by -H, -OH and -$NH_2$, on the band gap of silicon nanowires with varying diameters. For both [100] and [110] oriented nanowires they found that the band gap narrows with increased wire diameter to the bulk value for large diameters. However, surface termination by -OH and -$NH_2$ introduces a hybridization effect that competes with quantum confinement at smaller diameters, inducing a large relative red shift to the band gap by up to 1 eV for small diameter wires. In Figure 1.3 is plotted the calculated band gap $E_g$ for nanowires with different surface terminations as the diameter of the silicon core changes.

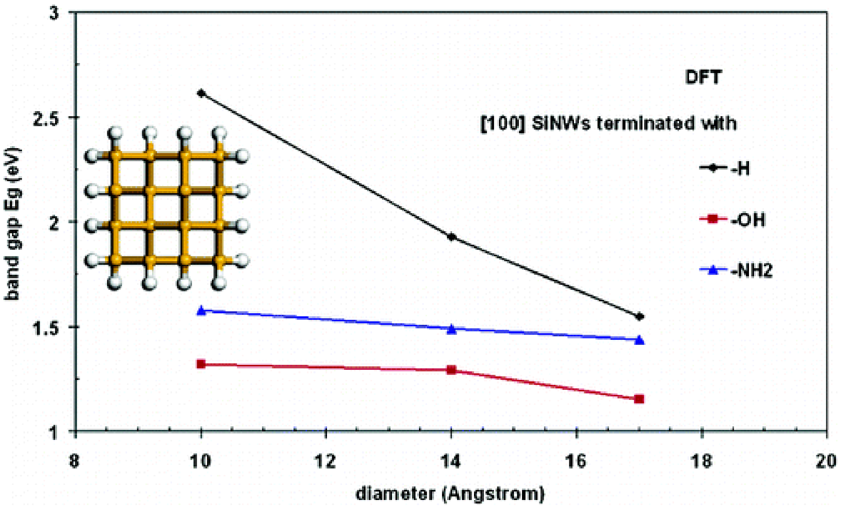

Fig. 1.3. The calculated within an *ab initio* approach electronic band gap as a function of the [100] silicon nanowire diameter for various surface terminations. The figure is taken from Ref. [22].

The origin of the reduced band gap was related to the interaction between the Si 3p and O/N 2p states in the valence band edge of the nanowire. The obtained results allow for a simple electronic structure engineering of nanometer scale silicon wires via surface treatment.

In the recent publication [23] the authors settled a general expression for the Hamiltonian of the electron-phonon deformation potential interaction in case of a novel nanosystem – non-polar core-shell cylindrical nanowire. On the basis of long range phenomenological continuum model for the optical phonon modes and by taking into account the bulk phonon dispersions, they studied the size dependence and strain-induced shift of the electron-phonon coupling strengths for Ge-Si and Si-Ge core-shell nanowires. The deformation potential electron-phonon Hamiltonian was derived analytically and some numerical results for the frequency core modes and vibrational amplitudes were reported. The developed approach allows for the unambiguous identification of the strain and confinement effects in non-polar core-shell nanowires. The obtained results contribute to the characterization and device applications of the novel core-shell nanowires.

In Ref. [24] the authors reported on fabrication and characterization of ultra-thin suspended single crystalline flat silicon layers with thickness down to 6 nm. They have developed a method to control the strain in the nanolayers by adding a strain compensating frame on the silicon nanolayer perimeter to avoid buckling of the released layers. The magnitude of the strain was related to the strain compensation ratio as $R_c=w_c/w_m$, where $w_m$ is the width of the bare Si part of the nanolayer and $w_c$ is the width of the area of the released layer covered with the compensating layer ($Si_3N_4$). To illustrate the effect of the compensation ratio $R_c$ and the thickness of the nanolayer on the induced strain, LO phonon peaks measured from sets of 54 and 6 nm thick layers with various $R_c$ of 0.8, 1.2 and 3.5, together with a reference Si LO peak are shown in Fig. 1.4.

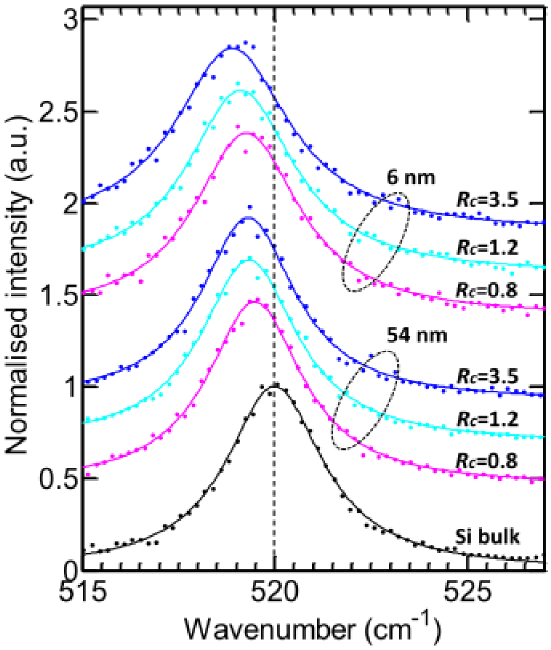

Fig. 1.4. LO peaks measured by Raman scattering from 6 and 54 nm thick free-standing Si nanolayers with the strain compensation ratio $R_c$ of 0.8, 1.2 and 3.5. The figure is taken from Ref. [24].

It was shown that by changing the properties of the frame the strain in the silicon nanolayer can be tuned in a controlled manner. The authors argued that both the mechanical properties and the electronic band structure can be engineered and the resulting strain-engineered nanolayers provide a unique laboratory to study low-dimensional electronic, photonic and phononic phenomena.

In Ref. [25] by Boykin T. et.al. the theory, based on empirical tight-binding approach, was developed to describe the valley splitting observed in silicon nanolayers with strain. The valley splitting was computed for realistic devices proposed for quantum computing. It was shown, that the splitting is in general nonzero even in the absence of electric field. The splitting in a square well oscillated as a function of the number of atomic layers in the silicon nanolayer, with a period that was determined by the location of the valley minimum in the BZ.

One of the hottest topics of today’s solid state physics is related with investigation of electronic and other properties of carbon materials, such as carbon nanotubes, single- and few-layer graphene, graphene nanoribbons, etc. Owing to some of their unique properties, carbon nanomaterials are considered one of the most perspective candidates for future high-tech nanoelectronic applications. In this context, the reports on the unusual properties of novel nanostructures made from conventional semiconductor materials, which could extend the applicability of the current well elaborated semiconductor technologies, are of a particular interest. One of the recent such results were presented in Ref. [26] by Perim E. et.al. In their work the authors reported on theoretical discovery of novel silicon and germanium tubular nanostructures with no corresponding stable carbon analogues. The electronic and mechanical properties of these new tubes were investigated through *ab initio* methods. Their results showed that the novel tubular structures have lower crystal energy than their corresponding nanoribbon counterparts and are stable up to high temperatures. Silicon tubes were stable at temperatures as high as 500 K, while germanium ones reached temperatures as high as 1000 K. Both tubes were semiconducting with small indirect band gaps, which could be significantly altered by both compressive and tensile strains. Large bandgap variations of almost 50% were observed for strain rates as small as 3%, suggesting possible applications in a variety of technological devices.

The possibility to incorporate both electronic and optical functionality in a single material offers the tantalizing prospect of amplifying, modulating and detecting light within a monolithic platform. One of the major difficulties, which limit the application of silicon nanostructures in modern photonics, is their transparency at telecommunication wavelengths. A particularly interesting result in this direction was reported in Ref. [27] by Healy N. et.al. The authors made an important step toward the realization of the described monolithic devices. They developed a laser processing technique for silicon fibre technology through which one can modify the electronic band structure of the semiconductor material as it is crystallized. The unique fiber geometry in which the silicon core is confined within a silica cladding allowed large anisotropic stresses to be set into the crystalline material so that the size of the bandgap could be engineered. The stresses cause an anisotropic distortion of the crystal lattice which acts to reduce its electronic bandgap energy, as illustrated in Figure 1.5 below. An extreme bandgap reduction from 1.11 eV down to 0.59 eV, enabling optical detection out to 2100 nm, was demonstrated.

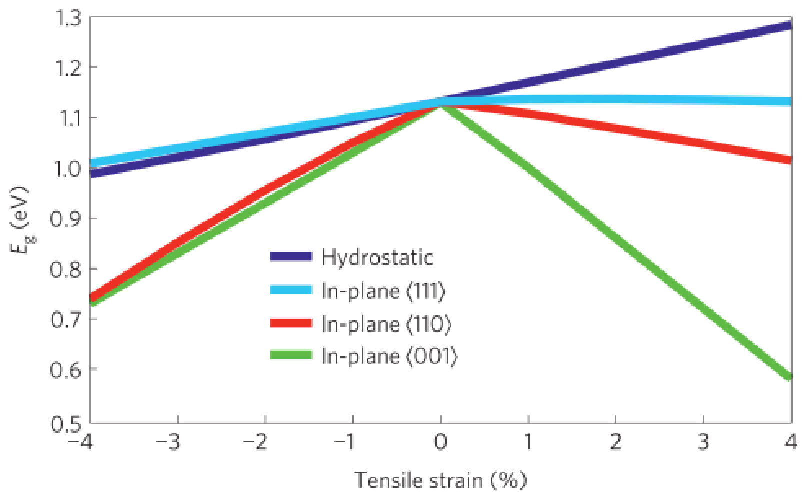

Fig. 1.5. Simulations of the bandgap as a function of strain – hydrostatic and in-plane across three main crystallographic planes. The figure is taken from Ref. [27].

Authors concluded, that the obtained results could inspire a new generation of mass-producible, fully functional, monolithic electron-photonics devices that are compatible with current semiconductor technology.

## 1.2. Theoretical models for phonons in nanostructures

The concept of a *phonon* and its properties were first introduced by P. Debye [28] in 1912. A phonon is defined as a quantum of vibrational energy within a crystal structure. A phonon (or *phonon mode*) is considered a quasi-particle with energy $\hbar\omega_s$, quasi-momentum $\hbar\vec{q}$ and vibrational polarization *s*. The set of phonon modes with the same polarization forms the *phonon branch*, and thus the index *s* is also considered as a phonon branch index. The phonon polarization is characterized by the relation between the direction of atomic vibrational motion and wave propagation. The most common examples of polarizations are: longitudinal, where atoms oscillate in the direction of wave propagation, and transverse, where atoms oscillate perpendicular to the direction of propagation. The maximum possible number of branches in a crystal equals to the number of atoms per unit cell multiplied by the number of degrees of freedom per one atom (normally three). The relation between phonon's frequency and its wave vector is called *phonon dispersion*: $\omega_s(\vec{q})$ and it is a fundamental relation of *lattice dynamics theory*. The phonon branches are divided into two categories: acoustic and optical. Acoustic branches are defined by the linear dispersion law near the BZ center: $\omega_s(q \to 0) \sim q$ with atoms within each unit cell vibrating in-phase while optical branches are defined by the relation $\omega_s(q = 0) \neq 0$, with atoms within each unit cell moving out-of-phase. However, in nanostructures due to the confinement effect the atomic vibrations are quantized and there appear a large number of mixed modes, which have the vibrational behavior of both acoustic and optical nature.

During the last century there were developed several models to describe the lattice dynamics (phonons) in bulk and nanostructured crystalline materials. These models vary greatly in complexity from simple continuum approaches to detailed *ab initio* techniques. Each of these models has their advantages and disadvantages, and their field of application can also differ. Below, the current achievements in the theory of phonons in nanostructures are reviewed. The basic concepts of the elastic continuum and force-constant models are provided.

The basics of lattice dynamics were founded in 1912 by P. Debye [28] and independently by M. Born and Th. von Karman [29]. A systematic lattice dynamics theory was presented three years later by M. Born in his book "Dynamics of Crystal Lattices" (in German) [30]. Debye introduced the definition of 'phonon' and proposed a simple model known as the elastic isotropic continuum model. The basic idea of the continuum model is that the atomic crystal structure is disregarded and crystal is treated as a continuous elastic medium. The application of continuum models in describing acoustic and optical phonon phenomena in nanostructures has been reviewed in 2001 by Stroscio and Dutta [31]. A good application of the elastic continuum model provides the case of acoustic phonon modes propagating in a nanowire. The equation of motion for elastic vibrations in an anisotropic medium can be written as:

$$\rho \frac{d^2 U_m(x_3)}{dt^2} = \frac{d\sigma_{mi}}{dx_i},$$

where $U = (U_1, U_2, U_3)$ is the displacement vector, $\rho$ is the mass density of the material, $\sigma_{mi}$ is the elastic stress tensor given by $\sigma_{mi} = c_{mikj} U_{kj}$ and $U_{kj} = \frac{1}{2}\left( \frac{\partial U_k}{\partial x_j} + \frac{\partial U_i}{\partial x_k} \right)$ is the strain tensor. The nanowire has two distinctively different symmetry planes and four possible types of the propagating phonon waves, which are the solutions of the equation of motion. These solutions are usually denoted as [32]: Dilatational: $u_x^{AS}(x,y);u_y^{SA}(x,y);u_z^{SS}(x,y)\rightarrow u_i^D$, Flexural$_1$: $u_x^{SS}(x,y);u_y^{AA}(x,y);u_z^{AS}(x,y)\rightarrow u_i^{F_1}$, Flexural$_2$: $u_x^{AA}(x,y);u_y^{SS}(x,y);u_z^{SA}(x,y)\rightarrow u_i^{F_2}$, Shear: $u_x^{SA}(x,y);u_y^{AS}(x,y);u_z^{AA}(x,y)\rightarrow u_i^{Sh}$. Here *SA* and *AS* show mode parity relative to the change of sign, $f(x,y)=f(-x,y)=f(x,-y)\rightarrow f^{SS}(x,y)$, $f(x,y)=-f(-x,y)=-f(x,-y)\rightarrow f^{AA}(x,y)$, etc. In Figure 1.6 is presented the phonon dispersion for the Dilatational polarization in the GaN nanowire with 4 nm x 6 nm cross-section. The figure is taken from Ref. [32]. The free boundary conditions are applied at the nanowire's boundary.

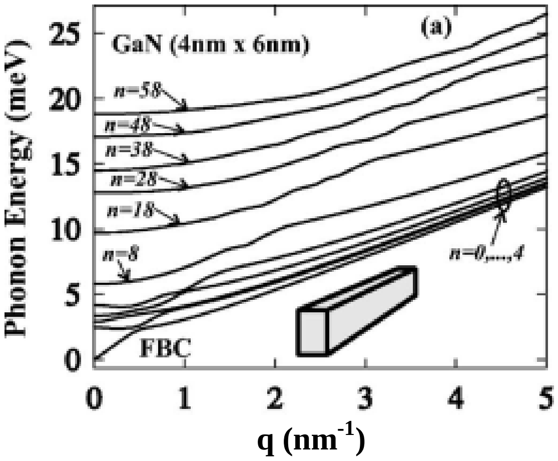

Fig. 1.6. Phonon dispersion in free-standing GaN nanowire.

One can see from Figure 1.6 that phonon spectrum of nanowire is quantized, i.e. there exist a large number of discrete energy branches with different dispersions. Also, there is only one acoustic branch in Dilatational polarization and the rest of the branches are acoustic-like with $\omega(q=0)\neq 0$, which is a direct result of phonon confinement. At the same time, there is a considerable disadvantage of the elastic continuum treatment, namely, the phonon branches at the BZ edge at high *q* (short wave lengths) posses a considerable dispersion, i.e. large group velocity, which is in contradiction with more accurate atomistic models of lattice dynamics (see for example Ref. [33]), predicting group velocities close to 0.

As the device size approaches the nanometer scale a continuum material description is no longer accurate. Lattice dynamics models, which account for discrete atomistic structure of the crystal, should be used instead. There are two main atomistic approaches in modeling the lattice dynamics of crystal lattice, these are phenomenological *force-constant* models and *ab initio* models. The *ab initio* models were first developed in the 1970's. However, *ab initio* lattice dynamics calculations in nanostructures have only recently become feasible, due to the many-body interactions problem and due to the lack of translation symmetry in one or more directions which introduces difficulties in modeling the periodic potentials of the crystal structure. Calculation of the phonon dispersion relations for nanostructures with a thousand of atoms or more is nearly impossible within *ab initio* techniques with current computational resources. This has led to the use of phenomenological force-constant models for phonons in nanostructures. These were first developed a century ago [34] and have been continuously improved and adapted for different materials and structures. In the phenomenological force-constant models the interatomic force constants are treated as fitting parameters, which should be adjusted in order to reproduce the experimentally verified phonon spectra of a bulk material. A classic lattice dynamics force-constant model called "Born – von Karman model" was developed in 1954 [35].

In BvK model the total potential energy of the crystal lattice is given in the harmonic approximation as:

$$V = \frac{1}{2} \sum_{i,j=x,y,z} \sum_{s,s'} \sum_{n_s,n'_{s'}} \Phi_{ij}(n_s, n'_{s'}) u_i(n_s) u_j(n'_{s'}) ,$$

where *i,j* numerate Cartesian coordinate components, *s,s'* numerate neighbor atomic spheres of interacting atoms *n* and *n'* correspondingly, *u* is a small atomic displacement from equilibrium position and $\Phi$ is the force constant matrix. The components of the force constant matrix are *interatomic force constants*; they are fitted to the experimental phonon frequencies of bulk material and then can be used in modeling the lattice dynamics of nanostructures. The main advantage of the BvK model is its simplicity and relatively modest calculation resources required, when one goes from bulk materials to nanoscale structures. The BvK model was successfully applied in phononic investigations in different nanomaterials: nanolayers, nanowires, superlattices, graphene, etc. [36-38].

Other phenomenological models of lattice dynamics include VFF model [39] and *adiabatic bond charge* model [40]. In the VFF approach the internal energy of the crystal is expressed in terms of the position of the atoms, the bond lengths between the atoms and the angles between these bonds. Thus all interatomic interactions are seen in terms of bond-stretching and bond-bending forces. In the adiabatic bond charge model the atom is considered a non-polarizable ion core with a shell of valence electrons. The valence charge density is considered as point charges, called bond charges. These two models are generally more complex than the simple BvK model and as a result are harder to modify for low-dimensional structures and require more computational time. Nevertheless, they are considered as an improvement in terms of accuracy of the phonon dispersion relations and in gaining the physical insight into the interatomic interactions in crystals. Both, VFF and adiabatic bond charge models were applied in studying the phonons in different nanostructures [41-42].

In this context, an important direction in lattice dynamics theory of nanostructures is the development of approaches which link the classical force constant models with models based on the interatomic potentials. In Refs. [43-44] I derived simple analytical expressions for the components of force-constant matrices expressed through the parameters of Stillinger-Weber and Keating interatomic potentials [45], which can extend the applicability of the current force constant models for investigation of lattice dynamics of different nanomaterials.

### 1.3. Phonon processes in Si-based nanostructures and graphene

Phonons manifest themselves in all properties of materials: phonons limit electrical conductivity; optical phonons strongly influence optical response, while acoustic phonons carry heat in insulators and semiconductors. Long-wavelength phonons give rise to sound in solids. Spatial confinement of phonons in nanostructures can strongly affect the phonon spectrum and modify phonon properties such as phonon group velocity, polarization, density of states and electron - phonon interaction [46-48]. Thus, nanostructures offer a new way of controlling phonon transport and electron - phonon interaction via tuning phonon dispersion relation, i.e. *phonon engineering*. The idea of engineering phonon dispersion in nanostructures has the potential to be as powerful as the idea of the band-gap engineering for electrons, which is now utilized in a variety of devices. The original phonon engineering concept was first formulated by A. Balandin in 2000 [49].

A topic of special interest in recent years has been thermal transport in nanostructures [50-52]. When the characteristic dimensions of nanostructures such as the diameter of a nanowire or thickness of a nanolayer approach phonon mean free paths, the thermal conductivity can be substantially smaller than the bulk value due to the phonon scattering on sample boundaries. Significant thermal conductivity reductions have been observed in a number of nanoscale systems, including nanowires [53-55], nanotubes [56] and nanolayers [57], and have been widely adopted in thermoelectrics applications [58-60]. Below are reviewed some selected advances of the last decade in studying the phonons and thermal transport in nanostructures. A special attention was paid to the Si-based one-dimensional and two-dimensional nanostructures and graphene.

In Ref. [61] authors have investigated the thickness dependence of the thermal conductivity in ultra-thin free-standing Si nanolayers of high crystalline quality using Raman thermometry. The power absorption coefficient of the membranes was determined experimentally and theoretically calculated. It was found that the thermal conductivity of the layers systematically reduces as their thickness decreases. This was successfully modeled considering the shortening of the phonon mean free path due to the diffuse scattering at the boundaries. The thermal conductivity of the thinnest nanolayer with thickness $d$ = 9 nm resulted in (9 ± 2) $\mathrm{Wm^{-1}K^{-1}}$, which approaches the amorphous limit (~0.01 $\mathrm{Wm^{-1}K^{-1}}$) while still maintaining a high crystalline quality. The authors argued that the obtained results open new possibilities for building thermoelectric modules based on suspended two-dimensional systems.

In Ref. [62] were presented experimental measurements and theoretical calculations of the relaxation times of confined phonons in ultra-thin silicon layers. In Figure 1.7 are presented phonon lifetimes in free-standing silicon layers as a function of phonon frequency. The thick dashed lines show the contributions to the finite phonon lifetime from three-phonon interactions $\tau_{3\text{-}ph}$ and boundary scattering $\tau_b$. The total contribution, calculated using Matthiessen's rule $\tau_T^{-1} = \tau_{3-ph}^{-1} + \tau_b^{-1}$, is shown by the thick solid line. Other models are: intrinsic scattering processes (grey dotted line: Herring [63], grey dashed line: Akhiezer [63]) and extrinsic scattering processes (dot-dashed grey lines: with specularity parameter $p$=0 and $p$=0.95).

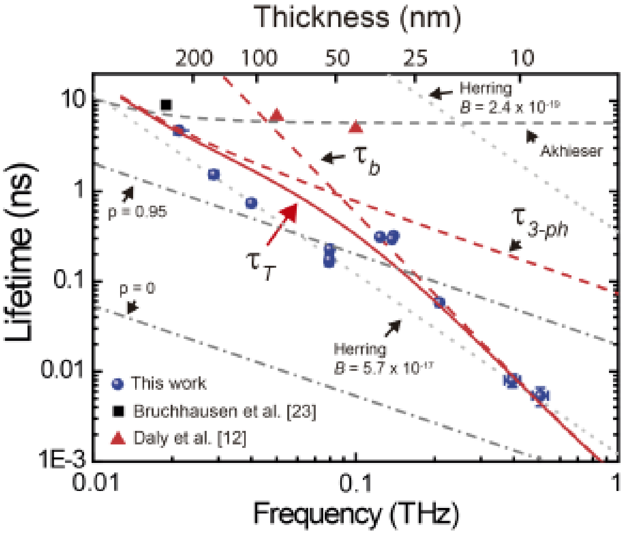

Fig. 1.7. Phonon lifetime of the dilatational mode in free-standing silicon layers as a function of frequency. Experimental data of free-standing silicon nanolayers with thickness values ranging from 222 to 8 nm (circles [62], squares [64],) and bulk silicon (triangles [63]). The figure is taken from Ref. [62].

The relaxation times of the ultra-thin layers were found to be dominated by boundary roughness scattering. In the case of thicker nanolayers, phonon-phonon interactions were predicted to be the dominant scattering processes. The obtained results are important for nanomechanical resonator and thermal transport applications.

In Ref. [65] authors have provided a methodology for predicting phononic gaps in thin semiconductor superlattices. They have shown that several different choices of ultra-thin superlattices possess one-dimensional phononic gaps and that the greater the difference between each layer's vibrational properties the greater is the size of the gaps. The $Si_n/Ge_m$ [001] and $GaAs_n/AlAs_m$ [001] superlattices manifested themselves as one-dimensional *phononic crystals* – artificial periodic structures with controllable phonon properties, with similar results expected for other semiconducting superlattices. It was shown that the gap positions in both these structures vary inversely with the superlattice period. Also, it was presented a method for predicting gap locations in thicker structures once these have been found in thin structures. Quantitative predictions have been made for the positions of the LA and TA gaps with the Ge length fraction $L_f$ in Si/Ge superlattices for the period given by n+m=20, and for GaAs/AlAs structures with differing periods and $L_f=0.5$. It has been shown that the technique can be applied to any superlattice. Furthermore, an empirical formula has been provided for the location of a one-dimensional phononic gap in Si/Ge [001] superlattices for different length fractions and periods:

$$\nu_{gap} = \left(-0.563L_f + 1.406\right)\frac{\bar{L}}{L},$$

where $\nu_{gap}$ is the frequency in terahertz of the center of the gap, $L$ is the superlattice period in nanometers and $\bar{L}=5.54$ nm. It was pointed out that such a relation could be easily found for other superlattices. Moreover, authors have found that the introduction of mass defects has the greatest effect for the high acoustic range in shifting frequencies, but does not close any pre-existing phononic gaps. The results could be useful to both experimentalists and theorists in understanding vibrational and thermal properties of semiconductor superlattices.

In Ref. [66] authors reported on the experimental observation of coherent heat conduction through the use of finite-thickness superlattices with varying number of periods. The measured thermal conductivity increased linearly with increasing total superlattice thickness over a temperature range from 30 to 150 K (see Figure 1.8 below).

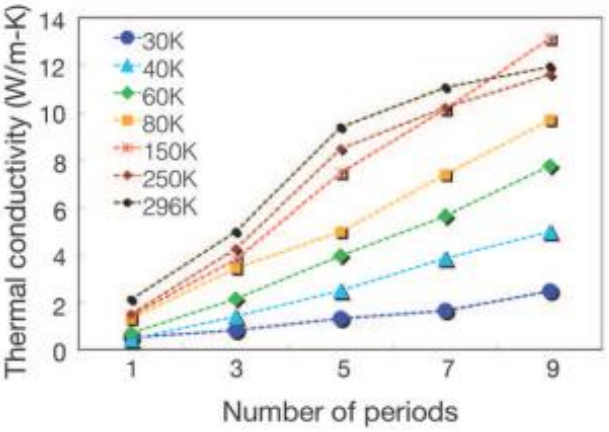

Fig. 1.8. Measured thermal conductivity of GaAs/AlAs superlattices as a function of the number of periods for different temperatures. The figure is taken from Ref. [66].

The performed experimental and theoretical studies showed that most of the phonons that contributed to the measured thermal conductivity in superlattices traversed the structures ballistically and hence were coherent. Interface roughness was effective in destroying the coherence of high-frequency phonons but not effective in scattering low-frequency phonons. The large reduction in thermal conductivity resulted from the loss of coherence of high-frequency phonons, but the lower-frequency phonons that contribute to the thermal conductivity were mostly coherent during their transport through the superlattice structures until they were scattered at the sample’s external boundaries.

In Ref. [67] partial coherent treatment of phonons, where phonons are regarded as either wave or particles depending on their frequencies, was considered. Phonons with mean free path smaller than the characteristic size of phononic crystals were treated as particles and the transport in this regime was modeled by Boltzmann transport equation with phonon boundary scattering taken into account. Phonons with mean free path longer than the characteristic size were treated as waves. In this regime, phonon dispersion relations were computed and it was found that they are modified due to the zone folding effect. The folded phonon spectra were then used to compute phonon group velocity and density of states for thermal conductivity modeling. The presented partial coherent model agreed well with the existent experimental results on in-plane thermal conductivity of phononic crystals and highlighted the importance of zone folding effect on thermal transport in phononic crystals.

In Ref. [68] authors presented atomistic VFF calculations of thermal transport in Si nanowires of diameters from 12 nm down to 1 nm. It was shown that as the diameter is reduced, the phonon density of states and transmission function acquire a finite value at low frequency, in contrast to approaching zero as in the bulk material. This effect is also known as the “problem of long longitudinal waves", which states that the thermal conductivity of a material increases as its length is increased due to the vanishing scattering for long wavelength phonons. The authors of Ref. [68] demonstrated that this thermal transport improvement also appears in nanowires as their diameter is decreased below d=5nm (not only as the length increases) originating from the increase in the density of states of the short wavelength phonon modes. The observation was present under ballistic transport conditions, and further enhanced with the introduction of phonon-phonon scattering. Because of this, in such ultra-narrow nanowires, as the diameter is reduced, phonon transport is dominated more and more by lower energy phonons with longer mean free paths. It was concluded, that almost 80% of the heat is carried by phonons with energies less than 5 meV, most with mean free paths of several hundreds of nanometers.

In Ref. [69] was presented a kinetic model to investigate the anomalous thermal conductivity in silicon nanowires by focusing on the mechanism of phonon-boundary scattering. The developed theoretical model took into account the anharmonic phonon-phonon scattering and the angle-dependent phonon scattering from the nanowire surface. For silicon nanowires with diameter of ~27 nm, it was found that in the case of specular reflection at lateral boundaries, the thermal conductivity increases as the length increases, even when the length is up to 10 mm, which is considerably longer than the phonon mean free path. Thus the phonon-phonon scattering alone was not sufficient for obtaining a normal diffusion in nanowires. However, in the case of purely diffuse reflection at lateral boundaries, the phonons diffused normally and the thermal conductivity converged to a constant when the length of the nanowire was greater than 100 nm. See Figure 1.9 for schematics of phonon scattering processes in nanowires.

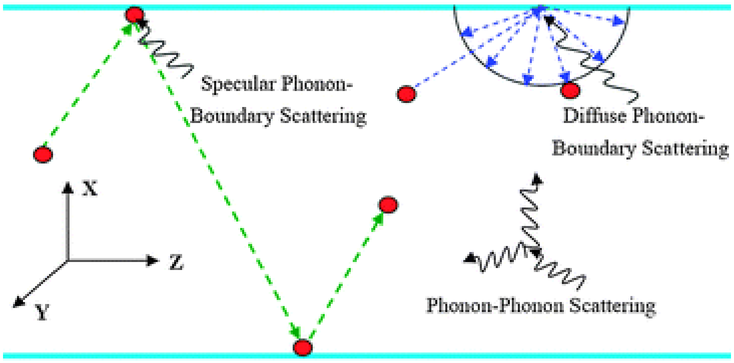

Fig. 1.9. Schematic illustration of phonon scattering in nanowires. The figure is taken from Ref. [69].

These results demonstrate that for observing the length dependence of thermal conductivity experimentally, nanowires with smooth and non-contaminated surfaces, and measuring at low temperature, are preferred.

Another interesting way in controlling the phonon and thermal properties of nanostructured materials was recently demonstrated using *thermocrystals* – periodic structures made of alloys containing nanoparticles [70]. In thermocrystals the heat flow can be managed like sound waves [70]. The basic idea is to manipulate the heat frequency spectrum such that low-frequency phonons carry a considerable part of the heat. In this manner, heat-carrying phonons are subject to coherent reflection and transmission at interfaces, and thus many applications designed for sound management can be applied to heat flow. In thermocrystals [70], high-frequency phonons are blocked by including alloy atoms and nanoparticles (with diameters d ~ 1 nm). The alloy atoms and nanoparticles scatter a wide range of high-frequency phonons. Because high-frequency phonons are severely restricted from carrying heat, the proportion of heat carried by low-frequency phonons increases. To concentrate heat around a specific frequency range the contribution of very low-frequency phonons is also reduced by considering a thin-film material with rough surfaces. As a result of blocking the highest and lowest frequencies, most heat is thus concentrated to a relatively narrow low-frequency band. Specifically, for a $Si_{90}Ge_{10}$ alloy with a 10% filling fraction of d ~ 1 nm Ge nanoparticles, the frequency band is 0.1 THz < $f$ < 2 THz, with up to 40% of the heat restricted to a narrow 'hypersonic' 100-300 GHz range [71]. This matching of the heat frequency spectrum and of the phononic band gaps demonstrates that thermal phonons can be managed through coherent interference effects. Thermocrystals lay the foundation for various applications such as heat waveguides, thermal lattices, heat imaging, thermo-optics, thermal diodes and thermal cloaking [71].

An intriguing example of phonon engineering approach is *phonon thermal rectification*. Thermal rectification refers to a phenomenon predicted for materials systems where thermal conduction in one direction is different from that in the opposite direction [72-75]. Controlling phonon transport by the structure asymmetry, lattice nonlinearity or heterostructuring opens up possibilities, such as a practical realization of the *thermal diode*. Such a device acts as a thermal conductor if a positive thermal bias is applied, while in the opposite case of a negative thermal bias it exhibits poor thermal conduction, thus effectively acting as a thermal insulator. The proposed applications of the thermal rectifier vary from thermal management [73] to information processing [76]. One can distinguish several physical mechanisms leading to thermal rectifications and the corresponding material systems where they can be realized [73, 77-81]. The first type is related to non-linear lattices with strong anharmonicity [75] or asymmetric mass or defect distributions [72, 80]. There have been a number of theoretical predictions of thermal rectifications in such systems [73-74], while there is a lack in experimental data. The second type of thermal rectification is more straightforward and feasible for practical applications. It is pertinent to the asymmetric structures operating in the ballistic or nearly-ballistic phonon transport regime where the acoustic phonon scattering from the boundaries is significant [78]. By modifying the geometry of the structure, introducing asymmetric edges or defects, one can make the phonon-boundary scattering stronger in one direction than in the opposite [78-79]. Another type of the thermal rectification is the use of heterostructures with special focus on interface thermal resistance. Because phonons are strongly scattered due to the mismatch in vibrational properties of the materials forming the interface, which in addition depends on the sign of the applied thermal bias, this produces an asymmetric interface thermal resistance. In Ref. [82] an amorphous silicon - polyethylene thermal rectifier was designed, in which the heat current from the polymer to the silicon was larger than vice versa. To examine the origin of this thermal rectification, the density of states of phonons on each side of the interface was investigated. It was shown, that the phonon density of states significantly softens in the polymer as it becomes warmer. This increases the density of states in the polymer at low frequencies. Thus the transmission probability of those low-frequency acoustic modes in silicon increases, yielding an enhanced thermal transport. The design and the experimental realization of the thermal diode present a striking step toward the practical elaboration of a *thermal transistor* [83], which allows for an *a priori* control of heat flow similar to the control of charge flow in a field-effect transistor. Similar to its electronic counterpart, a thermal transistor would consist of three terminals: the drain, the source, and the gate. When one applies a constant temperature bias between the drain and the source, the thermal current flowing between the source and the drain could be fine-tuned by the temperature that is applied to the gate.

Intense interests for phonon engineering represent carbon nanomaterials. Among them, *graphene* is seen as one of the most perspective candidates for future nanoelectronic and nanophononic applications. Graphene is a two-dimensional material, formed of a lattice of hexagonally arranged carbon atoms. Graphene has generated huge interest since it was first obtained in 2004 [84-85]. Phonons are the main heat carriers in carbon materials including graphene. The first measurements of thermal conductivity of suspended graphene were carried out in 2008 [86-87] and revealed extraordinary high values at RT in the range of 2000 – 5000 W $m^{-1}$ $K^{-1}$, depending on sample size and quality. The experimental observation was explained theoretically by the specifics of the 2D phonon transport [88-90]. It was concluded, that the low-energy acoustic phonons in graphene make a substantial contribution to the heat conduction due to their extraordinary large mean free paths and weak anharmonic scattering [87]. The large values of thermal conductivity make graphene an excellent candidate for heat removal applications. The thermal transport in 2D graphene can be tuned more readily than in the corresponding bulk 3D graphite [91-92]. However, it should be pointed out that the thermal conductivity of the supported graphene is lower than that of suspended and constitutes ~ 600 W

$m^{-1} K^{-1}$ for graphene on $SiO_2$/Si substrate near RT [93], due to the strong phonon-interface and phonon-disorder scatterings [94]. Nevertheless, it is still rather high, exceeding considerably the thermal conductivity of bulk Si (148 W $m^{-1} K^{-1}$) and Cu (400 W $m^{-1} K^{-1}$).

It is interesting to examine the evolution of the thermal properties of *few-layer graphene* with increasing thickness (number of atomic planes, *n*). One has to clearly distinguish two cases: thermal transport limited by (i) intrinsic properties of the few-layer graphene lattice, that is, crystal anharmonicity; and (ii) extrinsic effects, for example, by phonon-boundary or defect scattering. The optothermal Raman study [95] found that thermal conductivity of suspended few-layer graphene decreases with increasing *n*, approaching the bulk graphite limit (see Figure 1.10). This evolution of thermal conductivity was explained by considering the intrinsic quasi-2D crystal properties described by the phonon Umklapp scattering [95]. As number of monolayers *n* increases, the phonon dispersion changes and more phase-space states become available for phonon scattering leading to a decrease in thermal conductivity.

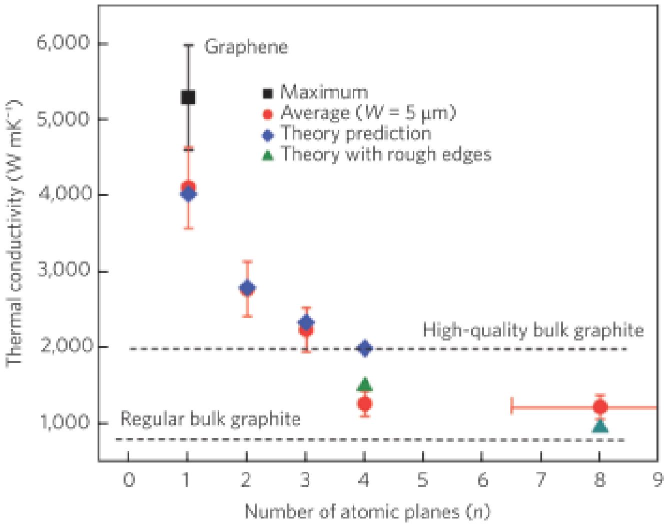

Fig. 1.10. Measured and calculated thermal conductivity of suspended few-layer graphene as a function of number of monolayers *n*. The figure is taken from Ref. [95].

The phonon scattering from the top and bottom boundaries in suspended few-layer graphene is limited if constant *n* is maintained over the layer length. The small thickness ($n < 4$) also means that phonons do not have a transverse component in their group velocity, leading to even weaker phonon-boundary scattering rate from the top and bottom boundaries. In few-layer graphene films with $n > 4$ the boundary scattering can increase, because transverse group velocity is non-zero and it is harder to maintain constant *n* through the whole area of a graphene flake, resulting in thermal conductivity below the graphite limit. The graphite value recovers for thicker films.

An intriguing open question in the theory of phonon transport in graphene is the relative contribution to heat conduction by LA, TA and ZA phonon polarizations (see Figure 1.11 below for phonon dispersion in graphene [38]).

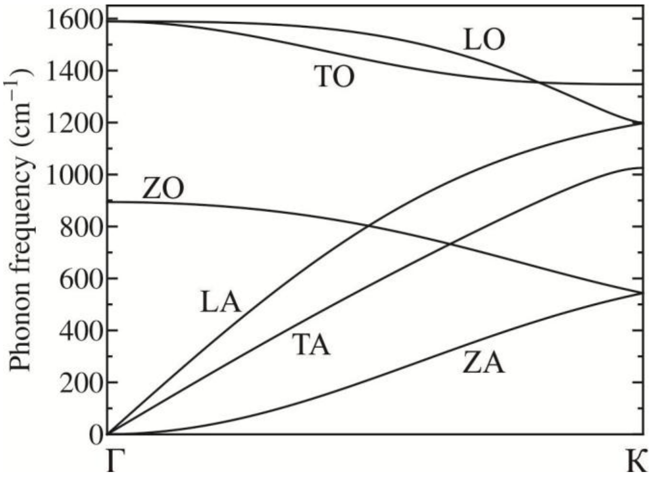

Fig. 1.11. Phonon dispersion in graphene along Γ-K direction.

There have been opposite views expressed as to the importance of ZA phonons, from negligible [91-92, 96] to dominant [90, 93, 97-98]. The argument against ZA contributions originates from the fact that ZA modes have large Gruneisen parameters [92-93] - which defines the scattering strength - and zero group velocity near the zone centre, resulting in a negligible contribution to heat transport [91-92, 96]. The argument for the strong contributions of ZA modes is made on the basis of a selection rule in ideal graphene, which restricts the phase space for phonon-phonon scattering, and increases the lifetime of ZA modes [90]. However, graphene placement on any substrates and the presence of nanoscale corrugations in the graphene lattice can break the symmetry selection rule, which restricts ZA phonon scattering. It is also possible that ZA dispersion undergoes modification, for example, linearization, owing to the substrate coupling.

In Ref. [99] authors have performed molecular dynamics simulations with phonon spectral analysis to predict the mode-dependent phonon relaxation times of suspended and supported graphene at RT. The per-branch phonon relaxation times for both suspended and supported single-layer graphene at 304 K as a function of phonon frequency are shown in Figure 1.12. It was concluded that the majority of LO and TO phonons were found to have relaxation times about 1-4 ps at RT and reduced by about half when put on substrate, which is consistent with the optical phonon relaxation times of supported few-layer graphene measured by Raman spectroscopy [100-102].

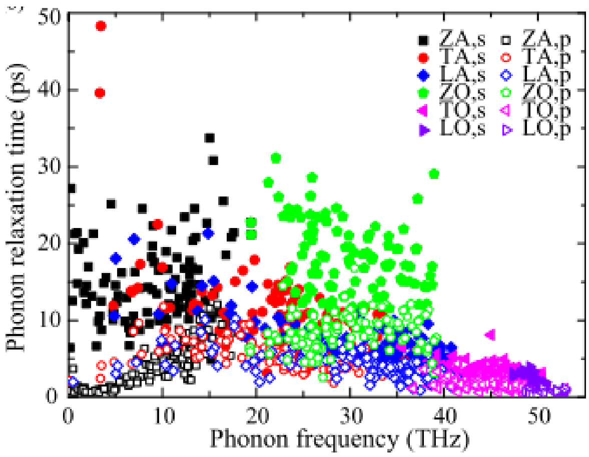

Fig. 1.12. Phonon relaxation times as a function of frequency for all phonon branches. The subscripts “s” and “p” are short for “suspended” and “supported”, respectively. The figure is taken from Ref. [99].

As can be seen from Figure 1.12 in case of low frequency phonons a considerable suppression of their relaxation times was observed. For frequency below 18 THz, the relaxation times values monotonically decreased as frequency continuously reduced to zero, indicating the substrate couples most efficiently to low frequency acoustic phonons. Authors argued that one of the most significant implications of such observation is that the thermal conductivity of supported graphene will not be sensitive to graphene flake size. This is because long wavelength near-zone-center phonons in larger samples would have minimal relaxation times due to substrate scattering and thus would barely contribute to thermal transport. The relaxation time reduction was found to be especially strong for ZA modes. This was due to the fact that the presence of the substrate breaks various symmetries (mirror-reflection, translational, etc.) in single-layer graphene and alters the out-of-plane vibrations by introducing graphene-substrate scattering which largely shortens the relaxation time of ZA phonons. In this case, higher-order anharmonic interactions would be no longer important. As a proof of their findings, authors referred to a Brillouin scattering experiment on multilayer graphene supported on $SiO_2$/Si substrate [103], which suggested that the relaxation times of long wavelength LA/TA phonons are about 10-30 ps, which is shorter than that of suspended graphene, thus in line with the presented conclusions.

In Ref. [104] *ab initio* density functional theory approach was used to calculate the lattice vibration, phonon dispersion and density of states of graphene under uniaxial strain along the zigzag direction. Zigzag and armchair are two typical configurations of graphene along the directions perpendicular or parallel to C-C bonds, respectively. The crystal symmetry and reciprocal lattice were changed under strain, depending on the strain direction. For the ideal graphene, G, M, and K high-symmetry crystallographic points were selected to calculate the phonon dispersion, while G, N, and M points were for the strain along the zigzag direction. The strain was exerted by changing the lattice constant along a given direction and relaxing the atom position in the perpendicular direction. The convergence of the total energy was chosen as $10^{-7}$ eV, and structure optimization was performed until the force acting on each atom was less than 0.01 eV/nm. Supercells with periodic boundary conditions in all directions were utilized to calculate the phonon dispersion curves and density of states of graphene with or without uniaxial strain.

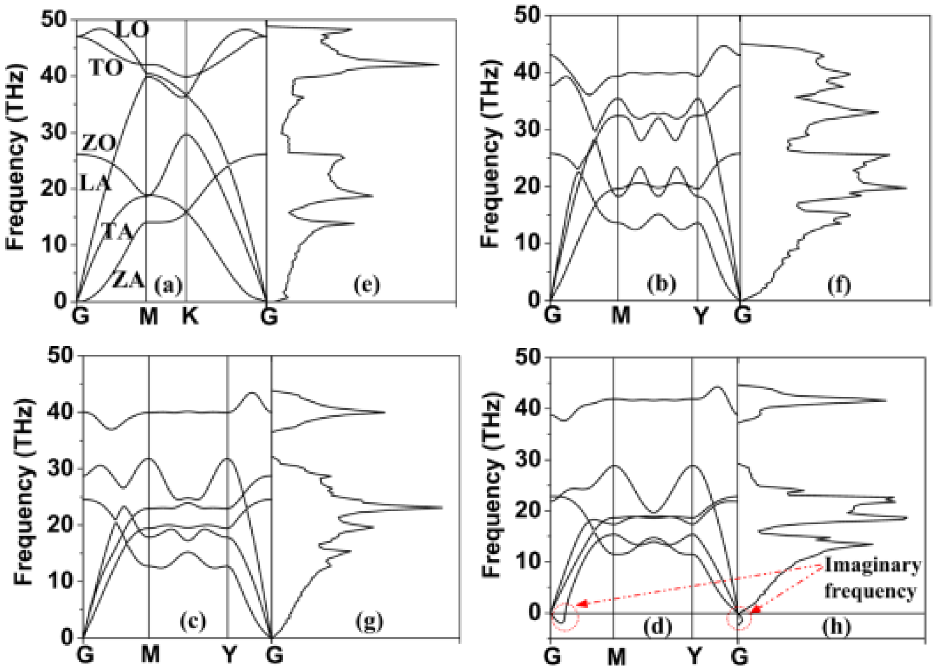

Fig. 1.13. Phonon dispersion curves of graphene under uniaxial strain of (a) 0%, (b) 8%, (c) 16%, and (d) 23% along the zigzag direction, and (e), (f), (g), and (h) present corresponding total density of states. The figure is taken from Ref. [104].

Figures 1.13(a) and 1.13(e) display the phonon dispersion curves and density of states of ideal graphene without strain, respectively. Figures 1.13(b)-1.13(d) depict the phonon dispersion curves of graphene under uniaxial strain of 8%, 16%, and 23% along the zigzag direction; the corresponding phonon density of states is shown in Figures 1.13(f)-1.13(h). Authors noted that the two degenerate optical branches split near the G points due to the reduced crystal symmetry in the presence of lattice strain and that this split becomes more evident at a larger strain. This resulted in a frequency gap of about 10 THz near 35 THz at a strain of about 16%, as was demonstrated in Figures 1.13(c) and 1.13(g). It was concluded, that the phonon modes in this frequency region were forbidden, similar to the band gap in electronic crystals and photonic crystals. This could be utilized in the applications such as thermal rectifiers, thermal transistors, and thermal memories [105]. When the strain increased up to 23%, imaginary frequencies appeared near the G points as indicated by the red arrows in Figures 1.13(d) and 1.13(h). The structure became unstable and the phonon modes were softened. Similar results were obtained when the strain was along the armchair direction, but the instability appeared at 20% strain.

Finally, the important questions are related to the identification of stacking configuration and how the interlayer coupling strength changes for different stacking arrangements and number of layers in few-layer graphene, since its electronic and phononic properties are found to be depended on the number of layers as well as the rotational angle between the interacting sheets of graphene (also known as *twisted graphene*) [38, 106-109]. Recently, it was reported on the observation of low-frequency shear phonon modes in few-layer graphene [110]. Shear modes involve the relative motion of atoms in adjacent graphene planes and provide a direct measurement of the interlayer coupling. The authors of Ref. [110] performed polarized Raman measurements and found a pronounced peak at low-frequency which they denoted as C-peak.

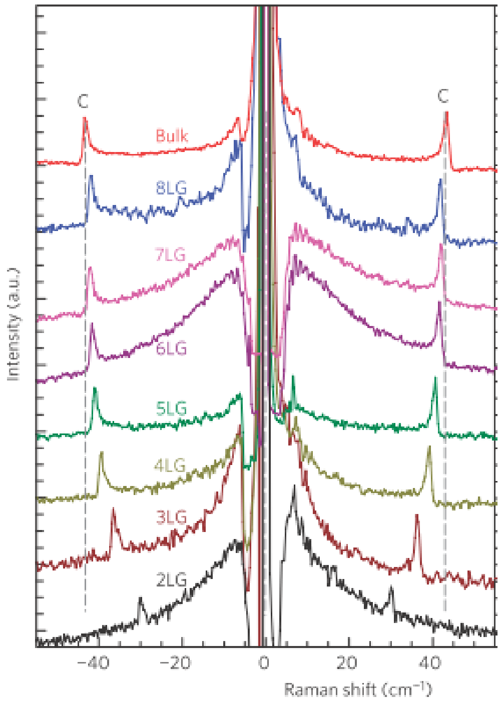

Fig. 1.14. Raman spectra for the C-peak spectral region.

Figure 1.14 plots the Raman spectra for few-layer graphene with increasing thickness. It is seen that position of the C-peak shifts to higher frequencies from two-layer graphene to bulk graphite. Considering a simple linear-chain model and assuming that a layer interacts strongly only with adjacent layers, the analytical expression for C-peak position was obtained:

$$Pos(\mathrm{C})_N = \frac{1}{\sqrt{2}\pi c}\sqrt{\frac{\alpha}{\mu}}\sqrt{1+\cos\left(\frac{\pi}{N}\right)},$$

where $N$ is the number of graphene layers, $\mu$ is the mass per unit area in a graphene sheet, $c$ is the speed of light and $\alpha$ is the interlayer coupling strength. From fitting to the experimental data it was found that $\alpha = 12.8 \times 10^{18}$ N m$^{-3}$. The authors concluded, that the hardening of the C mode when going from bilayer graphene to bulk graphite is not due to a variation of interlayer coupling, but rather to an increase of the overall restoring force i.e. surface layers are less bound in few-layer than in the bulk.

Concluding, one can state that the strong dependence of phonon processes on stacking arrangements and interlayer coupling make few-layer graphene an ideal material for phonon engineering.

## 1.4. Conclusions to chapter 1 and objectives of the Thesis.

The presented highlight on recent theoretical and experimental investigations of electron and phonon processes in graphene and silicon-based nanostructures demonstrate a huge interest from both scientific and engineering community in further developments of nanoelectronic and nanophononic materials and applications. Successful realization of these plans requires the detailed investigation of electron and phonon processes in one-dimensional and two-dimensional nanostructures, as well as determination of novel nanoscale geometries and materials with high electron and phonon engineering abilities. It constitutes the main scientific problem and the **goal** of this Thesis.

In order to achieve this goal, the following **objectives** are formulated:

- Determination of novel one-dimensional and two-dimensional nanostructures with specific geometrical and material parameters, as perspective candidates for electron and phonon engineering.
- Development of theoretical models to describe phonon and electron states in novel one-dimensional and two-dimensional nanostructures.
- Investigation of electron, phonon and thermal properties of novel and generic one-dimensional and two-dimensional nanostructured materials.

The **methods** which are used in order to accomplish the objectives are:

- Lattice dynamics theory for the investigation of phonon processes in novel one-dimensional and two-dimensional nanostructures such as cross-section modulated nanowires and multilayer graphene with different atomic stacking.
- Effective mass approach for the investigation of electrons in novel nanostructures.
- Boltzmann transport equation approach for modeling the thermal properties of novel one-dimensional and two-dimensional nanostructures.

# 2. PHONON PROCESSES IN Si NANOLAYERS AND PLANAR Si/Ge SUPERLATTICES

## 2.1. Born – von Karman lattice dynamics model for nanolayers and planar superlattices

Let us consider a freestanding homogeneous layer and a superlattice made from such layers. The characteristic thickness of the layers is of a few nanometers. The schematic view of the considered structures is shown in Figure 2.1. The *X* and *Y* axes of the Cartesian coordinate system are in the plane of the nanolayer, while the *Z* axis is perpendicular to it. In the *XY* plane the layers are assumed to have infinite size.

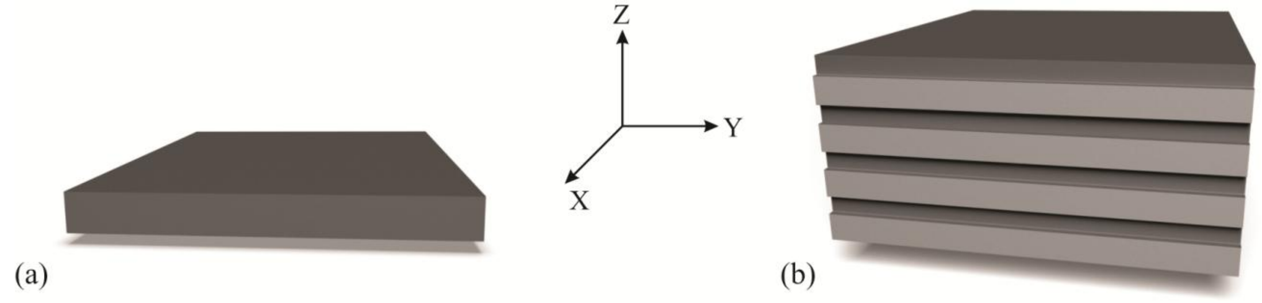

Fig. 2.1. Schematic view of a freestanding homogeneous layer (a) and planar superlattice (b).

The main difference between the nanolayer and bulk material is the absence of translational symmetry along the *Z* axis. Atoms from different monolayers are translationally unequivalent and the amplitude of the atomic displacement is a function of monolayer number $U(s)$, where *s* numerates monolayers. In case of a superlattice the translational symmetry along the *Z* axis is preserved by definition. However, within one translational element (superlattice period) atoms from different monolayers are also translationally unequivalent and the amplitude of atomic displacement is similarly dependent on the monolayer number *s*. As a result, the total number of equations of motion for atoms is determined by the number of monolayers and equals to *3N*, where *N* is the number of monolayers in superlattice period.

In the framework of BvK lattice dynamics theory for nanolayers and planar superlattices, the system of equations of motion for atoms from monolayer *s* can be represented, in a harmonic approximation, as:

$$m_s \omega^2 U_i(s,\vec{q}) = \sum_{j=x,y,z} \sum_{s'=1}^{N} D_{ij}\left(s,s',\vec{q}\right) U_j(s',\vec{q}) \qquad i = x, y, z \tag{2.1}$$

where $s$, $s'$ – numerate monolayers and take values between 1 and *N*, $m_s$ – mass of the atom from monolayer *s*, $\omega$ – phonon frequency, $\vec{q}$ – phonon wavevector, $U_i(s)$ – *i*-th component of the atomic displacement amplitude vector of the *s*-th monolayer, $D_{ij}$ – dynamic matrix element, given by expression:

$$D_{ij}\left(s,s',\vec{q}\right)=\sum_{n'_{s'}}\Phi_{ij}(n_s,n'_{s'})\exp\left(\mathbf{i}\vec{q}\times\left(\vec{r}(n'_{s'})-\vec{r}(n_s)\right)\right), \tag{2.2}$$

where $\vec{r}(n_s)$ – radius-vector of the atom $n_s$ and $\Phi(n_s,n'_{s'})$ – matrix of the force constants describing interaction between a pair of atoms $(n_s,n'_{s'})$. It is taken into account the interaction within two nearest neighbor coordination spheres, therefore the summation in Equation (2.2) is performed over all atoms $n'$ from two nearest spheres of atom *n*. The index *n* here denotes atom lying in the center of the coordination sphere for which the equations of motion are written. One should note also, that atoms *n* and $n'$ can belong to the same monolayer $(n_s,n'_s)$, as well as to the different monolayers $(n_s,n'_{s\pm1})$, $(n_s,n'_{s\pm2})$. The lattice dynamics is described by two force constant matrices: $\Phi(n_s,n'_{s'})=-\begin{pmatrix}\alpha(n_s,n'_{s'}) & \beta(n_s,n'_{s'}) & \beta(n_s,n'_{s'})\\ \beta(n_s,n'_{s'}) & \alpha(n_s,n'_{s'}) & \beta(n_s,n'_{s'})\\ \beta(n_s,n'_{s'}) & \beta(n_s,n'_{s'}) & \alpha(n_s,n'_{s'})\end{pmatrix}$ for the nearest sphere and $\Phi(n_s,n'_{s'})=-\begin{pmatrix}\gamma(n_s,n'_{s'}) & \gamma(n_s,n'_{s'}) & 0\\ \gamma(n_s,n'_{s'}) & \gamma(n_s,n'_{s'}) & 0\\ 0 & 0 & 0\end{pmatrix}$ for the second nearest sphere. Thus, the developed BvK model contains three independent interatomic force constants: $\alpha$, $\beta$ and $\gamma$. In case when interacting atoms $n_s$ and $n'_{s'}$ are from different materials, it is taken the arithmetic average between force constants in corresponding materials. For instance, if Si atom interacts with Ge atom, which takes place on the interfaces of a Si/Ge superlattice, than force constants are calculated according to the following formulas: $\alpha(\text{Si-Ge})=\frac{\alpha_{Si}+\alpha_{Ge}}{2}$, $\beta(\text{Si-Ge})=\frac{\beta_{Si}+\beta_{Ge}}{2}$ and $\gamma(\text{Si-Ge})=\frac{\gamma_{Si}+\gamma_{Ge}}{2}$.

Solving Equations (2.1) in the long-wavelength limit $q\to0$ and approximating the frequency of transverse optic (TO) and longitudinal optic (LO) phonons at the BZ center as $\omega_{LO,TO}(q=0)\approx2\pi\upsilon_{L[100]}/a$, where $\upsilon_{L[100]}=\sqrt{c_{11}/\rho}$ is the longitudinal sound velocity in [100] crystallographic direction, *a* is the lattice constant and $\rho$ is the mass density, the interatomic force constants can be expressed through independent elastic moduli of a bulk crystal $c_{11}$ and $c_{44}$ as: $\alpha=a\pi^2c_{11}/16$, $\beta=\sqrt{\alpha(a(c_{11}-2c_{44})+\alpha)/2}$ and $\gamma=\left(ac_{11}-\alpha\right)/8$. Hence, the proposed

BvK model does not contain any fitting parameters and allows one to simulate phonon properties of different materials with diamond crystal lattice without additional fitting procedures.

An important step in the modeling of the lattice dynamics of nanostructures is the choice of the boundary conditions on external surfaces. In case of a homogeneous nanolayer the external surfaces are considered to be free, i.e. the components of the forces on the surface are equal to zero and therefore $\alpha = \beta = \gamma = 0$. In case of a planar superlattice the external surfaces are absent (the structure is considered infinite along the *Z* axis) and on the superlattice period are applied the periodic boundary conditions in the form: $U(n_{N+1}) = U(n_1)\exp(\mathbf{i}q_z L)$; $U(n_0) = U(n_N)\exp(-\mathbf{i}q_z L)$, where *L* – thickness of one superlattice period.

## 2.2. Phonon processes in Si nanolayers

### 2.2.1. Phonon energy spectra and scattering processes

In order to obtain the phonon energy spectra the system of equations of motion (2.1) with dynamic matrix (2.2) was solved numerically. Diagonalization of the dynamic matrix was performed using standard numerical procedures within double precision LAPACK library. Material parameters and interatomic force constants of silicon used in the calculations are presented in Table 2.1.

Table 2.1. Material parameters and interatomic force constants used in calculations of phonon energy spectra in bulk silicon and silicon nanolayers.

| $a$ (nm) | $\rho$ (kg/m$^3$) | $c_{11}$ (GPa) | $c_{44}$ (GPa) | $\alpha$ (N/m) | $\beta$ (N/m) | $\gamma$ (N/m) |
|---|---|---|---|---|---|---|
| 0.5431 [111] | 2329.0 [111] | 166.0 [112] | 79.6 [112] | 55.6 | 40.6 | 4.3 |

In Figure 2.2 are shown phonon energy spectra in [100] crystallographic direction in bulk silicon (Figure 2.2(a)) and silicon nanolayer with 10 nm thickness (Figure 2.2(b)).

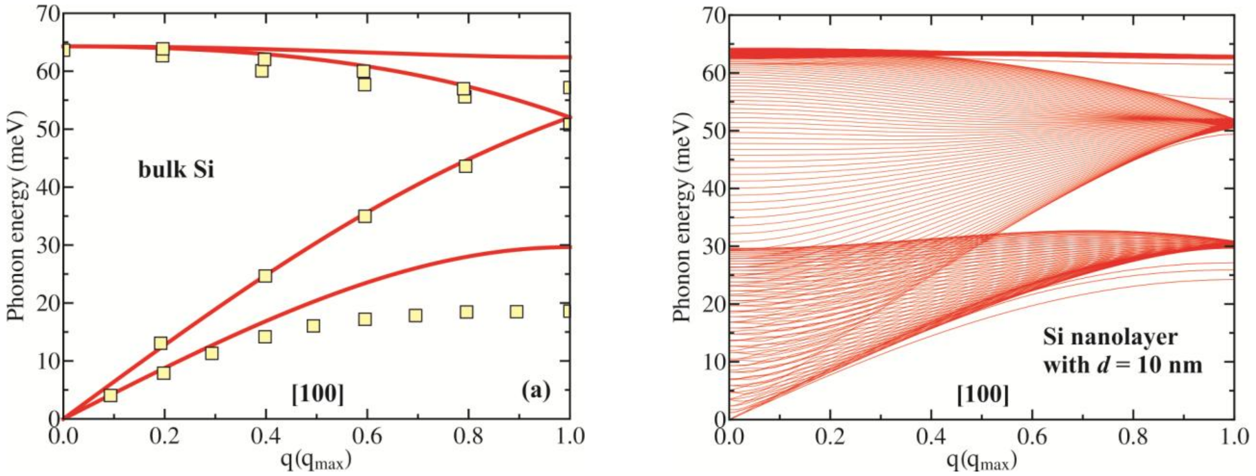

Fig. 2.2. Phonon energy spectra of bulk Si (a) and Si nanolayer with 10 nm thickness (b). Squares denote experimental points from Ref. [113].

It is seen from Figure 2.2(a) that the developed three-parameter BvK model reproduces reasonably well all the features of the bulk silicon phonon spectra, except for the overestimation of TA and TO phonon energies for $q > 0.5 \cdot q_{\max}$, where $q_{\max} = 11.57\ nm^{-1}$. This overestimation is explained by the fact that the short-range interatomic interactions are only considered in this model [114]. The behavior of phonon dispersion curves in the [110] and [111] directions is analogous. In Figure 2.2(b) we present the phonon energy spectra for a Si nanolayer with $d = 10\ nm$ in the [100] crystallographic direction calculated within the BvK model with interatomic force constants from Table 2.1. The strong dimensional confinement along the *Z*-axis results in a quantification of the phonon energy spectra, i.e. the appearance of a large number of size-quantized energy branches. Analogously to the bulk silicon phonon spectrum in nanolayer's spectrum one can distinguish three bunches of phonon branches: TA-like, LA-like and TO(LO)-like branches. However, unlike in the bulk case, where all atomic vibrations are exactly distinguished on transversal/longitudinal and acoustic/optic, in nanolayers appear essentially new transverse-longitudinal acousto-optical mixed vibrations. As a result, a numerous phonon modes in the nanolayers possess low phonon group velocity. Thus these modes do not contribute to the thermal transport. Similar results were also obtained in the framework of continuum approaches [115-116] and different models of lattice vibrations [33, 117-120] for nanolayers and nanowires made from GaN, AlN, Si or Ge material.

In nanolayers it was taken into account two basic mechanisms of phonon scattering: Umklapp phonon-phonon scattering and phonon-boundary scattering. Total scattering time of a phonon with wavevector $\vec{q}$ from *s*-th energy level was calculated according to Matthiessen's rule:

$$\tau_{tot,s}(q) = \left(\tau_{U,s}^{-1}(q) + \tau_{b,s}^{-1}(q)\right)^{-1}, \tag{2.3}$$

where $\tau_{U,s}(q)$ and $\tau_{b,s}(q)$ are phonon lifetimes in Umklapp and boundary scattering process, respectively.

*A) Umklapp scattering processes*

There are two types of phonon-phonon scattering processes: normal (N-processes) and umklapp (U-processes). In N-processes the total momentum of interacting phonons is zero, while in U-processes the total momentum is preserved with a precision of a reciprocal lattice vector $\vec{G}$. The N-processes do not influence on thermal flux directly, but through redistribution of the momentum between heat-carrying phonons. U-processes affect the thermal transport directly, since they change the total momentum of the phonon system. Due to the momentum and energy conservation laws for phonons in silicon the N-processes are significant only at very low temperatures. At medium and high temperatures the U-processes prevail and the N-processes can be disregarded with a good approximation. The most intensive U-processes limiting the heat transfer are scattering processes involving three phonons. Such processes satisfy the following momentum (with a precision of a vector $\vec{G}$) and energy conservation laws:

1) U-processes of the I-st type:

$$\begin{cases} \vec{q} + \vec{q}' = \vec{q}'' + \vec{G} \\ \omega + \omega' = \omega'' \end{cases}$$

These processes can be described as an absorption by phonon $(\vec{q}, \omega)$ of the phonon $(\vec{q}', \omega')$ with creation of the third phonon $(\vec{q}'', \omega'')$ in the second BZ. Or as a decay of a phonon $(\vec{q}'', \omega'')$ from the second BZ into two phonons $(\vec{q}, \omega)$ and $(\vec{q}', \omega')$ in the first zone.

2) U-processes of the II-nd type:

$$\begin{cases} \vec{q} + \vec{G} = \vec{q}' + \vec{q}'' \\ \omega = \omega' + \omega'' \end{cases}$$

Analogously, these processes can be described as a decay of a phonon $(\vec{q}, \omega)$ from second BZ into two phonons $(\vec{q}', \omega')$ and $(\vec{q}'', \omega'')$ in the first zone, or as an absorption by phonon $(\vec{q}', \omega')$ of the phonon $(\vec{q}'', \omega'')$ with creation of a third phonon $(\vec{q}, \omega)$ in the second BZ.

In order to evaluate the scattering time of the phonons in three-particle U-processes of the both types the following model formula from Ref. [119] was used:

$$\tau_{U,s}^{-1}(q) = B\left(\omega_s(q)\right)^2 T \exp\left(-C/T\right), \tag{2.4}$$

According to [119] this form of the Umklapp scattering rate ensures an adequate temperature dependence of the thermal conductivity both at high as well as low temperatures. Parameters *B* and *C* are fitted to reproduce the experimental thermal conductivity of bulk silicon [121].

*B) Phonon-boundary scattering processes*

One of the most significant phonon scattering mechanisms in nanolayers is scattering on external boundaries. For calculation of the phonon-boundary scattering time a phenomenological formula first introduced by Ziman [122] was used:

$$\tau_{b,s}^{-1}(q) = \frac{1-p(q)}{1+p(q)} \frac{|\upsilon_s(q)|}{d}, \tag{2.5}$$

In this approach the *p*-th part of the phonons is reflected specularly from the boundary, while all the other phonons are scattered diffusively, i.e. uniformly in all directions independently on the initial direction of the phonon wave before impact with the boundary. In this context, the parameter *p* characterizes the degree of boundary roughness, namely, the values of *p* close to 0 correspond to a very smooth boundary, while *p* close to 1 correspond to a very rough boundary.

Moreover, it is clear, that boundary roughness parameter *p* should depend on the wavelength of the incident phonon as well as on the boundary (surface) profile. The same surface can be rough for short wavelengths and smooth for long wavelengths. According to authors of Refs. [122-124] the parameter *p* can be determined from the following expression: $p(q) = \exp\left(-2\pi q^2 \delta^2\right)$, where $\delta$ – average height of the surface roughness. This expression was used to calculate the phonon-boundary scattering time from Equation (2.5). This form of the parameter *p* takes into account that when the average height of the surface roughness is much higher than the wavelength of the incident phonon, then the scattering is very strong and phonon "feels" even the smallest surface imperfections. In this case the parameter *p* is close to 0. In the case when phonon wavelength is much larger than $\delta$ then surface details are hardly distinguishable for such waves and the scattering will take place almost specularly with *p* close to 1.

It is important to analyze the phonon scattering mechanisms, determined by Equations (2.4) and (2.5), through their relative influence on thermal conductivity of nanolayers for different temperatures, phonon frequencies and phonon group velocities. First, let us consider the temperature dependence. According to (2.4), at low temperatures the lifetime of phonons in U-processes is large ($\tau_U \to \infty$ when $T \to 0$), while lifetime of phonons in boundary scattering does not depend on temperature and it is the same in the whole temperature range. Due to Matthiessen's rule (2.3) the total phonon scattering time $\tau_{tot}$ is limited by the smallest scattering time, i.e. at low temperatures by the phonon-boundary scattering time $\tau_b$. Thus, in the low-temperature range the dominant mechanism of phonon scattering in nanolayers is scattering on the external boundaries. When temperature rises the Umklapp scattering rate increases and at high temperatures it scales as $\frac{1}{\tau_U} \sim T$. Therefore, in the range of high temperatures the dominant phonon scattering mechanism limiting the thermal conductivity of nanolayers is Umklapp scattering.

Let us consider the dependence of total phonon scattering time on phonon frequency and phonon group velocity. According to Equation (2.4) $\tau_U$ is inverse proportional to the squared phonon frequency, while $\tau_b$ (2.5) is independent on frequency and is inverse proportional to the phonon group velocity. As a result, low-frequency high-speed acoustic phonons practically do not participate in U-processes and mainly scatter on the nanolayer’s external boundaries. In the high-frequency range the picture is opposite, the total phonon lifetime is limited by U-processes as $\tau_{tot} \sim \tau_U \sim \frac{1}{\omega^2}$, which is caused by their weak boundary scattering due to the low group velocity (see Figure 2.2(b), where high-frequency phonons are almost dispersionless).

### 2.2.2. Phonon thermal conductivity

The microscopic definition of the thermal flux is a sum of contributions from all phonons with energy $\hbar\omega_s(\vec{q})$, group velocity $\vec{\upsilon}_s(\vec{q})$ and nonequilibrium distribution function $n_s(\vec{q})$ [88]:

$$\vec{\theta} = \sum_{s,\vec{q}} \hbar\omega_s(\vec{q})\vec{\upsilon}_s(\vec{q})n_s(\vec{q}), \tag{2.6}$$

where $s$ – numerates phonon branches, $\vec{q}$ – phonon wavevector.

According to the Boltzmann transport equation in the relaxation time approximation, phononic nonequilibrium distribution function is given by relation [88]:

$$n_s(\vec{q}) = -(\vec{\nabla}T, \vec{\upsilon}_s(\vec{q}))\tau_{tot,s}(\vec{q})\frac{\partial N_s(\vec{q})}{\partial T}. \tag{2.7}$$

The “–“ sign in the right hand side of the Equation (2.7) shows that thermal flux is directed opposite to the temperature gradient vector $\vec{\nabla}T$, i.e. toward the fastest temperature decrease. In (2.7) $N_s(\vec{q}) = \frac{1}{\exp(\frac{\hbar\omega_s(q)}{k_B T}) - 1}$ – Bose-Einstein equilibrium distribution function, $\tau_{tot,s}(\vec{q})$ – total phonon scattering time, determined by Equations (2.3)-(2.5). Substituting (2.7) in (2.6), for phonon thermal flux we will obtain:

$$\vec{\theta} = -\sum_{s,\vec{q}} \hbar\omega_s(\vec{q})\vec{\upsilon}_s(\vec{q})(\vec{\nabla}T, \vec{\upsilon}_s(\vec{q}))\tau_{tot,s}(\vec{q})\frac{\partial N_s(\vec{q})}{\partial T}. \tag{2.8}$$

From comparison of formula (2.8) with phenomenological definition of thermal conductivity (Fourier law): $\vec{\theta} = -\kappa\,\vec{\nabla}T$, results the following expression for phonon thermal conductivity [88]:

$$\kappa = \sum_{s,\vec{q}} \hbar\omega_s(\vec{q})(\upsilon_s(\vec{q}))^2(\cos\varphi)^2\tau_s(\vec{q})\frac{\partial N_s(\vec{q})}{\partial T}, \tag{2.9}$$

where $\varphi$ – angle between $\vec{q}$ and $X$ axis. In Equation (2.9) was assumed that the thermal flux is directed along the $X$ axis.

Thermal conductivity coefficient $\kappa_{ph}$ is related to the thermal conductivity $\kappa$ through a simple relation: $\kappa_{ph} = \frac{\kappa}{V}$, where $V$ is the volume of the nanolayer. Taking into account two-dimensional phonon density of states one can change in Equation (2.9) the summation over $\vec{q}$ to the integration as: $\sum_{\vec{q}} \to \frac{S}{(2\pi)^2}\iint dq_x dq_y$, where $S$ is the area of one of the nanolayer's surfaces ($S = \frac{V}{d}$, $d$ is the nanolayer thickness). In the approximation of isotropic phonon dispersion in the $XY$ plane the integration can be performed in the polar coordinates: $\iint dq_x dq_y = \int_0^{q_{\max}} q\,dq \int_0^{2\pi} d\varphi$.

Thus, the phonon thermal conductivity coefficient in nanolayers is given by the following formula [88, 125]:

$$\kappa_{ph} = \frac{1}{4\pi k_B T^2 d}\sum_s \int_0^{q_{\max}} (\hbar\omega_s(q))^2(\upsilon_s(q))^2\tau_{tot,s}(q)\frac{\exp(\frac{\hbar\omega_s(q)}{k_B T})}{(\exp(\frac{\hbar\omega_s(q)}{k_B T})-1)^2}q\,dq. \tag{2.10}$$

In Figure 2.3 is presented the comparison between the experimental [121] (black dashed curve) and calculated (gray curve) temperature dependence of the bulk silicon thermal conductivity limited by the Umklapp scattering only.

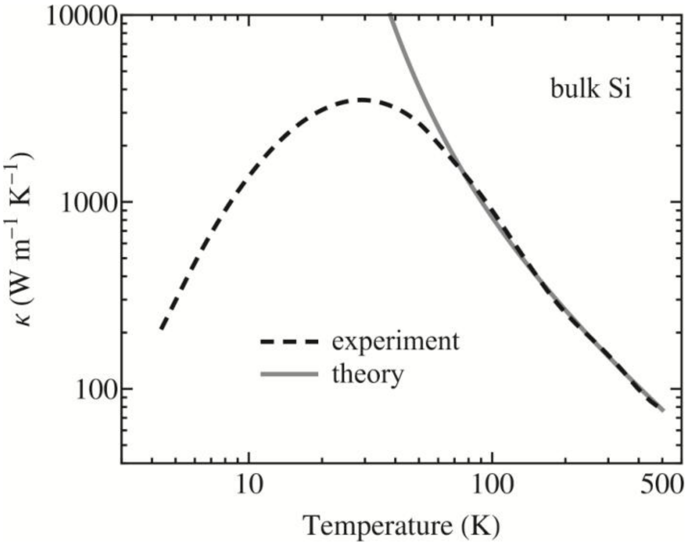

Fig. 2.3. Experimental [121] (black dashed curve) and calculated (gray curve) temperature dependence of the bulk silicon thermal conductivity.

In the considered temperature range the proposed BvK model with the Umklapp scattering parameters $B = 1.76 \times 10^{-19}$ s/K and $C$ = 137.39 K allows one to obtain a good agreement between theoretical and measured thermal conductivity even with overestimated energies of TA and TO phonons for $q > 0.5q_{\max}$, because these phonons weakly participate in the heat transport due to the small group velocities of TO phonons and the strong Umklapp scattering of the short-wavelength TA phonons. Therefore overall correction of the thermal conductivity from them is small. At temperatures T<80 K the experimental thermal conductivity decreases with temperature decrease due to the phonon relaxation on the lattice defects. These mechanisms of the phonon scattering were not accounted in the theory, therefore the difference between theoretical and experimental results reinforces with temperature decrease.

In Figure 2.4 we plot the temperature dependence of the phonon thermal conductivity in silicon nanolayers with $d$ = 5, 10, 20 and 30 nm.

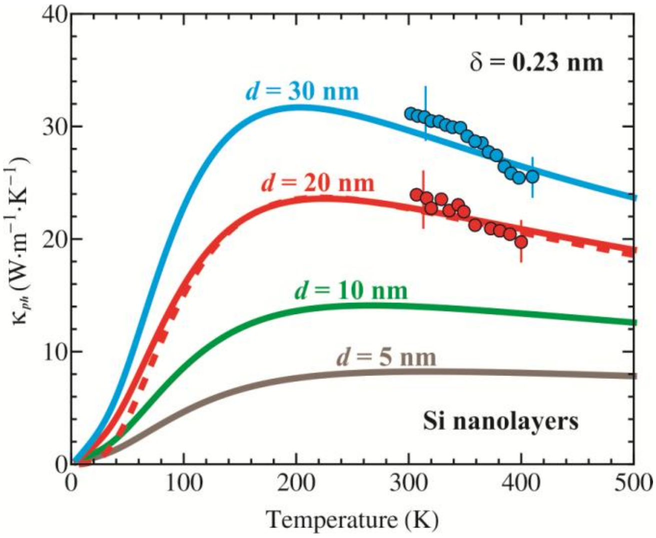

Fig. 2.4. Calculated temperature dependence of the phonon thermal conductivity of silicon nanolayers with $d$ = 5, 10, 20 and 30 nm for average roughness height $\delta = 0.23$ nm. The red dashed line corresponds to the thermal conductivity of 20-nm-thick layer calculated with the constant roughness parameter $p$ = 0.08. The experimental data points from Ref. [126] are also shown for comparison.

In thermal conductivity calculations for silicon nanolayers were used the same Umklapp scattering parameters as in the bulk silicon: $B = 1.76 \times 10^{-19}$ s/K and $C$ = 137.39 K. One should note a sharp drop of thermal conductivity in comparison with bulk case, which is explained by quantification of phonon energy spectrum, decrease of the phonon group velocity and additional scattering of phonons on nanolayer's external boundaries. A drop by a factor of 5 – 20 is found at the RT depending on nanolayer thickness. The experimental data points for nanolayers with $d$ = 20 and 30 nm from Ref. [126] are also shown in Figure 2.4 for comparison. A good agreement is achieved for the average roughness height $\delta$ = 0.23 nm. As one can see from the figure, the maximum thermal conductivity shifts to higher temperatures with decrease of $d$, from $T$ ~ 130 K for 30-nm-thick layer to $T$ ~ 320 K for 5-nm-thick layer. This behavior can be explained as follows: the position of the thermal conductivity maximum separates the low-temperature region, where phonon scattering is mainly due to the boundary, from the high-temperature region, where Umklapp scattering is dominant. In a thinner nanolayer the boundary scattering is stronger in a comparison with a thicker one ($\tau_b \sim d$ according to Equation (2.5)) and dominates up to higher temperatures, therefore the position of the thermal conductivity maximum on the temperature dependence curves shifts to the right. In Figure 2.4 is also shown the thermal conductivity of a 20-nm-thick silicon layer calculated using a momentum-independent roughness parameter $p$ = 0.08 (red dashed line). The results show that the major difference between two approaches with

$p(q)$ and $p = const$ is at low temperatures. These findings are in line with the recent theoretical predictions from Ref. [124]. However phonon scattering on the lattice defects (point defects or dislocations) in real nanoscale structures which is dominant at low temperatures could eliminate the difference between approaches with *p(q)* and *p*=const.

Comparison between the dependencies of the RT thermal conductivity on the nanolayer thickness calculated using BvK (solid and dotted lines) and Face-centered cubic cell (FCC) (dashed lines) models of lattice dynamics is shown in Figure 2.5. The detailed description of the FCC model and its application for the calculation of the phonon energy spectra is presented in Refs. [33, 118, 125].

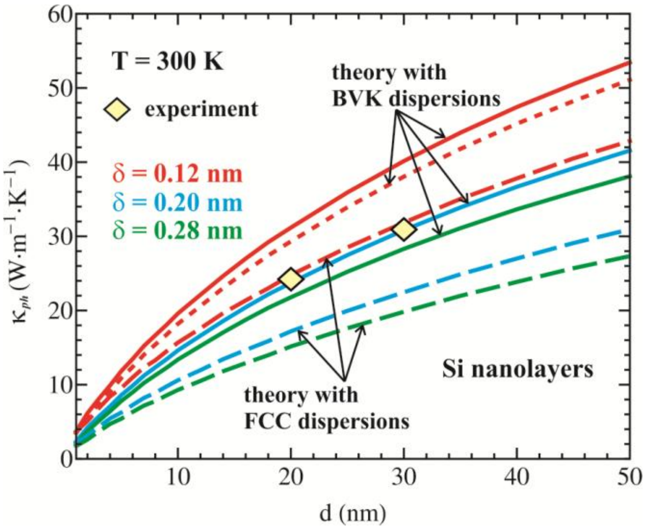

Fig. 2.5. Room temperature phonon thermal conductivity as a function of silicon layer thickness for different values of a boundary roughness parameter $\delta$. The theoretical curves are obtained within BvK model (solid and dotted lines) and FCC model (dashed lines). Dotted line shows the thermal conductivity of acoustic phonon branches only. The experimental data points from Ref. [126] are also shown for comparison.

The results are presented for different values of the boundary roughness parameter $\delta$ =0.12, 0.20 and 0.28 nm. The dotted line shows the thermal conductivity calculated with taking into account the acoustic phonon modes only, i.e. modes with energy $\hbar\omega \leq 50\,\text{meV}$ (see Figure 2.2). The experimental data points for silicon nanolayers with thicknesses $d = 20\,\text{nm}$ and $d = 30\,\text{nm}$ from Ref. [126] are also shown for comparison. The rise of the thermal conductivity with increase of nanolayer thickness is explained by the reduction of the phonon boundary scattering rate. One should note also, that calculations based on both BvK and FCC models reproduce well the available experimental data, but for the different values of $\delta$. The best agreement between BvK calculations and experimental data is obtained for $\delta$ = 0.2 nm, while for the FCC calculations for $\delta$ = 0.12 nm. This discrepancy is attributed to the difference between FCC and

BvK phonon energy dispersions. Note also that for the same values of the boundary roughness parameter the FCC thermal conductivities are smaller than those obtained within BvK model. Growth of the nanolayer thickness leads to the increase of the number of phonon branches. Therefore the difference in the thermal conductivities calculated using FCC and BvK models strongly depends on the layer thickness and increases from ~ 0 % for 1 nm-thick-nanolayer to ~ 20-25 % for 50-nm-thick nanolayer. The lower values of the thermal conductivity obtained in FCC model is explained (1) by a smoother slope of the FCC phonon dispersion branches in comparison with BvK branches and (2) by the taking into consideration acoustic phonon branches only within the FCC model [33, 118].

An interesting question is the contribution of optic phonons in the thermal transport of silicon nanolayers. In order to establish the quantitative estimation of this contribution, in Figure 2.5 is also shown the thermal conductivity curve, obtained taking into account acoustic phonons only (red dotted line). It was found, that the contribution of the optic phonon branches to the thermal conductivity in the considered Si nanolayers constitutes ~ 5 % and is almost independent on the nanolayer thickness. This weak contribution of optic phonons is due to their small group velocities and strong umklapp scattering.

## 2.3. Phonon processes in planar Si/Ge superlattices

### 2.3.1. Phonon energy spectra

Material parameters and interatomic force constants of germanium used in the calculation of phonon energy spectra in Si/Ge planar superlattices are presented in Table 2.2. The material parameters of silicon where taken from Table 2.1.

Table 2.2. Material parameters and interatomic force constants of germanium used in calculations of phonon energy spectra in Si/Ge planar superlattices.

| $a$ (nm) | $\rho$ (kg/m$^3$) | $c_{11}$ (GPa) | $c_{44}$ (GPa) | $\alpha$ (N/m) | $\beta$ (N/m) | $\gamma$ (N/m) |
|---|---|---|---|---|---|---|
| 0.5658 [127] | 5323.4 [127] | 126.0 [128] | 67.7 [128] | 44.0 | 29.2 | 3.4 |

The values of the force constants $\alpha$, $\beta$ and $\gamma$ were adjusted to reproduce the phonon spectra of bulk germanium (see Figure 2.6).

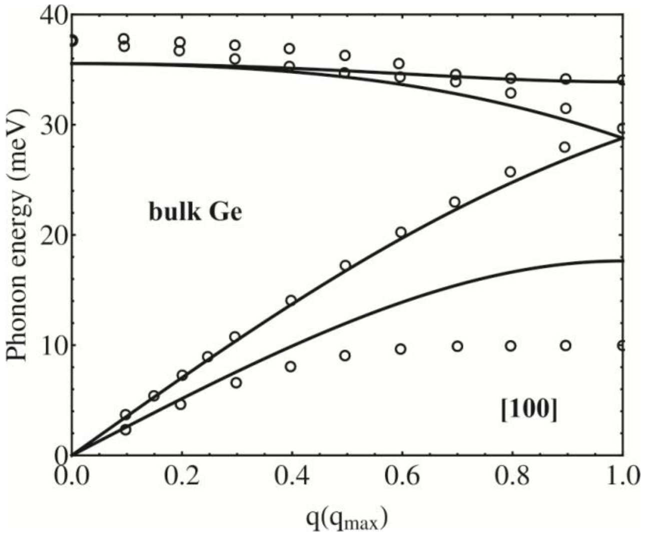

Fig. 2.6. Phonon energy spectrum of bulk Ge in [100] crystallographic direction. Open circles denote experimental points from Ref. [129].

Analogously to the bulk Si case (Figure 2.2(a)), the three-parameter BvK model reproduces reasonably well all the features of the bulk germanium phonon spectra, except for the overestimation of TA phonon energies near the BZ edge, which is caused by the lack of the long-range interatomic interactions in the developed model of lattice dynamics.

In Figure 2.7 the phonon energy spectra in Si(23ML)/Ge(5ML) planar superlattice are shown for two different directions in the BZ.

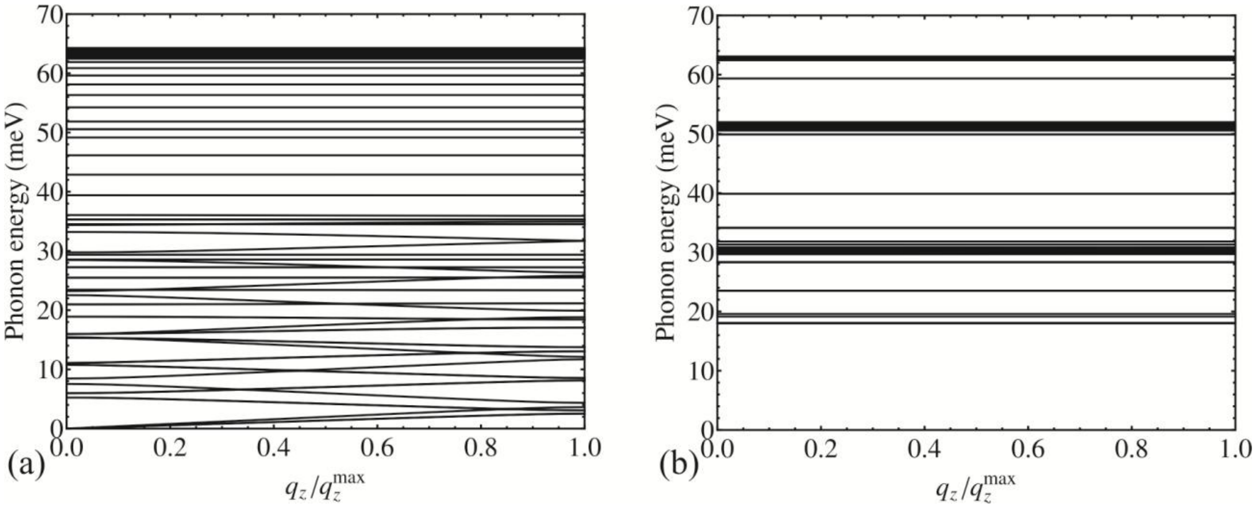

Fig. 2.7. Phonon energy spectra of Si(23ML)/Ge(5ML) planar superlattice in $(0,0,0)\to(0,0,q_z^{\max})$ direction (a) and $(0,q_y^{\max},0)\to(0,q_y^{\max},q_z^{\max})$ direction (b).

One can see from Figure 2.7 that phonon energy spectra in Si/Ge planar superlattices is strongly modified compared to bulk silicon or silicon nanolayers (see Figure 2.2). Due to the superlattice nature of the considered planar Si/Ge nanostructure i.e. the existence of a set of consecutive Si/Ge interfaces and due to the acoustic mismatch between Si and Ge materials, there appear a large number of phonons trapped (localized) in different segments of the superlattice: Si layers, Ge layers or Si/Ge boundary. A clear manifestation of the trapping effect one can found considering the high-energy phonons from Figure 2.7(a). The maximal phonon energy in germanium is ~ 40 meV, therefore all phonon modes in a Si/Ge superlattice with energy more than this value should be localized in Si segments. It is clearly seen from Figure 2.7(a) that phonons with energy more than 40 meV are dispersionless i.e. they posses group velocity close to zero and therefore they are localized in silicon segments of Si/Ge superlattice. Moreover, one can see from Figure 2.7(b) that in directions close to BZ edge the short-wavelength phonons are also dispersionless and posses a very low group velocity.

The peculiarities of the phonon spectra redistribution in Si/Ge planar superlattices in comparison with bulk Si and Ge can be qualitatively estimated from the calculation of the phonon group velocities averaged over entire BZ. In Figure 2.8 is shown the dependence of the average phonon group velocity $\langle\upsilon\rangle(E) = g(E) / \sum_{s(E)} (dE_s / dq_z)^{-1}$ as a function of the phonon energy for Si(23ML)/Ge(5ML) planar superlattice (black solid line), bulk silicon (black dashed line) and bulk germanium (gray solid line). The $g(E)$ is the phonon density of states i.e. the number of phonon modes with energy *E*.

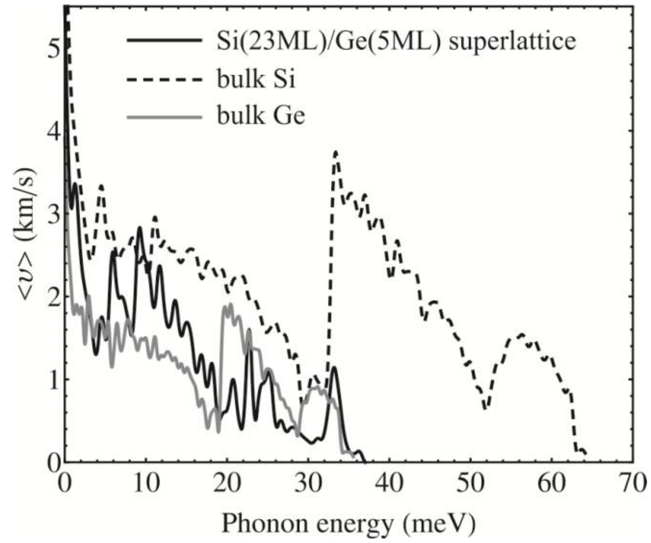

Fig. 2.8. Average phonon group velocity as a function of phonon energy in Si(23ML)/Ge(5ML) planar superlattice (black solid line), bulk Si (black dashed line) and bulk Ge (gray solid line).

The average phonon group velocity in Si/Ge planar superlattice is smaller than that in the bulk silicon for all phonon energies. This drop is explained by the phonon localization effect: the localized phonon modes represent standing waves existing only in the corresponding segments of the Si/Ge superlattice or at the Si/Ge interfaces. Another interesting feature of the Si/Ge superlattice phonon spectrum can be observed in the range of intermediate energies: $30\ \text{meV} < E < 40\ \text{meV}$, where a considerable drop of the average phonon group velocity can be observed. This drop cannot be explained by the localization of these phonon modes in superlattice segments, since phonons of this energy are not filtered by the acoustic mismatch at Si/Ge interface and they exist in the entire Si/Ge structure. The cause of this drop is phonon hybridization effect i.e. phonons of the same energies but of different polarizations and/or from different materials are “mixed” with each other, forming different (hybridized) phonon states with averaged phonon properties. In the considered case, the hybridization takes place between high-velocity TA and LA acoustic “silicon” phonons and low-velocity TO and LO optic “germanium” phonons. As a result, for the considered energy interval a strong decrease of the average phonon group velocity in Si/Ge planar superlattice occurs, as compared to bulk silicon case.

### 2.3.2. Phonon scattering processes. Scattering on Si/Ge interface

To model the phonon scattering processes in real planar Si/Ge superlattices it was taken into account three basic mechanisms of phonon scattering: Umklapp phonon-phonon scattering, scattering on external boundaries (on the bottom and top segments) and scattering on Si/Ge interface. Total scattering time of a phonon with wavevector $\vec{q}$ from *s*-th energy branch was calculated according to Matthiessen’s rule:

$$\tau_{tot,s}(q) = \left(\tau_{U,s}^{-1}(q) + \tau_{B,s}^{-1}(q) + \tau_{I,s}^{-1}(q)\right)^{-1}, \tag{2.11}$$

where $\tau_{U,s}(q)$, $\tau_{B,s}(q)$ and $\tau_{I,s}(q)$ are phonon lifetimes in Umklapp, boundary and interface scattering processes, respectively.

*Umklapp scattering processes*

For calculation of the phonon-phonon Umklapp scattering rate it was used the same formula as for silicon nanolayers (Equation 2.4). However, for Si/Ge superlattice the parameters *B* and *C* were averaged between silicon and germanium values taking into account a particular distribution of the phonon mode in one superlattice period:

$$\frac{1}{\tau_{U,s}(q)} = \tilde{B}_s(q)\ T\ \left(\omega_s(q)\right)^2 \exp\left(-\frac{\tilde{C}_s(q)}{T}\right), \tag{2.12}$$

where

$$\tilde{B}_s(q) = B(Si) \int\limits_{\substack{\text{over Si}\\ \text{segment}}} \left|w_s(z,q)\right|^2 dz \, + \, B(Ge) \int\limits_{\substack{\text{over Ge}\\ \text{segment}}} \left|w_s(z,q)\right|^2 dz \,, \tag{2.13}$$

$$\tilde{C}_s(q) = C(Si) \int\limits_{\substack{\text{over Si}\\ \text{segment}}} \left|w_s(z,q)\right|^2 dz \, + \, C(Ge) \int\limits_{\substack{\text{over Ge}\\ \text{segment}}} \left|w_s(z,q)\right|^2 dz \,. \tag{2.14}$$

In Equations (2.13) and (2.14) $\left|w_s(z,q)\right|$ is the amplitude of the displacement of atoms from $z$-th monolayer in $(s,q)$ vibrational mode. In calculations these amplitudes were normalized to unity: $\int\limits_{\substack{\text{over Si}\\ \text{segment}}} \left|w_s(z,q)\right|^2 dz + \int\limits_{\substack{\text{over Ge}\\ \text{segment}}} \left|w_s(z,q)\right|^2 dz = 1$. In this way, every phonon mode is scattered individually. For example, if 90% of the vibration is localized in Si segment i.e. $\int\limits_{\substack{\text{over Si}\\ \text{segment}}} \left|w_s(z,q)\right|^2 dz = 0.9$ and $\int\limits_{\substack{\text{over Ge}\\ \text{segment}}} \left|w_s(z,q)\right|^2 dz = 0.1$, then the Umklapp scattering parameters will have values close to that of silicon: $\tilde{B}_s(q) = 0.9B(Si) + 0.1B(Ge)$; $\tilde{C}_s(q) = 0.9C(Si) + 0.1C(Ge)$.

*Boundary scattering processes*

In a real superlattice there are no phonons with mean free path larger than the total thickness of the superlattice, because of the scattering of phonons on the external boundaries. This condition is satisfied if one uses for the phonon-boundary scattering lifetime the following formula:

$$\tau_{B,s}^{-1}(q) = \frac{\left|\upsilon_s(q)\right|}{L}, \tag{2.15}$$

where $L$ - total thickness of the superlattice along $Z$ axis.

## Scattering on Si/Ge interface

Let us consider a superlattice consisted of an infinite number of consecutive layers of two materials – A and B. At the A/B (B/A) interfaces there exists a domain, where atoms from A and B materials are intermixed (see Figure 2.9 below). If the perturbation due to such intermixing (mass defect) is weak, then the phonon scattering on the A/B interface can be described using perturbation theory. Let us write the perturbation Hamiltonian for one superlattice period [130]:

$$H' = \frac{1}{2}\sum_{i}^{G(A)} \left(m_i - \bar{m}\right) \left|\frac{\partial \vec{u}_i}{\partial t}\right|^2 + \frac{1}{2}\sum_{j}^{G(B)} \left(m_j - \bar{m}\right) \left|\frac{\partial \vec{u}_j}{\partial t}\right|^2, \tag{2.16}$$

where $G$ - number of intermixed atoms in A and B layers (for the sake of simplicity it is considered the same for both layers, however indices A and B remain for a more clear understanding), $\bar{m}$ - average mass of atoms in superlattice.

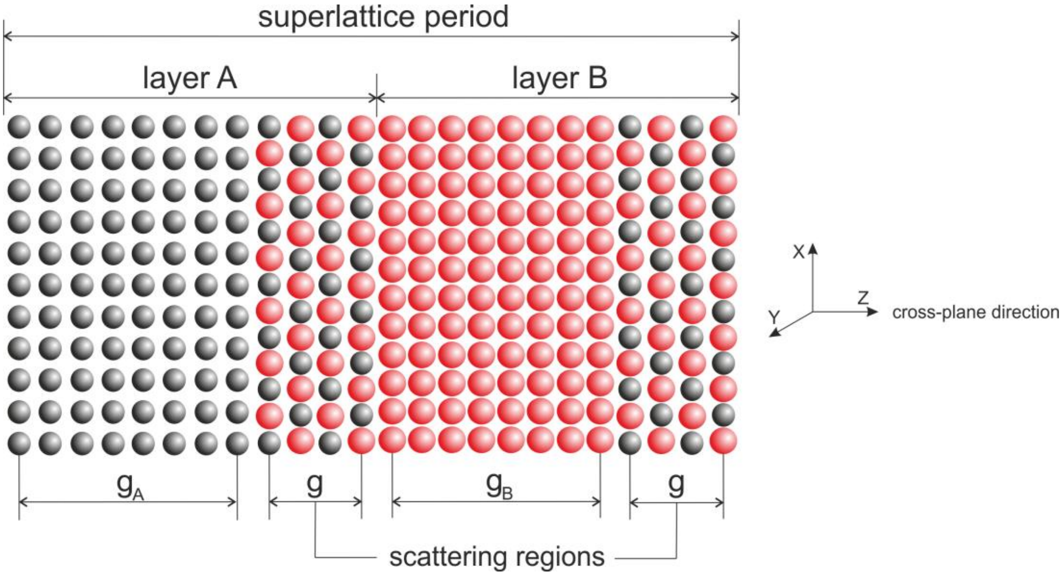

Fig. 2.9. Schematics of a planar superlattice with atomic intermixing at interfaces.

In the second quantization formalism, displacement vector of *i*-th atom is given by expression:

$$\vec{u}_i = -\mathrm{i}\sqrt{\frac{\hbar}{2\bar{\rho}V}}\sum_{\vec{q},s}\frac{\vec{e}_i(\vec{q},s)}{\sqrt{\omega(\vec{q},s)}}\left(b^{+}(\vec{q},s)-b(-\vec{q},s)\right)\exp\left[\mathrm{i}\left((\vec{q},\vec{r}_i)-\omega(\vec{q},s)t\right)\right], \tag{2.17}$$

where $\bar{\rho}$ - average density in one superlattice period, $V$ - volume of one period, $\vec{e}_i(\vec{q},s)$ - vector of the displacement amplitudes corresponding to a vibrational mode $(\vec{q},s)$. The first derivative of (2.17) over time is:

$$\frac{\partial\vec{u}_i}{\partial t} = -\sqrt{\frac{\hbar}{2\bar{\rho}V}}\sum_{\vec{q},s}\sqrt{\omega(\vec{q},s)}\vec{e}_i(\vec{q},s)\left(b^{+}(\vec{q},s)-b(-\vec{q},s)\right)\exp\left[\mathrm{i}\left((\vec{q},\vec{r}_i)-\omega(\vec{q},s)t\right)\right]. \tag{2.18}$$

Substituting (2.18) into the perturbation Hamiltonian (2.16), one can obtain:

$$\begin{aligned}
H' = {} & \frac{\hbar}{4\bar{\rho}V}\sum_{\vec{q},s}\sum_{\vec{q}',s'}\sqrt{\omega(\vec{q},s)\omega(\vec{q}',s')}\left(b^{+}(\vec{q},s)b(\vec{q}',s')-b^{+}(\vec{q},s)b^{+}(-\vec{q}',s')-\right.\\
& \left.-b(-\vec{q},s)b(\vec{q}',s')+b(-\vec{q},s)b^{+}(-\vec{q}',s')\right)\exp\left[-\mathrm{i}\left(\omega(\vec{q},s)-\omega(\vec{q}',s')\right)t\right]\times\\
& \times\left\{\sum_{i}^{G(A)}\left(m_i-\bar{m}\right)\left(\vec{e}_i(\vec{q},s),\vec{e}_i^{\,*}(\vec{q}',s')\right)\exp\left[\mathrm{i}\left(\vec{q}-\vec{q}'\right)\vec{r}_i\right]+\right.\\
& \left.+\sum_{j}^{G(B)}\left(m_j-\bar{m}\right)\left(\vec{e}_j(\vec{q},s),\vec{e}_j^{\,*}(\vec{q}',s')\right)\exp\left[\mathrm{i}\left(\vec{q}-\vec{q}'\right)\vec{r}_j\right]\right\}
\end{aligned} \tag{2.19}$$

The probability of a phonon to go from state $\omega(\vec{q},s)$ into another state $\omega(\vec{q}',s')$ as a result of an interface scattering event can be calculated using the Fermi's golden rule:

$$P_{qs}^{q's'} = \frac{2\pi}{\hbar^2}\left|\left\langle n(\vec{q},s)-1, n(\vec{q}',s')+1\right| H'(\vec{q},s,\vec{q}',s')\left| n(\vec{q},s), n(\vec{q}',s')\right\rangle\right|^2 \delta(\omega(\vec{q},s)-\omega(\vec{q}',s')) \ . \qquad (2.20)$$

In Equation (2.20) delta-function ensures the energy conservation law for all possible transitions $(\vec{q},s)\to(\vec{q}',s')$. The bosonic creation $b^+$ and annihilation $b$ operators act on phonon occupation number $n(\vec{q},s)$ as:

$$\begin{aligned} b^+(\vec{q},s)\left|n(\vec{q},s)\right\rangle &= \sqrt{n(\vec{q},s)+1}\left|n(\vec{q},s)+1\right\rangle \\ b(\vec{q},s)\left|n(\vec{q},s)\right\rangle &= \sqrt{n(\vec{q},s)}\left|n(\vec{q},s)-1\right\rangle \end{aligned} \qquad (2.21)$$

In the matrix element (2.20) the creation and annihilation operators which correspond to a vibrational mode $(\vec{q},s)$ act only on the phononic state $\left|n(\vec{q},s),\_\_\right\rangle$, while operators which correspond to mode $(\vec{q}',s')$ only on the state $\left|\_\_,n(\vec{q}',s')\right\rangle$. Taking into account Equation (2.21), Equation (2.20) will take the form:

$$\begin{aligned} P_{qs}^{q's'} &= 4\frac{2\pi}{\hbar^2}\frac{\hbar^2}{16\bar{\rho}^2V^2}\,\omega(\vec{q},s)\omega(\vec{q}',s')n(\vec{q},s)\left(n(\vec{q}',s')+1\right)\delta(\omega(\vec{q},s)-\omega(\vec{q}',s'))\times \\ &\times\left[\sum_i^{G(A)}\left(m_i-\bar{m}\right)\left(\vec{e}_i(\vec{q},s),\vec{e}_i^{\,*}(\vec{q}',s')\right)\exp\left[\mathrm{i}(\vec{q}-\vec{q}')\vec{r}_i\right]+\right. \\ &\left.+\sum_j^{G(B)}\left(m_j-\bar{m}\right)\left(\vec{e}_j(\vec{q},s),\vec{e}_j^{\,*}(\vec{q}',s')\right)\exp\left[\mathrm{i}(\vec{q}-\vec{q}')\vec{r}_j\right]\right]\times \\ &\times\left[\sum_i^{G(A)}\left(m_i-\bar{m}\right)\left(\vec{e}_i^{\,*}(\vec{q},s),\vec{e}_i(\vec{q}',s')\right)\exp\left[-\mathrm{i}(\vec{q}-\vec{q}')\vec{r}_i\right]+\right. \\ &\left.+\sum_j^{G(B)}\left(m_j-\bar{m}\right)\left(\vec{e}_j^{\,*}(\vec{q},s),\vec{e}_j(\vec{q}',s')\right)\exp\left[-\mathrm{i}(\vec{q}-\vec{q}')\vec{r}_j\right]\right] \end{aligned} \qquad (2.22)$$

Here it was taken into account that in the double sum $\sum_{\vec{q},s}\sum_{\vec{q}',s'}$ there are 2! identical elements $H'(\vec{q},s,\vec{q}',s')$ and $H'(\vec{q}\to\vec{q}',s\to s',\vec{q}'\to\vec{q},s'\to s)$, thus one should multiply the matrix element $P_{qs}^{q's'}$ by $(2!)^2=4$. Opening the brackets in Equation (2.22), one can obtain:

$$\begin{aligned}
P_{qs}^{q's'} &= \frac{\pi}{2\bar{\rho}^2V^2}\,\omega(\vec{q},s)\omega(\vec{q}',s')n(\vec{q},s)\left(n(\vec{q}',s')+1\right)\delta(\omega(\vec{q},s)-\omega(\vec{q}',s'))\times\\
&\times\left[\sum_{i}^{G(A)}\sum_{j}^{G(A)}\left(m_i-\bar{m}\right)\left(m_j-\bar{m}\right)\left(\vec{e}_i(\vec{q},s),\vec{e}_i^{\,*}(\vec{q}',s')\right)\left(\vec{e}_j^{\,*}(\vec{q},s),\vec{e}_j(\vec{q}',s')\right)\exp\left[\mathrm{i}(\vec{q}-\vec{q}')(\vec{r}_i-\vec{r}_j)\right]+\right.\\
&+\sum_{i}^{G(A)}\sum_{j}^{G(B)}\left(m_i-\bar{m}\right)\left(m_j-\bar{m}\right)\left(\vec{e}_i(\vec{q},s),\vec{e}_i^{\,*}(\vec{q}',s')\right)\left(\vec{e}_j^{\,*}(\vec{q},s),\vec{e}_j(\vec{q}',s')\right)\exp\left[\mathrm{i}(\vec{q}-\vec{q}')(\vec{r}_i-\vec{r}_j)\right]+\\
&+\sum_{i}^{G(B)}\sum_{j}^{G(A)}\left(m_i-\bar{m}\right)\left(m_j-\bar{m}\right)\left(\vec{e}_i(\vec{q},s),\vec{e}_i^{\,*}(\vec{q}',s')\right)\left(\vec{e}_j^{\,*}(\vec{q},s),\vec{e}_j(\vec{q}',s')\right)\exp\left[\mathrm{i}(\vec{q}-\vec{q}')(\vec{r}_i-\vec{r}_j)\right]+\\
&\left.+\sum_{i}^{G(B)}\sum_{j}^{G(B)}\left(m_i-\bar{m}\right)\left(m_j-\bar{m}\right)\left(\vec{e}_i(\vec{q},s),\vec{e}_i^{\,*}(\vec{q}',s')\right)\left(\vec{e}_j^{\,*}(\vec{q},s),\vec{e}_j(\vec{q}',s')\right)\exp\left[\mathrm{i}(\vec{q}-\vec{q}')(\vec{r}_i-\vec{r}_j)\right]\right]
\end{aligned}\tag{2.23}$$

The best case scenario is the exact calculation of the matrix element (2.23). However, it is a problem of great complexity, since it requires: (i) knowing the spatial distribution of atoms in mixed layers and their displacement amplitudes vectors, and (ii) summation of a huge number of elements $\sum_{i}^{G}\sum_{j}^{G}=G^2$. Nevertheless, one can greatly simplify the problem if consider the following approximations: (a) segments with mixing atoms have the same crystalline structure as the segments without mixing, (b) all atoms from one particular monolayer have the same amplitudes of the displacements and (c) the number of atoms in monolayers is constant and equals to *N*. In this case, it is convenient to divide the summation $\sum_{i}^{G}$ over atoms in matrix element (2.23) into the summation over monolayers $\sum_{l}^{g}$ (where $g$ - number of monolayers with mixing in segments A and B) and the summation over atoms in a monolayer $\sum_{k}^{N}$. Thus, the first sum from Equation (2.23) can be written as:

$$\begin{aligned}
&\sum_{i}^{G(A)}\sum_{j}^{G(A)}\left(m_i-\bar{m}\right)\left(m_j-\bar{m}\right)\left(\vec{e}_i(\vec{q},s),\vec{e}_i^{\,*}(\vec{q}',s')\right)\left(\vec{e}_j^{\,*}(\vec{q},s),\vec{e}_j(\vec{q}',s')\right)\exp\left[\mathrm{i}(\vec{q}-\vec{q}')(\vec{r}_i-\vec{r}_j)\right]\approx\\
&\approx\sum_{l}^{g(A)}\sum_{n}^{g(A)}\left(\vec{e}_l(\vec{q},s),\vec{e}_l^{\,*}(\vec{q}',s')\right)\left(\vec{e}_n^{\,*}(\vec{q},s),\vec{e}_n(\vec{q}',s')\right)\sum_{k(l)}^{N(A)}\sum_{p(n)}^{N(A)}\left(m_{k(l)}-\bar{m}\right)\left(m_{p(n)}-\bar{m}\right)\times\\
&\times\exp\left[\mathrm{i}(\vec{q}-\vec{q}')(\vec{r}_{k(l)}-\vec{r}_{p(n)})\right]
\end{aligned}\tag{2.24}$$

Here $k(l)$ denotes *k*-th atom from *l*-th monolayer, $\vec{r}_{k(l)}$ - radius-vector of $k(l)$-th atom. Once the displacement amplitudes vectors are taken out from summation over atoms, the calculation of sums $\sum_{k(l)}^{N(A)}\sum_{p(n)}^{N(A)}$ is becoming possible, if one uses the assumption of a random distribution of atoms in monolayers with mixing. Consider as origin of summation the center of a monolayer.

The radius-vectors of atoms can be represented as a sum of two vectors: $\vec{r}_{k(l)}=\vec{R}_l+\vec{r}^{\,||}_{k(l)}$, where $\vec{R}_l$ - vector of *l*-th monolayer, directed perpendicular to it, and $\vec{r}^{\,||}_{k(l)}$ - radius-vector of *k*-th atom from *l*-th monolayer, lying in the monolayer plane. In the chosen representation one can write:

$$\begin{aligned}&\sum_{k(l)}^{N(A)}\sum_{p(n)}^{N(A)}\left(m_{k(l)}-\bar{m}\right)\left(m_{p(n)}-\bar{m}\right)\exp\left[\mathrm{i}(\vec{q}-\vec{q}\,')(\vec{r}_{k(l)}-\vec{r}_{p(n)})\right]=\exp\left[\mathrm{i}(\vec{q}-\vec{q}\,')(\vec{R}_l-\vec{R}_n)\right]\times\\&\times\sum_{k(l)}^{N(A)}\sum_{p(n)}^{N(A)}\left(m_{k(l)}-\bar{m}\right)\left(m_{p(n)}-\bar{m}\right)\exp\left[\mathrm{i}(\vec{q}-\vec{q}\,')(\vec{r}^{\,||}_{k(l)}-\vec{r}^{\,||}_{p(n)})\right]\end{aligned}\tag{2.25}$$

Assuming a random distribution of atoms in monolayers with mixing, one can obtain:

$$\begin{aligned}&\sum_{k(l)}^{N(A)}\sum_{p(n)}^{N(A)}\left(m_{k(l)}-\bar{m}\right)\left(m_{p(n)}-\bar{m}\right)\exp\left[\mathrm{i}(\vec{q}-\vec{q}\,')(\vec{r}^{\,||}_{k(l)}-\vec{r}^{\,||}_{p(n)})\right]=\sum_{k(l)}^{N(A)}\sum_{\substack{p(n)\\ \vec{r}^{\,||}_{k(l)}=\vec{r}^{\,||}_{p(n)}}}^{N(A)}\left(m_{k(l)}-\bar{m}\right)\left(m_{p(n)}-\bar{m}\right)+\\&+\sum_{k(l)}^{N(A)}\sum_{\substack{p(n)\\ \vec{r}^{\,||}_{k(l)}\neq\vec{r}^{\,||}_{p(n)}}}^{N(A)}\left(m_{k(l)}-\bar{m}\right)\left(m_{p(n)}-\bar{m}\right)\exp\left[\mathrm{i}(\vec{q}-\vec{q}\,')(\vec{r}^{\,||}_{k(l)}-\vec{r}^{\,||}_{p(n)})\right]\approx\sum_{k}^{N}\left(m_k-\bar{m}\right)^2\end{aligned}\tag{2.26}$$

The last sum in Equation (2.26) can be calculated as:

$$\begin{aligned}&\sum_{k}^{N}\left(m_k-\bar{m}\right)^2=\left[\sum_{k}^{N}\left(m_k\right)^2\right]-\left[\sum_{k}^{N}2\bar{m}m_k\right]+\left[\sum_{k}^{N}\left(\bar{m}\right)^2\right]=\left[\sum_{k}^{N_A}\left(m_A\right)^2+\sum_{k}^{N_B}\left(m_B\right)^2\right]-\\&-\left[\sum_{k}^{N_A}2\bar{m}m_A+\sum_{k}^{N_B}2\bar{m}m_B\right]+\left[\sum_{k}^{N_A}\left(\bar{m}\right)^2+\sum_{k}^{N_B}\left(\bar{m}\right)^2\right]=\left[N_Am_A^2+N_Bm_B^2\right]-\\&-2\bar{m}\left[N_Am_A+N_Bm_B\right]+\left[N_A\bar{m}^2+N_B\bar{m}^2\right]=N_A\left(m_A-\bar{m}\right)^2+N_B\left(m_B-\bar{m}\right)^2\end{aligned}\tag{2.27}$$

Here $N_A$ and $N_B$ - number of atoms in material A and B in monolayer with mixing, respectively. It is convenient to introduce a parameter *x*, i.e. part of A atoms in a monolayer with mixing. Then one can express the following quantities in terms of *x* and *N*:

$$\begin{aligned}&\bar{m}=\frac{m_Ag_A+m_Bg_B+2g\left(xm_A+\left(1-x\right)m_B\right)}{g_A+g_B+2g};\qquad\bar{\rho}=\frac{\rho_Ag_A+\rho_Bg_B+2g\left(x\rho_A+\left(1-x\right)\rho_B\right)}{g_A+g_B+2g};\\&N_A=xN;\qquad N_B=\left(1-x\right)N;\qquad\sum_{k}^{N}\left(m_k-\bar{m}\right)^2=N\left(x\left(m_A-\bar{m}\right)^2+\left(1-x\right)\left(m_B-\bar{m}\right)^2\right)\end{aligned}\tag{2.28}$$

where $g_A$ and $g_B$ - number of monolayers without mixing in segments A and B correspondingly.

Using Equations (2.25)-(2.28), the matrix element (2.23) takes the form:

$$
\begin{aligned}
P_{qs}^{q's'} &= \frac{\pi}{2\bar{\rho}^2 V^2} N\Delta\bar{\mu}^2 \omega(\vec{q},s)\omega(\vec{q}',s')n(\vec{q},s)\left(n(\vec{q}',s')+1\right)\delta(\omega(\vec{q},s)-\omega(\vec{q}',s'))\times \\
&\times\left[\sum_{l}^{g(A)}\sum_{n}^{g(A)}\left(\vec{e}_l(\vec{q},s),\vec{e}_l^{\,*}(\vec{q}',s')\right)\left(\vec{e}_n^{\,*}(\vec{q},s),\vec{e}_n(\vec{q}',s')\right)\exp\left[\mathrm{i}(\vec{q}-\vec{q}')(\vec{R}_l-\vec{R}_n)\right]+\right. \\
&+\sum_{l}^{g(A)}\sum_{n}^{g(B)}\left(\vec{e}_l(\vec{q},s),\vec{e}_l^{\,*}(\vec{q}',s')\right)\left(\vec{e}_n^{\,*}(\vec{q},s),\vec{e}_n(\vec{q}',s')\right)\exp\left[\mathrm{i}(\vec{q}-\vec{q}')(\vec{R}_l-\vec{R}_n)\right]+ \\
&+\sum_{l}^{g(B)}\sum_{n}^{g(A)}\left(\vec{e}_l(\vec{q},s),\vec{e}_l^{\,*}(\vec{q}',s')\right)\left(\vec{e}_n^{\,*}(\vec{q},s),\vec{e}_n(\vec{q}',s')\right)\exp\left[\mathrm{i}(\vec{q}-\vec{q}')(\vec{R}_l-\vec{R}_n)\right]+ \\
&\left.+\sum_{l}^{g(B)}\sum_{n}^{g(B)}\left(\vec{e}_l(\vec{q},s),\vec{e}_l^{\,*}(\vec{q}',s')\right)\left(\vec{e}_n^{\,*}(\vec{q},s),\vec{e}_n(\vec{q}',s')\right)\exp\left[\mathrm{i}(\vec{q}-\vec{q}')(\vec{R}_l-\vec{R}_n)\right]\right]
\end{aligned}
\tag{2.29}
$$

where $\Delta\bar{\mu}^2 = x\left(m_A-\bar{m}\right)^2+\left(1-x\right)\left(m_B-\bar{m}\right)^2$.

Once the matrix elements are known one can calculate the relaxation time of phonons in interface scattering using the formula [130]:

$$
\tau_{I,s}^{-1}(\vec{q}) = \frac{\sum\limits_{\vec{q}',s'} P_{qs}^{q's'}}{n(\vec{q},s)\left(n(\vec{q},s)+1\right)}. \tag{2.30}
$$

Taking advantage of 2D layered geometry of a planar superlattice one can go from summation over $q'$ to integration using the following scheme:

$$
\sum_{\vec{q}'}\to\frac{1}{\left(2\pi\right)^3}\iiint dxdydz\iiint dq_x'dq_y'dq_z' = \frac{V}{\left(2\pi\right)^2}\int_0^{2\pi/a} q_\perp' dq_\perp' \int_{-\pi/L}^{\pi/L} dq_z'. \tag{2.31}
$$

Substitute Equation (2.31) into Equation (2.30):

$$
\begin{aligned}
\tau_{I,s}^{-1}(q_\perp,q_z) &= \sigma\frac{\Delta\bar{\mu}^2}{4\rho^2\pi}\sum_{s'}\int_{-\pi/L}^{\pi/L}\int_0^{2\pi/a}\omega(q_\perp,q_z,s)\omega(q_\perp',q_z',s')\times \\
&\times\frac{n(q_\perp',q_z',s')+1}{n(q_\perp,q_z,s)+1}\delta(\omega(q_\perp,q_z,s)-\omega(q_\perp',q_z',s'))\times \\
&\times\left[\sum_{l}^{g(A)}\sum_{n}^{g(A)}\left(\vec{e}_l(q_\perp,q_z,s),\vec{e}_l^{\,*}(q_\perp',q_z',s')\right)\left(\vec{e}_n^{\,*}(q_\perp,q_z,s),\vec{e}_n(q_\perp',q_z',s')\right)\exp\left[\mathrm{i}(q_z-q_z')(l-n)\frac{a}{4}\right]+\right. \\
&+\sum_{l}^{g(A)}\sum_{n}^{g(B)}\left(\vec{e}_l(q_\perp,q_z,s),\vec{e}_l^{\,*}(q_\perp',q_z',s')\right)\left(\vec{e}_n^{\,*}(q_\perp,q_z,s),\vec{e}_n(q_\perp',q_z',s')\right)\exp\left[\mathrm{i}(q_z-q_z')(l-n)\frac{a}{4}\right]+ \\
&+\sum_{l}^{g(B)}\sum_{n}^{g(A)}\left(\vec{e}_l(q_\perp,q_z,s),\vec{e}_l^{\,*}(q_\perp',q_z',s')\right)\left(\vec{e}_n^{\,*}(q_\perp,q_z,s),\vec{e}_n(q_\perp',q_z',s')\right)\exp\left[\mathrm{i}(q_z-q_z')(l-n)\frac{a}{4}\right]+ \\
&\left.+\sum_{l}^{g(B)}\sum_{n}^{g(B)}\left(\vec{e}_l(q_\perp,q_z,s),\vec{e}_l^{\,*}(q_\perp',q_z',s')\right)\left(\vec{e}_n^{\,*}(q_\perp,q_z,s),\vec{e}_n(q_\perp',q_z',s')\right)\exp\left[\mathrm{i}(q_z-q_z')(l-n)\frac{a}{4}\right]\right]\times \\
&\times q_\perp' dq_\perp' dq_z'
\end{aligned}
\tag{2.32}
$$

In Equation (2.32) the distance between monolayers was taken equal to $\frac{a}{4}$, which corresponds to a diamond crystal lattice. Also it was introduced a parameter $\sigma$ as an amount of mixing atoms in superlattice. This parameter is the only adjustable parameter of the model and is used to fit the experimental data. Integrating the Equation (2.32) over $q_z'$ finally one can obtain for phonon relaxation time in interface scattering:

$$\begin{aligned}
&\tau_{I,s}^{-1}(q_\perp, q_z) = \sigma \frac{\Delta\bar{\mu}^2}{4\rho^2\pi} \left(\omega(q_\perp, q_z, s)\right)^2 \sum_{q_z', s'} \int_0^{2\pi/a} \frac{1}{\left|\upsilon_z(q_\perp', q_z', s')\right|} \times \\
&\times \Bigg[ \sum_l^{g(A)} \sum_n^{g(A)} \left(\vec{e}_l(q_\perp, q_z, s), \vec{e}_l^{\,*}(q_\perp', q_z', s')\right)\left(\vec{e}_n^{\,*}(q_\perp, q_z, s), \vec{e}_n(q_\perp', q_z', s')\right) \exp\left[ \mathrm{i}(q_z - q_z')(l-n)\frac{a}{4} \right] + \\
&+ \sum_l^{g(A)} \sum_n^{g(B)} \left(\vec{e}_l(q_\perp, q_z, s), \vec{e}_l^{\,*}(q_\perp', q_z', s')\right)\left(\vec{e}_n^{\,*}(q_\perp, q_z, s), \vec{e}_n(q_\perp', q_z', s')\right) \exp\left[ \mathrm{i}(q_z - q_z')(l-n)\frac{a}{4} \right] + \\
&+ \sum_l^{g(B)} \sum_n^{g(A)} \left(\vec{e}_l(q_\perp, q_z, s), \vec{e}_l^{\,*}(q_\perp', q_z', s')\right)\left(\vec{e}_n^{\,*}(q_\perp, q_z, s), \vec{e}_n(q_\perp', q_z', s')\right) \exp\left[ \mathrm{i}(q_z - q_z')(l-n)\frac{a}{4} \right] + \\
&+ \sum_l^{g(B)} \sum_n^{g(B)} \left(\vec{e}_l(q_\perp, q_z, s), \vec{e}_l^{\,*}(q_\perp', q_z', s')\right)\left(\vec{e}_n^{\,*}(q_\perp, q_z, s), \vec{e}_n(q_\perp', q_z', s')\right) \exp\left[ \mathrm{i}(q_z - q_z')(l-n)\frac{a}{4} \right] \Bigg] \times \\
&\times q_\perp' dq_\perp'
\end{aligned} \tag{2.33}$$

In order to calculate the phonon lifetime of interface scattering in a Si/Ge superlattice with Equation (2.33) one should first know the phonon eigenfrequencies and displacement vectors for the whole BZ taking into account the atomic intermixing at interfaces. The intermixing was introduced in the BvK model by changing the force constants between atoms from corresponding layers. For instance, if the *x*-th part of the atoms in monolayers with mixing is Si atoms, then force constants in these monolayers were calculated as:

$$\alpha_{mix} = x\alpha_{Si} + (1-x)\alpha_{Ge}; \quad \beta_{mix} = x\beta_{Si} + (1-x)\beta_{Ge}; \quad \gamma_{mix} = x\gamma_{Si} + (1-x)\gamma_{Ge}. \tag{2.34}$$

In Figure 2.10 are presented phonon lifetimes as a function of wavenumber $q_z$ in Si(35ML)/Ge(9ML) planar superlattice for a fixed wavenumber $q_\perp = 0$ and different phonon branches. The gray lines correspond to the calculations taking into account boundary and umklapp scattering only, while black lines are results of the calculations with boundary and interface scattering.

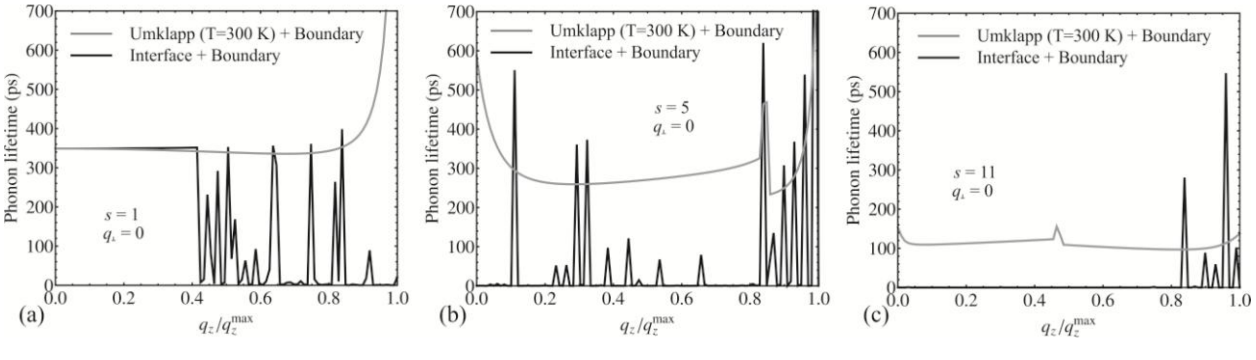

Fig. 2.10. Phonon lifetime as a function of wavenumber $q_z$ in Si(35ML)/Ge(9ML) planar superlattice with 2 ML interface mixing for a fixed wavenumber $q_\perp = 0$ and three different phonon branches: (a) *s*=1, (b) *s*=5 and (c) *s*=11. Total number of branches is 132.

In the calculations of phonon scattering rates were used the following parameters: *T* = 300 K, *L* = 1800 nm, *x* = 0.5, $\sigma$ = 3.1 x $10^8$ and 2 ML interface mixing. The total thickness of the superlattice *L* was taken from experimental work [131] and parameter $\sigma$ was found by fitting the theoretical temperature dependence of the thermal conductivity to the experimental data from [131]. The Figures 2.10(a)-(c) are insightful in terms of particular influence of different phonon scattering mechanisms on total phonon lifetime in Si/Ge planar superlattices. From panel (a) one can see that for the lowest energy branch (*s*=1) the gray and black lines coincide for $q_z < 0.4 q_z^{\max}$, which means that for low-energy long wavelength phonons the boundary scattering mechanism is the only mechanism limiting their mean free path and lifetime. For $q_z > 0.4 q_z^{\max}$ the interface scattering becomes a dominant mechanism of the phonon scattering. Moreover, from panels (b) and (c) one can see that for higher energy branches the interface scattering is the dominant scattering of phonons for all wavelengths. The latter means that interface mass-mixing scattering of phonons plays an extremely important role in the limiting the total phonon lifetime in Si/Ge planar superlattices.

### 2.3.3. Phonon thermal conductivity

Taking into account anisotropy of the phonon energy dispersion in the direction perpendicular to the layers one can go in Equation (2.9) from the summation over $\vec{q}$ to the integration as: $\sum_{\vec{q}} \rightarrow \frac{V}{(2\pi)^3} \iint q_\perp dq_\perp dq_z \int_0^{2\pi} d\varphi$, where *V* is the volume of the planar superlattice. Thus, for calculation of the phonon thermal conductivity in planar Si/Ge superlattices we used the following equation:

$$\kappa_{ph} = \frac{1}{4\pi^2 k_B T^2} \sum_s \int_0^{\frac{\pi}{L_z}} \left\{ \int_0^{\frac{2\pi}{a}} (\hbar\omega_s(\vec{q}))^2 (\upsilon_{z,s}(\vec{q}))^2 \tau_{tot,s}(\vec{q}) \frac{\exp(\frac{\hbar\omega_s(\vec{q})}{k_B T})}{(\exp(\frac{\hbar\omega_s(\vec{q})}{k_B T}) - 1)^2} q_\perp dq_\perp \right\} dq_z \ , \tag{2.35}$$

where $\vec{q}$ – 2D phonon wavevector $\vec{q} = (q_\perp, q_z)$, $\omega_s(\vec{q})$ – phonon frequency of $s$-th branch with wavevector $\vec{q}$, $\upsilon_{z,s}(\vec{q})$ – *z*-th component of the phonon group velocity, $\tau_{tot,s}(\vec{q})$ – total phonon lifetime, $L_z$ – thickness of one superlattice period along $Z$ axis. In Equation (2.35) the BZ was represented as a cylinder with height $\frac{\pi}{L_z}$ along the $Z$ axis and base radius $\frac{2\pi}{a}$ lying in the $XY$ plane. In the $XY$ plane the phonon dispersion is considered to be isotropic.

In order to calculate the thermal conductivity of Si/Ge planar superlattices one first should define the Umklapp scattering parameters for Si and Ge materials from comparison with bulk thermal conductivity data. The Umklapp parameters of silicon were found previously (see Fig. 2.3 from Section 2.2.3). In Figure 2.11 is presented the experimental [121] (black dashed curve) and calculated (gray curve) temperature dependence of the bulk germanium thermal conductivity limited by the Umklapp scattering only.

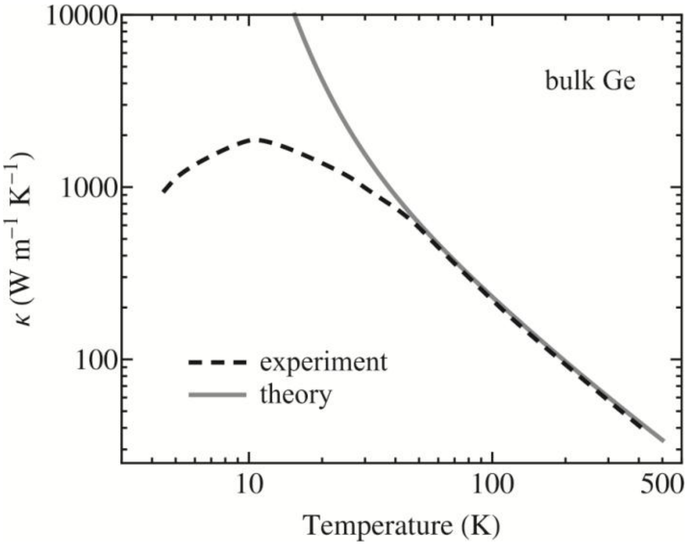

Fig. 2.11. Experimental [121] (black dashed curve) and calculated (gray curve) temperature dependence of the bulk germanium thermal conductivity.

For temperatures 50 K and higher the BvK model with the Umklapp scattering parameters $B = 4.08\times10^{-19}$ s/K and $C$ = 57.6 K allows one to obtain an excellent agreement between theoretical and experimental thermal conductivity. As in the case of bulk silicon, at low temperatures $T$<50 K the experimental thermal conductivity of bulk Ge is substantially lower than Umklapp-limited theoretical one due to the scattering of phonons on the crystal lattice defects.

In Figure 2.12 is presented the calculated phonon thermal conductivity of planar Si(35ML)/Ge(9ML) superlattice as a function of temperature.

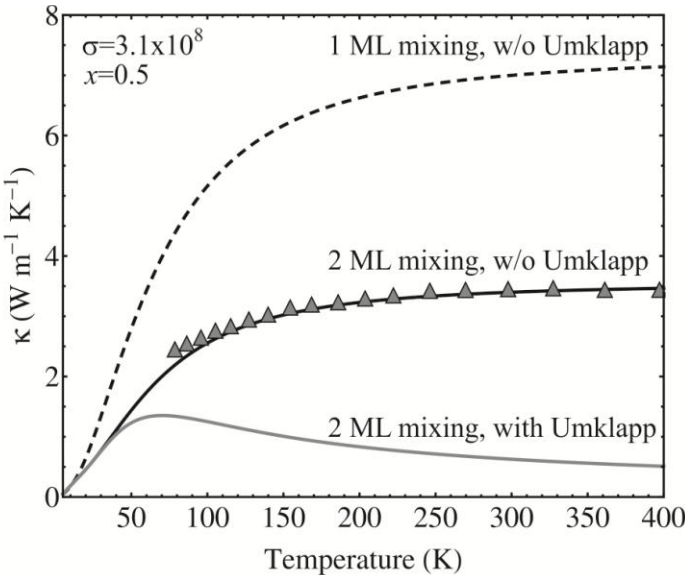

Fig. 2.12. Temperature dependence of the phonon thermal conductivity in Si(35ML)/Ge(9ML) planar superlattice. Gray triangles denote experimental points from Ref. [131].

The black dashed and solid lines correspond to calculations for 1 ML and 2 ML interface mixing without taking into account Umklapp scattering, while solid gray line represents calculation with 2 ML mixing and all three basic mechanisms of phonon scattering. The black solid line was obtained with parameters $x$=0.5 and $\sigma$ = 3.1 x 10$^{8}$ in order to fit the experimental data from Ref. [131]. A good agreement between theoretical and experimental data was obtained only in the case when Umklapp scattering was not accounted in calculations, indicating that in a real Si(35ML)/Ge(9ML) planar superlattice from Ref. [131] the interface mass-mixing scattering is the dominant mechanism of phonon scattering. Indeed, if Umklapp scattering was dominating over interface scattering, then one should find a slow decrease of thermal conductivity at high temperatures, since Umklapp scattering time scales with temperature as $\tau_U \sim T^{-1}$, which is clearly seen from the solid gray curve. However, the experimental data demonstrated no such behavior (follow gray triangles on the figure) and thermal conductivity remained almost independent on temperature. Another important conclusion can be made if one compares black solid and dashed curves i.e. calculations with different number of mixed monolayers at interface. The thermal conductivity of planar Si(35ML)/Ge(9ML) superlattice with 1 ML interface mixing is almost 2 times larger than with 2 ML mixing for a wide range of temperatures, which demonstrates the strongest influence of interface mass-mixing phonon scattering on thermal conductivity of planar Si/Ge superlattices.

In Figure 2.13 is presented the calculated thermal conductivity of Si/Ge planar superlattices as a function of thickness of Si and Ge segments. There are two set of curves: top curves represent calculation without taking into account phonon-interface scattering and bottom curves represent calculation with all basic mechanisms of phonon scattering. The calculations were performed for temperature $T$ = 300 K, interface scattering parameter $\sigma = 10^5$, 1 ML interface mixing and different values of parameter $x$ i.e. different ratios between amount of Si and Ge atoms in mixing regions. The thickness of the superlattice period remained constant and equal to 24 ML (~ 3 nm). In the case when interface scattering of phonons is not taken into account the thermal conductivity possesses its maximal value at $d_{Si}$=20ML and $d_{Ge}$=4ML ($d_{Si}$ and $d_{Ge}$ are thicknesses of silicon and germanium segments, respectively), i.e. when Ge segment is much thinner than the Si one. It is an expected result since silicon material possesses better thermal conduction properties than germanium. On the contrary, when phonon-interface scattering is included in calculations the thermal conductivity have a distinguished maximum when $d_{Si} = d_{Ge}$ = 12 ML. This peculiar behavior differs significantly from the case where phonon-interface scattering was not taken into account (top curves). It is attributed to the non-trivial dependence of the interface scattering rate on the amplitudes of the atomic displacements in Si/Ge superlattices (see Equation 2.32). The atomic displacement field can change significantly for different vibrational modes and different ratios between thicknesses of Si and Ge segments, because of the strong acoustic mismatch and different vibrational properties of the materials.

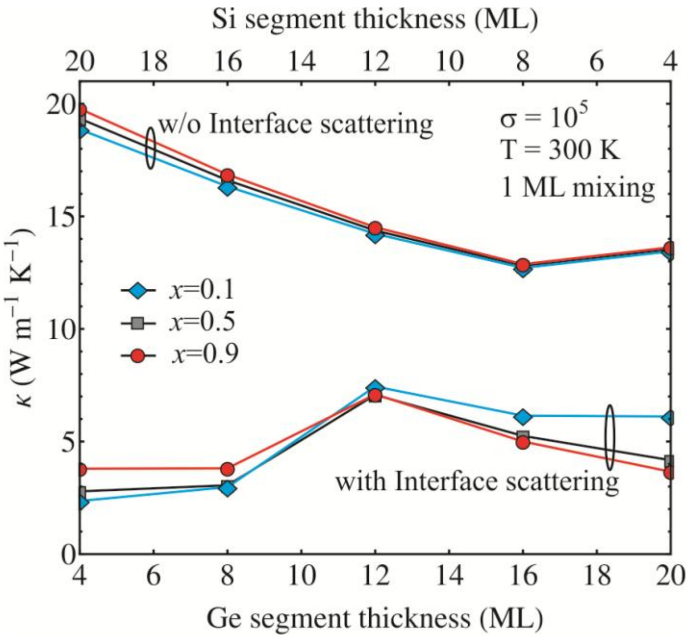

Fig. 2.13. Room-temperature thermal conductivity of Si/Ge planar superlattices with constant period $L_z$=24 ML and different ratio between thicknesses of Si and Ge segments.

Another valuable conclusion from Figure 2.13 can be made about the dependence of thermal conductivity on the parameter $x$ when all basic mechanisms of phonon scattering are accounted in calculations (bottom curves). In Si/Ge superlattices with thin Ge segments the thermal conductivity for $x$=0.9 (red curve) case is higher than for $x$=0.5 (black curve) and $x$=0.1 (blue curve) cases. In Si/Ge superlattices with thin Si segments there is opposite situation, the thermal conductivity for $x$=0.1 is higher than for $x$=0.5 and $x$=0.9 cases. It is attributed to the specifics of interface scattering of phonons, since in the case when the interface scattering is not taken into account (top three curves) the thermal conductivity do not demonstrate such behavior. The results suggest that Ge atoms act as strong scatterers of Si-like phonons when $d_{Si}>>d_{Ge}$. In this case phonon-interface scattering rate is larger for smaller values of $x$ i.e. for larger amount of Ge atoms in interface layers with mixing. When Ge segments are much thicker than Si segments the situation is opposite and Si atoms at the interface strongly scatter Ge-like phonons.

## 2.4. Conclusions to chapter 2

In this chapter a three-parameter BvK model of lattice dynamics for nanolayers and planar superlattices with diamond crystal lattice was developed. The Boltzmann transport equation approach was proposed for investigation of the phonon and thermal processes in Si nanolayers and Si/Ge planar superlattices.

For nanometer-wide silicon nanolayers a good agreement between theoretical calculations and the experimental data for 20-nm-thick and 30-nm-thick silicon nanolayers was obtained. It was demonstrated that optical phonons contribution to the thermal conductivity of silicon nanolayers under consideration constitutes only a few percent.

The perturbation theory and second quantization formalism were used in order to model the scattering of phonons on interfaces in Si/Ge planar superlattices. It was concluded that interface mass-mixing scattering of phonons plays an extremely important role in the limiting the total phonon lifetime in Si/Ge planar superlattices and can lead to a peculiar behavior of phonon thermal conductivity of these structures owing to the non-trivial dependence of the interface scattering rate on the amplitudes of the atomic displacements. For a wide temperature range from 50 K to 400 K a good agreement between theoretical and experimental phonon thermal conductivity was obtained for Si(35ML)/Ge(9ML) planar superlattice when phonon-phonon scattering was not taken into account, indicating that the interface mass-mixing scattering can be the dominant mechanism for the phonon scattering in real Si/Ge planar superlattices.

The proposed theoretical approaches allow better understanding of the phonon processes in 2D homogeneous layers and acoustically-mismatched heterostructures with diamond crystal lattice and can be highly useful for an accurate predictive simulation of their phonon and thermal properties.

# 3. PHONON AND ELECTRON PROCESSES IN Si-BASED MODULATED NANOWIRES

## 3.1. Effective mass method and electron energy spectra in Si/SiO$_2$ core/shell modulated nanowires

Despite the technological difficulties, modulated nanowires (modulated NWs or MNWs) have been successfully synthesized during the past few years, using electron deposition in pores of different materials, thermal evaporation and chemical vapor deposition [132-135]. Experimental successes stimulate the investigation of physical properties of modulated structures. Electronic states and ballistic electron transport in Si and GaAs MNWs have been theoretically investigated in Refs. [136-140] in the framework of effective mass method and density functional theory. It was demonstrated [139-140] that cross-section modulation with only a few quantum dots leads to an appreciable enhancement of electron conduction properties of GaAs nanowires.

In Figure 3.1 is shown the schematic view of considered core/shell nanowires. Nanowires consist of two periodically repeated Si segments with dimensions $d_x^1 \times d_y^1 \times l_z^1$ and $d_x^2 \times d_y^2 \times l_z^2$ covered by SiO$_2$ shell.

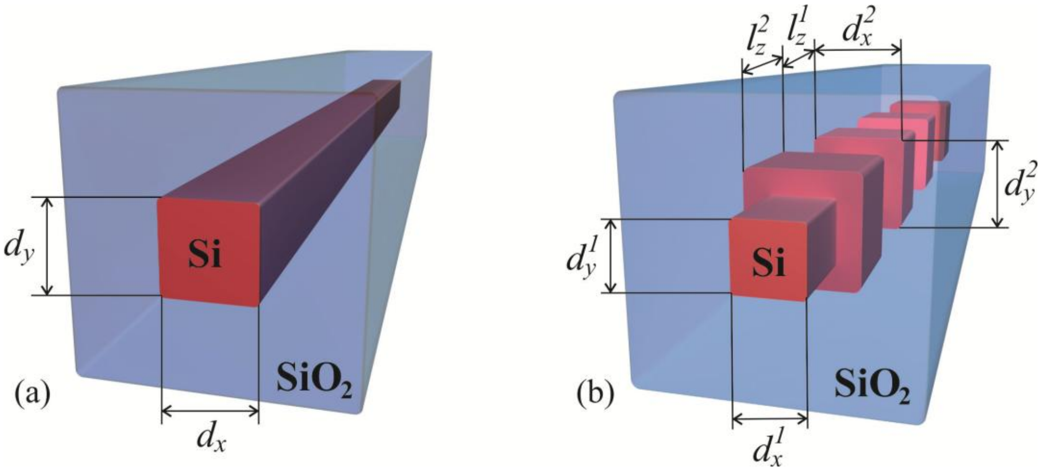

Fig. 3.1. Schematics of a Si nanowire with constant cross section (a) and periodically cross-section modulated Si nanowire (b). Both wires are covered with a SiO$_2$ shell.

Electron states in these structures are described with time-independent Schrodinger equation:

$$\hat{H}\Psi_n = E_n \Psi_n, \tag{3.1}$$

where $E_n$ and $\Psi_n$ is electron energy and electron wave function with quantum number *n*, respectively. Since NW with constant cross-section can be considered as a particular case of a

MNW (when cross-section of different segments is equal), then it can be obtained a general form of electronic Hamiltonian $\hat{H}$ for both modulated and unmodulated nanowires.

Let us direct the *Z* axis of the Cartesian coordinate system along the NW, while *X* and *Y* axes in the NW's cross-sectional plane. For a chosen coordination scheme the electronic Hamiltonian in the effective mass approximation takes the form:

$$\hat{H} = -\frac{\hbar^2}{2}\left[\frac{\partial}{\partial x} M_{\perp}(x,y,z)\frac{\partial}{\partial x} + \frac{\partial}{\partial y} M_{\perp}(x,y,z)\frac{\partial}{\partial y} + \frac{\partial}{\partial z} M_{\parallel}(x,y,z)\frac{\partial}{\partial z}\right] + V_b(x,y,z)\,, \tag{3.2}$$

where $\hbar$ is the Planck constant, $V_b(x,y,z)$ is potential barrier in $(x,y,z)$ point, $M_{\perp}(x,y,z)$ and $M_{\parallel}(x,y,z)$ is transversal and longitudinal electron effective masses. Transversal and longitudinal electron effective masses in Si are equal to $0.19\,m_e$ and $0.98\,m_e$, correspondingly, where $m_e = 9.10938215\times10^{-31}$ kg is electron mass in vacuum. Equation (3.1) with Hamiltonian (3.2) represents an eigenvalue problem, with electron energies as eigenvalues and electron wave functions as eigenvectors. For the numerical solution of this problem a discretization of equations (3.1-3.2) was performed. Thus, a point in continuum space with coordinates $(x,y,z)$ was mapped into a point with coordinates $(i,j,k)$ in discrete space. The discrete indices can have values: $i=1,...,N_x$; $j=1,...,N_y$ and $k=1,...,N_z$, where number of discrete points along the corresponding axes was taken equal to $N_x=15$, $N_y=15$ and $N_z=8$.

Applying a finite difference method for derivatives from equation (3.2), the equation (3.1) takes the form:

$$\begin{aligned}
&\Psi_n(i,j,k)\left[\frac{\hbar^2}{\Delta x^2}M_{\perp}(i,j,k)+\frac{\hbar^2}{\Delta y^2}M_{\perp}(i,j,k)+\frac{\hbar^2}{\Delta z^2}M_{\parallel}(i,j,k)+V_b(i,j,k)-E_n\right]+\\
&+\Psi_n(i+1,j,k)\left[-\frac{\hbar^2}{8\Delta x^2}\big(M_{\perp}(i+1,j,k)-M_{\perp}(i-1,j,k)\big)-\frac{\hbar^2}{2\Delta x^2}M_{\perp}(i,j,k)\right]+\\
&+\Psi_n(i-1,j,k)\left[\frac{\hbar^2}{8\Delta x^2}\big(M_{\perp}(i+1,j,k)-M_{\perp}(i-1,j,k)\big)-\frac{\hbar^2}{2\Delta x^2}M_{\perp}(i,j,k)\right]+\\
&+\Psi_n(i,j+1,k)\left[-\frac{\hbar^2}{8\Delta y^2}\big(M_{\perp}(i,j+1,k)-M_{\perp}(i,j-1,k)\big)-\frac{\hbar^2}{2\Delta y^2}M_{\perp}(i,j,k)\right]+\\
&+\Psi_n(i,j-1,k)\left[\frac{\hbar^2}{8\Delta y^2}\big(M_{\perp}(i,j+1,k)-M_{\perp}(i,j-1,k)\big)-\frac{\hbar^2}{2\Delta y^2}M_{\perp}(i,j,k)\right]+\\
&+\Psi_n(i,j,k+1)\left[-\frac{\hbar^2}{8\Delta z^2}\big(M_{\parallel}(i,j,k+1)-M_{\parallel}(i,j,k-1)\big)-\frac{\hbar^2}{2\Delta z^2}M_{\parallel}(i,j,k)\right]+
\end{aligned} \tag{3.3}$$

$$+\Psi_n(i,j,k-1)\left[\frac{\hbar^2}{8\Delta z^2}\left(M_{\|}(i,j,k+1)-M_{\|}(i,j,k-1)\right)-\frac{\hbar^2}{2\Delta z^2}M_{\|}(i,j,k)\right]=0$$

It is supposed, that considered core/shell Si/SiO$_2$ nanowires are suspended in vacuum and are infinite along the *Z* axis and in *XY* plane have nanometric dimensions. In this case the following boundary conditions are applied:

$$\begin{cases}\Psi_n(N_x+1,j,k)=\Psi_n(0,j,k)=0\\ \Psi_n(i,N_y+1,k)=\Psi_n(i,0,k)=0\\ \Psi_n(i,j,N_z+1)=\Psi_n(i,j,1)e^{ik_zL_z}\\ \Psi_n(i,j,0)=\Psi_n(i,j,N_z)e^{-ik_zL_z}\end{cases}, \tag{3.4}$$

where $L_z$ is the length of one period of NW along the *Z* axis; $k_z$ is electron wave number along the *Z* axis. Equation (3.3) with boundary conditions (3.4) determines electron energy and wave function in ($n$,$k_z$) state.

In Figure 3.2 are shown ten lowest electron energy branches in Si NW with constant cross-section $d_x \times d_y$ = 9x9 nm$^2$ and Si MNW $d_x^1 \times d_y^1 \times l_z^1$=5x5x1 nm$^3$; $d_x^2 \times d_y^2 \times l_z^2$=9x9x1 nm$^3$. Both wires are covered with SiO$_2$ shell in such a way that total cross-sectional dimensions are equal to 15x15 nm$^2$.

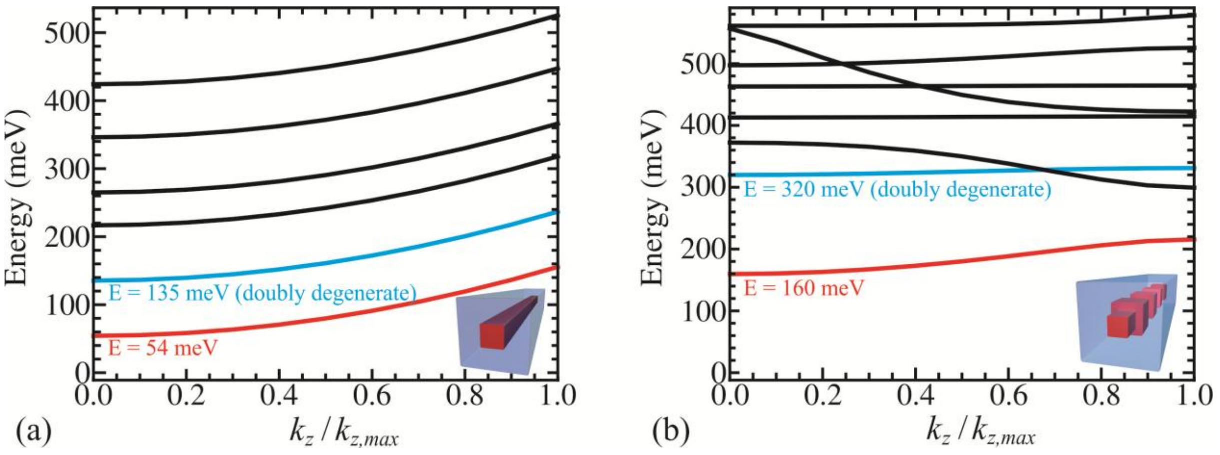

Fig. 3.2. Electron energy dispersion in Si nanowire with constant (a) and periodically modulated (b) cross-section, covered with SiO$_2$ shell.

Due to the nanometric cross-sectional dimensions of the considered wires, electron motion in *XY* plane is quantified and its energy can have only discrete values. In case of Si NW with constant cross-section the electron motion along the NW axis remains free and is described by a parabolic energy dispersion (see panel (a) in Figure 3.2). In case of a Si NW with modulated cross-section (panel (b) in Figure 3.2) there is a significant deviation from parabolic law, which indicates that electron motion along the *Z* axis is not free and a part of electron wave function being localized in wide segments of the modulated wire. One can observe also that lowest energy levels in MNW possess higher energy compared to generic NW, suggesting that electron confinement in nanowires with modulation manifests itself more strongly.

In Figure 3.3 is presented modulus of the electron wave function for lowest (ground) state in Si NW with constant cross-section 9x9 nm$^2$ and Si MNW 5x5x1-9x9x1 nm$^3$.

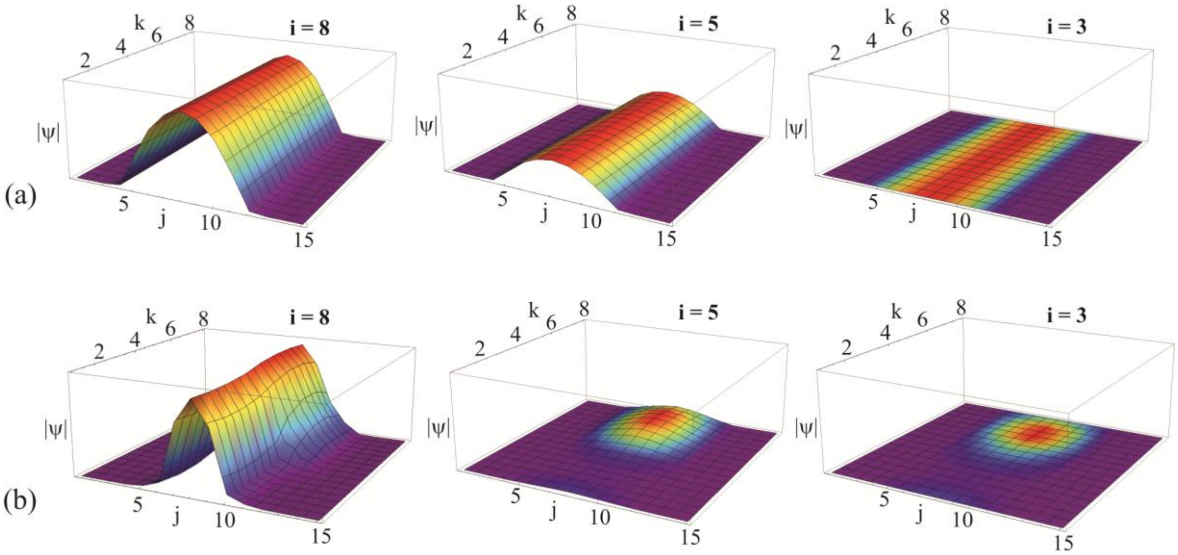

Fig. 3.3. Electron function modulus for ground state in Si nanowire with constant (a) and periodically modulated (b) cross-section, covered with a $SiO_2$ shell.

The distribution of wave function in *YZ* plane of NWs for three different values of coordinate *i*=8, 5 and 3 is shown. The *YZ* section for *i*=8 is situated in the middle of the wire's cross-section (since the total number of discrete *i* points is $N_x$=15), while for *i*=3 totally in the $SiO_2$ shell. For *i*=5 in case of unmodulated nanowire the *YZ* section totally lies on the Si/$SiO_2$ interface and in case of modulated nanowire one part of it is situated in $SiO_2$ shell (corresponds to the narrow Si segment; *k*=1,2,3,4) and another part on the Si/$SiO_2$ interface (corresponds to the wide Si segment; *k*=5,6,7,8).

From Figure 3.3(a) one can observe that for Si NW with constant cross-section the wave function distribution along the *Z* axis is homogeneous. In this case the wave function modulus strongly decreases in the $SiO_2$ shell e.g. for *i*=3 it is ~3 orders lower than for *i*=8. In case of a Si NW with modulated cross-section (Figure 3.3(b)) there is an inhomogeneity in the wave function distribution along the wire's axis, namely, in the wide segment is concentrated the main part of the wave function. In particular, for *i*=5 case it is clearly seen the electron wave function localization in the wide segment of the MNW. In addition, all graphics demonstrate that electron wave function is almost completely localized in the silicon channel and very weakly penetrates into the $SiO_2$ shell, which is caused by a high potential barrier on the Si/$SiO_2$ interface: $V_b$ = 3.2 eV.

## 3.2. Phonon processes in Si and Si/Ge core/shell modulated nanowires

In spite of the fact that bulk Si is a poor thermoelectric with room-temperature *ZT* ~ 0.01 [141], thin Si NWs and Si/Ge segmented NWs are considered promising for thermoelectric applications [54-55, 125, 142-143] owing to the much lower values of the RT (RT) lattice thermal conductivity $\kappa_{ph} < 1$ W m$^{-1}$ K$^{-1}$. It has been demonstrated experimentally that the good electrical conductivity, as in doped bulk Si, and poor thermal conductivity of Si NWs [55] and rough Si NWs [54] provide relatively high values of *ZT* ~ 0.3 to 0.6 at RT. These experimental results stimulate theoretical search of one-dimensional Si-based nanostructured materials with the ultra-low thermal conductivity. An up to 30-fold drop of the RT lattice thermal conductivity in comparison with Si NWs was reported for Si-based segmented nanowires consisting of acoustically-mismatched materials [125]. The reduction of the RT lattice thermal conductivity up to 75% was theoretically demonstrated in Si/Ge core/shell NWs with Ge thicknesses of several monoatomic layers [144]. The corresponding enhancement of *ZT* in these NWs was also predicted [145].

Fabrication of the periodically cross-section modulated nanowires is still a major challenge. It is difficult to precisely control shape and size of the nanowire segments. Nevertheless, the periodic diameter-modulated GeSi/Si pillar structures were prepared from the multilayer GeSi/Si islands using the selective etching of Si in KOH [136]. The theoretical models for the cross-section modulated nanowires have also been reported. Ballistic thermal conductance of Si and Si/Pb wires with modulation of the cross-sectional width from 0.1 to 0.5 μm was considered in Ref. [138]. Within the framework of the elasticity theory, thermal conductance was demonstrated to yield a minimum with a reduction by a factor 0.6 to 0.7 at *T* ~ 0.1 K to 0.3 K [138]. Nanowires of GaAs modulated by several quantum dots reveal the enhanced thermoelectric properties at low temperatures in the ballistic transport regime due to modification of the electron transmission coefficients [139-140] and reduction of the low-temperature thermal conductance [146].

Numerous theoretical investigations of phonon properties of semiconductor nanostructures were carried out in the framework of a continuum approach. This approach is a powerful tool for the analysis of the long-wavelength phonon modes. It is completely adequate for the description of the electron-phonon interaction [46, 147-148] or low-temperature thermal conductivity in nanostructures when only the low-frequency long-wavelength phonon modes are populated [146, 149]. However, the continuum approach significantly overestimates thermal conductivity for temperatures $T$>100 K in comparison with the FCC model of the lattice vibrations due to a steep slope of the dispersion curves for high-frequency phonon modes [33]. Different models of lattice dynamics and molecular dynamics simulations [88, 118, 150-154] allow for an accurate description of heat transfer and thermal conductivity in a good agreement with experiments.

The schematics of the considered Si NW, Si MNW and Si/Ge core/shell MNW are shown in Figure 3.4. The external surfaces of the nanostructures under consideration are assumed to be free [32, 116, 125]. The $X$ and $Y$ axes of the Cartesian coordinate system are located in the cross-sectional plane of the nanowires (unmodulated or modulated) and are parallel to its sides, while the $Z$ axis is directed along the wire axis. It is assumed that NW and MNWs are infinite along the $Z$ axis. The origin of the coordinates is set at the center of the nanowire cross-section. The translation period of MNW consists of two parts with dimensions $d_x^1 \times d_y^1 \times l_z^1$ and $d_x^2 \times d_y^2 \times l_z^2$, respectively. In case of a core/shell MNW the modulated Si core is covered by Ge shell with constant thickness $d_{Ge}$. The length of one MNW period is $l_z = l_z^1 + l_z^2$. The sides of unmodulated NW are denoted as $d_x$ and $d_y$.

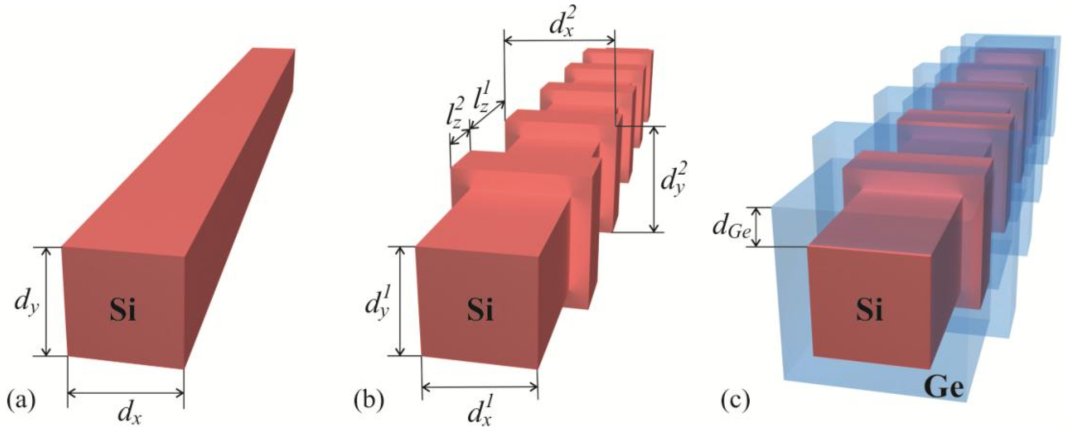

Fig. 3.4. Schematic view of a Si nanowire with constant cross-section (a), a cross-section modulated Si nanowire (b) and a cross-section modulated core/shell Si/Ge nanowire (c).

The crystal lattice of Si consists of two face-centered cubic sublattices, which are shifted along the main diagonal of a unit cell by 1/4 of its length. For convenience, let us identify the atoms of the first sublattice as the “blue” atoms while the atoms of the second sublattice as the “red” atoms (see Fig. 3.5 below).

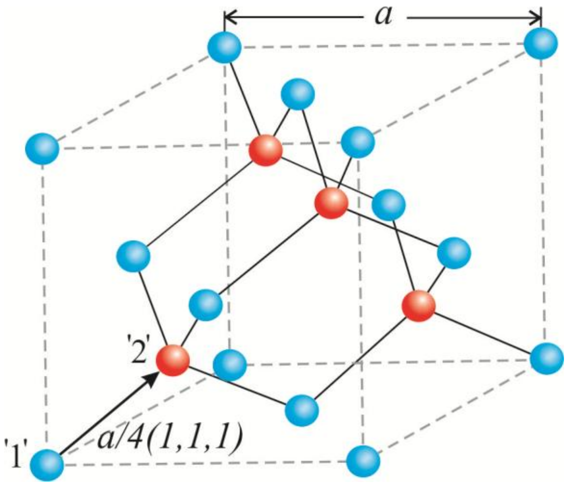

Fig. 3.5. Schematics of a diamond-type crystal lattice. Lattice constant is denoted as *a*.

In nanostructures under consideration, the displacements of the atoms belonging to one period only are independent. The rest of the atomic displacements are equivalent to those in the selected period due to the translational symmetry along the *Z*-axis. In the case of an unmodulated NW, the translation period consists of two atomic layers of the "blue" atoms and two atomic layers of the "red" atoms (all layers are perpendicular to the *Z* axis). For MNW, the number of atomic layers in the period is determined by $l_z$. The displacements of equivalent atoms have the form:

$$\vec{u}(x,y,z+nl_z;q_z)=\vec{w}(x,y,z;q_z)e^{iq_z(nl_z)}, \tag{3.5}$$

where $\vec{w}(x,y,z;q_z)\equiv\vec{w}(\vec{r};q_z)$ is the displacement of the atom with coordinates *x*, *y* and *z*, the period is labeled by an integer *n*, and $q_z$ is the phonon wavenumber. The equations of motion for the displacement are

$$\omega^2 w_i(\vec{r}_k;q_z)=\sum_{j=x,y,z;\vec{r}_k'} D_{ij}(\vec{r}_k,\vec{r}_k')w_j(\vec{r}_k';q_z),\ k=1,\ldots,N,\ i=x,y,z, \tag{3.6}$$

where

$$D_{ij}(\vec{r}_k,\vec{r}_k')=\Phi_{ij}(\vec{r}_k,\vec{r}_k')/\sqrt{m(\vec{r}_k)m(\vec{r}_k')}. \tag{3.7}$$

In Equations (3.6) and (3.7) $D_{ij}$ are the dynamic matrix coefficients, $m(\vec{r}_k)$ $[m(\vec{r}_k')]$ is the mass of the atom at $\vec{r}_k$ $[\vec{r}_k']$, $\Phi_{ij}(\vec{r}_k,\vec{r}_k')$ is the matrix of force constants and *N* is the number of atoms in the NW or MNW translational period. For the atom at $\vec{r}_k$, the summation in Equation (3.6) is performed over all the nearest and second-nearest atoms at $\vec{r}_k'$. In case of silicon or germanium, the atom at $\vec{r}_k$ has 4 nearest neighbors at $\vec{r}_{k,n}'=\vec{r}_k+\vec{h}_n^I$ (*n*=1,…,4) and 12 second-nearest neighbors at $\vec{r}_{k,n}'=\vec{r}_k+\vec{h}_n^{II}$ (*n*=1,..,12). The components of vectors $\vec{h}_n^I$ and $\vec{h}_n^{II}$ are presented in Table 3.1. In our model, the interaction of an atom with its nearest and second-nearest neighbors is described by the following force constant matrices: $\Phi^{I}_{ij} = (16/a^2)(\alpha\delta_{ij} + \beta(1-\delta_{ij}))h^{I}_{n,i}h^{I}_{n,j}$ for the nearest atoms ($n$=1,…,4) and $\Phi^{II}_{ij} = (4/a^2)(\lambda\delta_{ij}(a^2/4 - h^{II}_{n,i}h^{II}_{n,i}) + \mu\delta_{ij}h^{II}_{n,i}h^{II}_{n,i} + \nu(1-\delta_{ij})h^{II}_{n,i}h^{II}_{n,j})$ for the second-nearest atoms ($n$ = 1, …, 12), where $a$ is the lattice constant, $\alpha$, $\beta$, $\mu$, $\lambda$ and $\nu$ are the force constants, $\delta_{ij}$ is the Kronecker's delta and $i,j=x,y,z$. The force constant matrix $\Phi_{ij}(\vec{r}_k, \vec{r}\,'_k = \vec{r}_k)$ is obtained from the condition that the total force acting on the atom $\vec{r}_k$ at the equilibrium position is equal to 0, i.e. $\Phi_{ij}(\vec{r}_k, \vec{r}\,'_k = \vec{r}_k) + \sum_{\vec{r}\,'_k}\Phi_{ij}(\vec{r}_k, \vec{r}\,'_k \neq \vec{r}_k) = 0.$

By solving the equations of motion (3.6) at $\Gamma$ and $X$ BZ points of bulk Si, one can express three constants $\alpha$, $\mu$, and $\lambda$ through $\beta$ and the frequencies of the LO and TO phonons at $\Gamma$ point and the LA phonon at $X$ point:

$$\begin{aligned} &\alpha = m\omega^2_{LO}(\Gamma)/8;\ \ \mu = m\left(2\omega^2_{LA}(X) - \omega^2_{LO}(\Gamma)\right)/32; \\ &\lambda = m\left(4\omega^2_{TO}(X) - 2\omega^2_{LA}(X) - \omega^2_{LO}(\Gamma)\right)/32 - \beta/2. \end{aligned} \tag{3.8}$$

The constants $\beta$ and $\nu$ are treated as fitting parameters and are obtained from the best fit to experimental dispersion curves for bulk Si [115]. The numerical values of the force constants for Si are indicated in the last column of Table 3.1.

To calculate the energy spectra of phonons in Si NWs and MNWs, the set of Equations (3.6) was solved numerically by taking into account the periodic boundary conditions [see Equation (3.5)] along the $Z$-axis and free-surface boundary conditions in the $XY$-plane (i.e. all force constants outside the nanostructure are set to zero). The calculations were performed for all $q_z$ values in the interval (0, $\pi/l_z$) for MNWs and (0, $\pi/a$) for NWs (in the case of NWs, $l_z$ = $a$), where $a$ = 0.5431 nm is the lattice constant of Si. The notations and dimensions in the monoatomic layers (ML, 1 ML = $a$/4) for analyzed Si NWs and MNWs are represented in Table 3.1.

Table 3.1. Notations and dimensions for Si nanowires and Si cross-section modulated nanowires under consideration.

| Nanostructure | Dimensions | Notation |
|---|---|---|
| Si NW | 14 ML × 14 ML | NW #1 |
| Si MNW | 14 ML × 14 ML × 6 ML / 22 ML × 22 ML × 6 ML | MNW #1 |
| Si MNW | 14 ML × 14 ML × 8 ML / 18 ML × 18 ML × 8 ML | MNW #2 |
| Si MNW | 14 ML × 14 ML × 8 ML / 22 ML × 22 ML × 8 ML | MNW #3 |
| Si MNW | 14 ML × 14 ML × 8 ML / 26 ML × 26 ML × 8 ML | MNW #4 |

| | | |
|---|---|---|
| Si MNW | 14 ML × 14 ML × 8 ML / 30 ML × 30 ML × 8 ML | MNW #5 |
| Si MNW | 14 ML × 14 ML × 8 ML / 34 ML × 34 ML × 8 ML | MNW #6 |
| Si MNW | 14 ML × 14 ML × $N_z$ / 22 ML × 22 ML × $N_z$ | MNW #7 |
| Si MNW | 14 ML × 14 ML × 4 ML / 22 ML × 22 ML × 4 ML | MNW #8 |
| Si MNW | 14 ML × 14 ML × 12ML / 22 ML × 22 ML × 12 ML | MNW #9 |

The phonon energy spectra of Si NW #1 and Si MNW #1 are shown in Figure 3.6(a) and (b), correspondingly. In the figure, we show 20 lowest branches $\hbar\omega_s(q_z)$ ($s$=1,2,…,20) in both structures as well as several higher branches with $s$=20,25,30,35,…, 285,290,294 for the NW and with $s$=35,50,65,80,…,1515,1530 for the MNW.

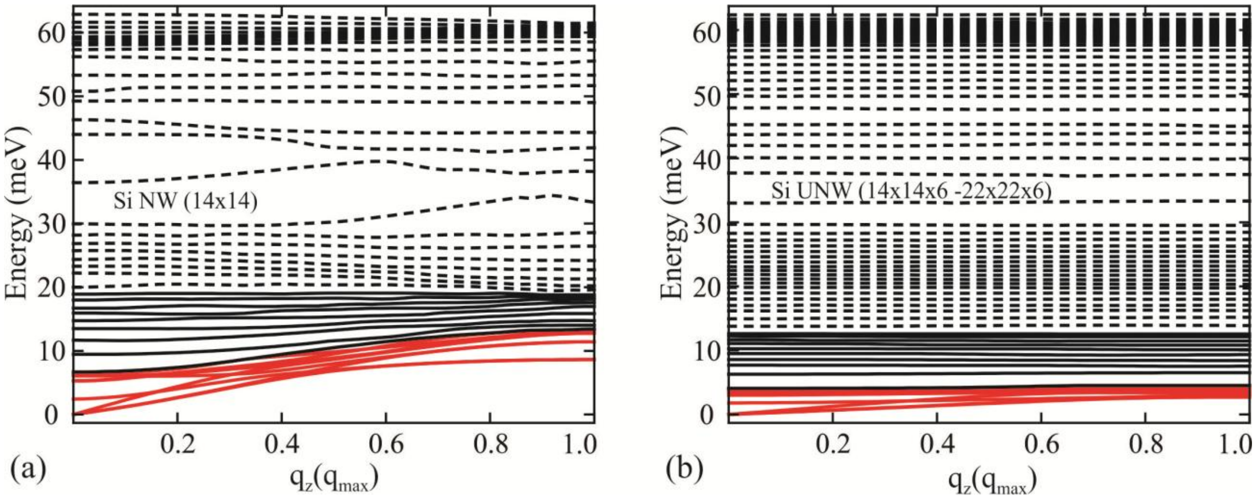

Fig. 3.6. Phonon energies as a function of the phonon wave vector $q$ (a) in Si NW with the lateral cross-section 14 ML × 14 ML (the phonon branches with $s$=1 to 20, 25, 30, 35…290, 294 are shown) and (b) in Si MNW with dimensions 14 ML × 14 ML × 6 ML/ 22 ML × 22 ML × 6 ML. The phonon branches with $s$=1 to 20, 35, 50, 65, …, 1515, 1530 are depicted.

The nanowire cross section is chosen the same as the cross section of narrow segments of the MNW (see Table 3.1). The volume of a translational period in the MNW is larger than that in the NW, therefore the number of quantized phonon branches in the MNW is substantially larger as compared to the NW. In the MNW, there are 1530 branches, while only 294 branches exist in the NW (see Figure 3.6). As follows from Figure 3.6, a great number of phonon modes in the MNW with energy $\hbar\omega > 5$ meV are dispersionless and possess group velocities close to zero due to the trapping into the MNW segments.

The trapping effect is illustrated in Figure 3.7: the average squared displacements of atoms (see Figure 3.7(a))

$$|U(z;s,q_z)|^2 = \begin{cases} \int\limits_{-d_x^1/2}^{d_x^1/2} \int\limits_{-d_y^1/2}^{d_y^1/2} |\vec{w}_s(x,y,z;q_z)|^2 \, dxdy, \text{ if } 0 \le z \le l_z^1 \\ \int\limits_{-d_x^2/2}^{d_x^2/2} \int\limits_{-d_y^2/2}^{d_y^2/2} |\vec{w}_s(x,y,z;q_z)|^2 \, dxdy, \text{ if } l_z^1 < z \le l_z^2 \end{cases} . \qquad (3.9)$$

in the mode ($s$=8, $q_z$=0.4$q_{z,\max}$) (red line) are relatively large in the wide segments of the MNW and almost vanishing in the narrow segments. Therefore this mode is trapped into the wide segments of the MNW. For comparison, it is also shown the average squared displacements of atoms in a propagating phonon mode ($s$=992, $q_z$=0.2$q_{z,\max}$) (blue line), which are equally large in both the wide and narrow MNW segments.

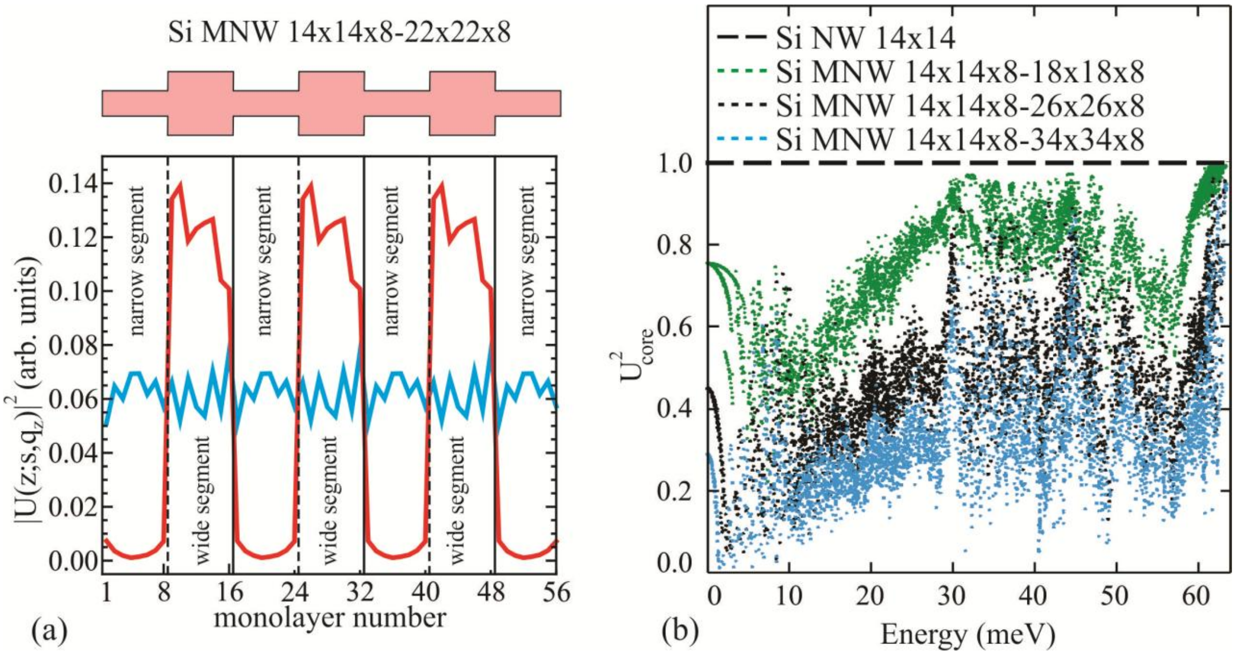

Fig. 3.7. (a) Average squared displacements $|U(z;s,q_z)|^2$ of the trapped ($s$=8, $q_z$=0.4$q_{z,\max}$) (red line) and propagating ($s$=992, $q_z$=0.2$q_{z,\max}$) (blue line) phonon modes in Si MNW with dimensions 14 ML × 14 ML × 8 ML/ 22 ML × 22 ML × 8 ML. (b) Localization of phonon modes in 14 ML × 14 ML MNW core shown for MNWs #2, #4 and #6.

For illustration of the phonon mode distribution in the cross-section of MNWs in Figure 3.7(b) we show the integral squared displacements of atoms in 14 ML × 14 ML cross-section channel as a function of the phonon energy:

$$U^2_{core} = \sum_{s(\omega)} \int\limits_{-d_x^1/2}^{d_x^1/2} \int\limits_{-d_y^1/2}^{d_y^1/2} \int\limits_{0}^{l_z^1+l_z^2} |\vec{w}_s(x,y,z;\omega)|^2 dxdydz \,/\, g(\omega). \qquad (3.10)$$

Here summation is performed over all phonon modes $s(\omega)$ with the frequency $\omega$; $g(\omega)$ is the number of the phonon modes. The results are presented for NW #1 (dashed black line) and

MNWs #2 (green points), #4 (black points) and #6 (blue points). In Si NW $U_{core}^2$ = 1 for all energies due to the orthonormalization of the phonon displacement vectors (see dashed black line in Figure 3.7(b)). Increase of the cross-section of the wide segments leads to the decrease of $U_{core}^2$ for all phonon energies and, corresponding, the rise of $(1-U_{core}^2)$. The latter is indicative of the phonon mode localization in the wide segments. Thus, the trapping effect enhances with increasing cross-section of the wide segments.

The effect of the phonon deceleration in cross-section modulated nanowires is illustrated in Figure 3.8, where is shown the average phonon group velocity $\langle v\rangle(\omega)=g(\omega)/\sum_{s(\omega)}(d\omega_s/dq_z)^{-1}$ as a function of the phonon energy for Si NW #1 (dashed line) and Si MNW #1 (solid line).

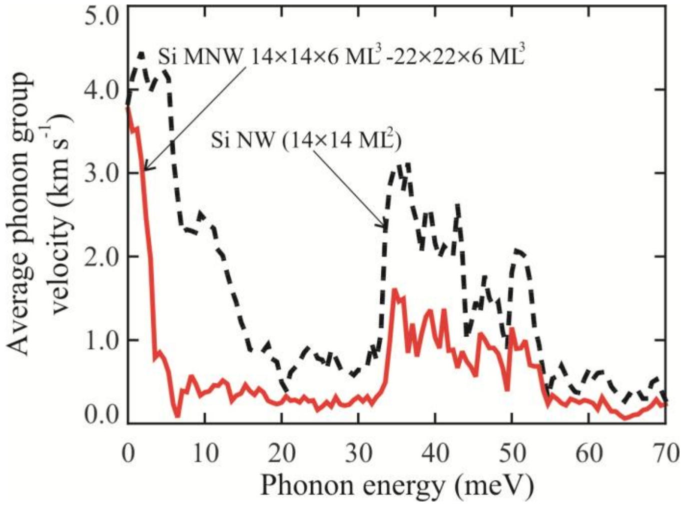

Fig. 3.8. Average phonon group velocity as a function of the phonon energy in Si NW with the lateral cross-section 14 ML × 14 ML and Si MNW with dimensions 14 ML × 14 ML × 6 ML/ 22 ML × 22 ML × 6 ML.

The average phonon group velocity in MNW is smaller than that in the NW for all phonon energies. As a result, the phonon modes in MNW carry less heat than those in the NW. The drop in the phonon group velocities in MNWs in comparison with NWs is explained by the trapping effect: the trapped phonon modes represent standing waves existing only in the wide segments of MNWs. These modes do not penetrate into narrow MNW segments (see the red line in Figure 3.7(a)). Therefore, these phonons possess group velocities close to zero. For example, group velocities of the phonon modes shown in Figure 3.7(a) are $\upsilon_{z,s=992}(q_z=0.2q_{z,\max})\sim$ 1.5 km/s and $\upsilon_{z,s=8}(q_z=0.4q_{z,\max})\sim$ 0.01 km/s for the propagating and trapped modes, respectively. A similar strong reduction of the phonon group velocity has been recently demonstrated in the segmented

NWs, consisting from the acoustically-mismatched materials [125]. The effect was also explicated by the phonon modes trapping in NW segments.

The following NWs were considered: Si/Ge core/shell MNWs with $14\times14\times N_z-22\times22\times N_z$ ML Si core and different $d_{Ge}$ (denoted as MNW # $N_z$ - $d_{Ge}$), Si MNWs with dimensions $14\times14\times N_z-22\times22\times N_z$ ML (denoted as MNW # $N_z$) and Si NW with the cross-section area $d_x\times d_y$ = $14\times14$ ML, which are equal to the cross-section area of a thin Si segment of MNWs (denoted as NW #1).

As well as in the case of Si NWs and Si MNWs the phonon energy spectra in Si/Ge core/shell MNWs were calculated from equation (3.2). In Figure 3.9, we show dependence of the phonon energies on $q_z$ for the Si NW #1 (panel (a)) and Si/Ge MNW#8-4 (panel (b)). The energy dispersion for phonon branches $s$=1-5,7,9,11,..,293 of the Si NW#1 and $s$=1-5,25,50,75,..,4150 of the MNW#8-4 are plotted for comparison. The number of phonon branches $N_b$=4152 in the MNW#8-4 is substantially larger than $N_b$=294 in the NW#1.

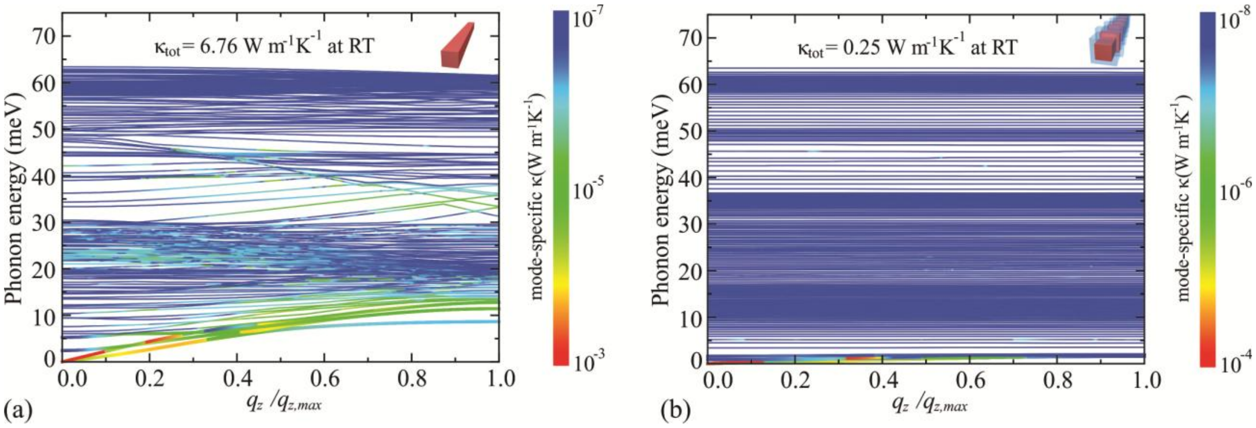

Fig. 3.9. Phonon energies as a function of the phonon wave vector $q_z$ in (a) a generic Si nanowire with the lateral cross-section area $14\times14$ ML and (b) a cross-section modulated Si/Ge nanowire with $14\times14\times8-22\times22\times8$ ML Si core and 4 ML – thicker Ge shell. The color in the plot shows the relative participation of the phonons in heat transfer: from maximum (red) to minimum (blue).

Flattening of the phonon dispersion branches in MNW leads to a decrease in the phonon group velocities in MNW in comparison with NW. As a result, the average phonon group velocities in Si/Ge MNWs are substantially lower than those in both Si NW and corresponding Si MNW. The color of the curves shows contribution of a given phonon mode ($s$,$q_z$) to thermal transport: red (blue) color designates maximum (minimum) participation. Since thermal conductivity is a sum of contributions of all phonon modes, we also calculated partial contribution of each mode. In Si NW, phonons with energy $\omega\leq10\,\mathrm{meV}$ carry 24% of heat while in the Si/Ge MNW#8-4 these modes carry 50% of heat. Therefore, participation of the higher energy phonons in heat transport is substantially reduced in Si/Ge MNWs.

The average phonon group velocity $\langle \upsilon \rangle (\omega) = g(\omega) / \sum\limits_{s(\omega)} (d\omega_s / dq_z)^{-1}$ is shown in Figure 3.10 for the Si NW#1, Si MNW#8 and Si/Ge MNWs #8-4 and #8-10. Here $g(\omega)$ is the number of the phonons with frequency $\omega$.

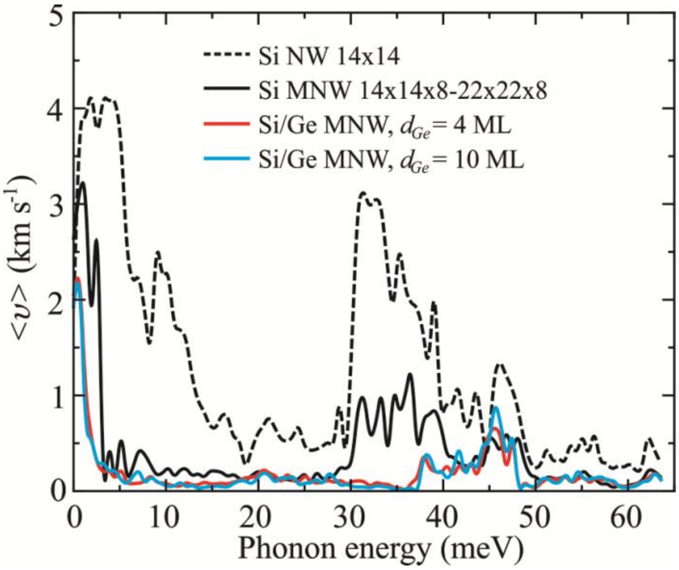

Fig. 3.10. Average phonon group velocity as a function of the phonon energy shown for Si NW with the lateral cross-section area $14 \times 14$ ML, Si MNW with dimensions $14 \times 14 \times 8 - 22 \times 22 \times 8$ ML and Si/Ge core-shell MNWs with $14 \times 14 \times 8 - 22 \times 22 \times 8$ ML Si core and different $d_{Ge}$

Note that Ge shell reinforces the decrease of $\langle \upsilon \rangle$ making it especially strong for the low- and middle-energy phonons with $\hbar\omega < 40\, meV$. Since these phonons are the main heat carriers in semiconductor nanostructures, the strong decrease of their group velocities significantly influences thermal conduction.

In calculations, we take into account all basic mechanisms of phonon scattering: three-phonon Umklapp scattering and boundary scattering [33, 115, 118, 120, 125, 151-154]. According to the Matthiessen's rule, the total phonon relaxation time is given by: $1/\tau_{tot,s}(q_z) = 1/\tau_{U,s}(q_z) + 1/\tau_{B,s}(q_z)$. Here, (i) $\tau_{U,s}$ is the relaxation time for the Umklapp scattering: $\frac{1}{\tau_{U,s}(q_z)} = B_s(q_z)\left(\omega_s(q_z)\right)^2 T \exp\left(-C_s(q_z)/T\right)$ [120]; (ii) $\tau_{B,s}$ is the relaxation time for the boundary scattering:

$$\frac{1}{\tau_{B,s}(q_z)} = \frac{1-p}{1+p} \frac{|\upsilon_{z,s}(q_z)|}{2} \left( \frac{1}{d_x} + \frac{1}{d_y} \right), \tag{3.11}$$

in the case of a NW,

$$\frac{1}{\tau_{B,s}(q_z)} = \frac{1-p}{1+p}\frac{|\upsilon_{z,s}(q_z)|}{2}\left(\left(\frac{1}{d_x^1}+\frac{1}{d_y^1}\right)\int_{-d_x^1/2}^{d_x^1/2}\int_{-d_y^1/2}^{d_y^1/2}\int_{0}^{l_z^1}\left|\vec{w}_s(x,y,z;q_z)\right|^2 dxdydz + \right. \qquad (3.12)$$
$$\left. +\left(\frac{1}{d_x^2}+\frac{1}{d_y^2}\right)\int_{-d_x^2/2}^{d_x^2/2}\int_{-d_y^2/2}^{d_y^2/2}\int_{l_z^1+a/4}^{l_z^1+l_z^2}\left|\vec{w}_s(x,y,z;q_z)\right|^2 dxdydz\right),$$

in the case of a MNW and

$$\frac{1}{\tau_{B,s}(q_z)} = \sum_{i=1}^{2}\frac{1}{\tau_{B,s}^i(q_z)},$$
$$\frac{1}{\tau_{B,s}^i(q_z)} = \begin{cases} \dfrac{1-p}{1+p}\dfrac{|\upsilon_{z,s}(q_z)|}{2}\left\{\xi_{core,s}^i(q_z)\left(\dfrac{1}{d_x^i}+\dfrac{1}{d_y^i}\right)+\right. \\ \left. +\xi_{shell,s}^i(q_z)\left(\dfrac{1}{d_x^i+d_{Ge}}+\dfrac{1}{d_y^i+d_{Ge}}\right)\right\}, \text{ if } \xi_{core,s}^i(q_z)/\xi_{shell,s}^i(q_z) \ge \delta, \\ \dfrac{1-p}{1+p}|\upsilon_{z,s}(q_z)|\dfrac{\xi_{shell,s}^i(q_z)}{d_{Ge}}, \xi_{core,s}^i(q_z)/\xi_{shell,s}^i(q_z) < \delta, \end{cases} \qquad (3.13)$$

in the case of a core/shell MNW, where

$$\xi_{core,s}^i(q_z) = \int_{-d_x^i/2}^{d_x^i/2}\int_{-d_y^i/2}^{d_y^i/2}\int_{(i-1)l_z^1}^{l_z^1+(i-1)l_z^2}\left|\vec{w}_s(x,y,z;q_z)\right|^2 dxdydz,$$
$$\xi_{shell,s}^i(q_z) = \int_{-(d_x^i+d_{Ge})/2}^{(d_x^i+d_{Ge})/2}\int_{-(d_y^i+d_{Ge})/2}^{(d_y^i+d_{Ge})/2}\int_{(i-1)l_z^1}^{l_z^1+(i-1)l_z^2}\left|\vec{w}_s(x,y,z;q_z)\right|^2 dxdydz - \xi_{core,s}^i(q_z). \qquad (3.14)$$

In equations (3.11-3.13), $\upsilon_{z,s}(q_z) = d\omega_s(q_z)/dq_z$ is the phonon group velocity along the nanowire axis, *p* is the specularity parameter of the boundary scattering. Equations (3.11-3.13) provide an extension of the standard formula for the rough edge scattering [115] to the case of a rectangular NW or MNW. In equation (3.12) it was taken into account that a part of the phonon wave corresponding to the mode (*s*,*q*$_z$), concentrated in the MNW segment $d_x^1 \times d_y^1 \times l_z^1$, scatters on the boundaries of this segment, while the rest of this wave scatters on the boundaries of the segment $d_x^2 \times d_y^2 \times l_z^2$. In equation (3.13) the parameter $\delta$ was introduced in order to classify different phonon modes: core-like, cladding-like and propagating. The quantities $\xi_{core,s}^i(q_z)$ and $\xi_{shell,s}^i(q_z)$ show the relative portion of the phonon mode (*s*,*q*$_z$), concentrated in the core or shell of the *i*th MNW segment, correspondingly. For Si/Ge core/shell MNWs it was taken into account that the core-like and propagating modes partially scatter at Si/Ge interfaces and outer boundaries while cladding-like (Ge-like) modes with $\xi_{core,s}^i(q_z)/\xi_{shell,s}^i(q_z) < \delta$ scatter only at

Si/Ge interfaces. In this sense, the parameter $\delta$ represents a threshold value for a ratio between the integrated phonon amplitudes concentrated in the core $\xi^{i}_{core,s}(q_z)$ and in the shell $\xi^{i}_{shell,s}(q_z)$ of *i*th MNW segment. In calculations it was used $\delta = 0.1$, which means that in the cladding-like modes more than 90% of lattice vibrations from the *i*th MNW segment occur in Ge-shell, while Si core-region is depleted of phonons. A similar effect of the phonon depletion was theoretically described by Pokatilov et.al. in Ref. [155] for the acoustically-mismatched planar heterostructures, where part of the phonons is pushed out into the acoustically softer layers.

The mode-dependent parameters $B_s$ and $C_s$ in the expressions for the Umklapp scattering in Si/Ge MNWs were averaged for the values of the Umklapp scattering parameters in bulk Si and Ge so that $B_s(q_z) = (\xi^{1}_{core,s}(q_z) + \xi^{2}_{core,s}(q_z))B_{Si} + (\xi^{1}_{shell,s}(q_z) + \xi^{2}_{shell,s}(q_z))B_{Ge}$ and $C_s(q_z) = (\xi^{1}_{core,s}(q_z) + \xi^{2}_{core,s}(q_z))C_{Si} + (\xi^{1}_{shell,s}(q_z) + \xi^{2}_{shell,s}(q_z))C_{Ge}$. In the case of Si NW and Si MNW, we have $\xi^{1}_{shell,s}(q_z) + \xi^{2}_{shell,s}(q_z)$ = 0 and $B_s(q_z)=B_{Si}$, $C_s(q_z)=C_{Si}$. The bulk values $B_{Si}$ and $C_{Si}$ were taken from Ref. [37] while $B_{Ge}$ and $C_{Ge}$ were determined by comparing the calculated thermal conductivity of bulk Ge with experimental data [121]: $B_{Si} = 1.88\times10^{-19}$ s/K, $C_{Si}$ = 137.39 K, $B_{Ge} = 3.53\times10^{-19}$ s/K, $C_{Ge}$ = 57.6 K.

The Boltzmann transport equation in the relaxation time approximation [37, 118, 125] was used in order to model the thermal properties of Si-based modulated nanowires. See equations (2.6)-(2.9) for description of this approach. Within BTE with relaxation time approximation the phonon flux per unit gradient in the Si NWs and the Si MNWs is given by:

$$\Theta = \frac{1}{2\pi k_B T^2} \sum_{s=1,\ldots,3N} \int_{0}^{q_{z,\max}} \left(\hbar\omega_s(q_z)\upsilon_{z,s}(q_z)\right)^2 \tau_{tot,s}(q_z) \frac{\exp\left(\dfrac{\hbar\omega_s(q_z)}{k_B T}\right)}{\left(\exp\left(\dfrac{\hbar\omega_s(q_z)}{k_B T}\right)-1\right)^2} dq_z . \tag{3.15}$$

Here $\tau_{tot,s}$ is the total phonon relaxation time, *s* is the number of a phonon branch, $k_B$ is the Boltzmann constant, $\hbar$ is the Planck constant and *T* is the absolute temperature. The Eq. (3.15) was derived from Eqs. (2.8-2.9) taking into account one-dimensional density of phonon states [125].

In Figure 3.11, the lattice thermal conductivity $\kappa^{NW}_{ph} = \Theta/(d_x d_y)$ and $\kappa^{MNW}_{ph} = \Theta(l^1_z + l^2_z)/(d^1_x d^1_y l^1_z + d^2_x d^2_y l^2_z)$ are plotted as a function of temperature for Si NW #1, as well as for Si MNWs #2, #3, #4 and #5 (see Table 3.1 for denotations). The results are presented for a reasonable specularity parameter *p* = 0.85, which was found in Ref. [118] from a comparison between theoretical and experimental data for a Si film of 20 nm thickness.

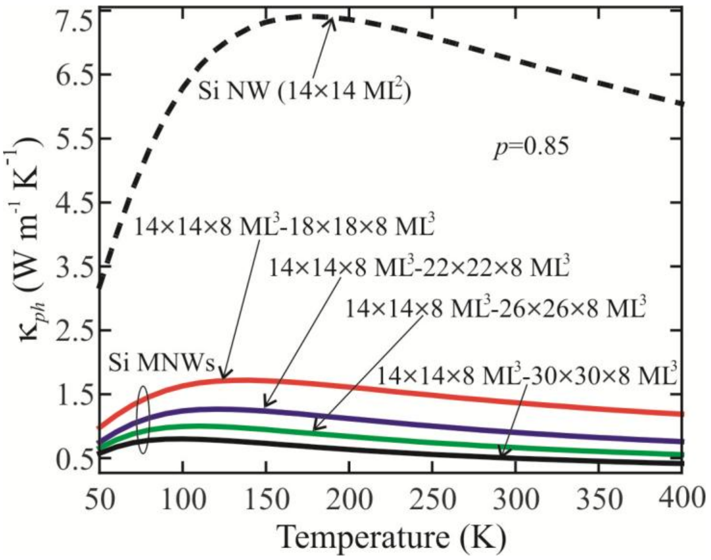

Fig. 3.11. Temperature dependence of the lattice thermal conductivity in Si NW with the cross-section 14 ML × 14 ML and Si MNW with different dimensions.

A significant redistribution of the phonon energy spectra and a reduction of the average group velocities in MNWs strongly decrease their lattice thermal conductivity in comparison with the NW. At RT, the ratio between the thermal conductivities in NW and MNWs ranges from a factor of 5 to 13 depending on $S_2 = d_x \times d_y$. However, this result does not mean that the ratio of the thermal fluxes in NW and MNWs should be the same since the average cross section of MNWs is larger than that in NW. To compare the abilities of MNWs and NWs to conduct heat, it was calculated the thermal flux per unit temperature gradient Θ using equation (3.15) for all structures under analysis.

In Figure 3.12(a) we show the thermal flux for Si NW #1 (upper dashed line) and Si MNWs #2, #4 and #6 for $p$ = 0.85 as a function of temperature.

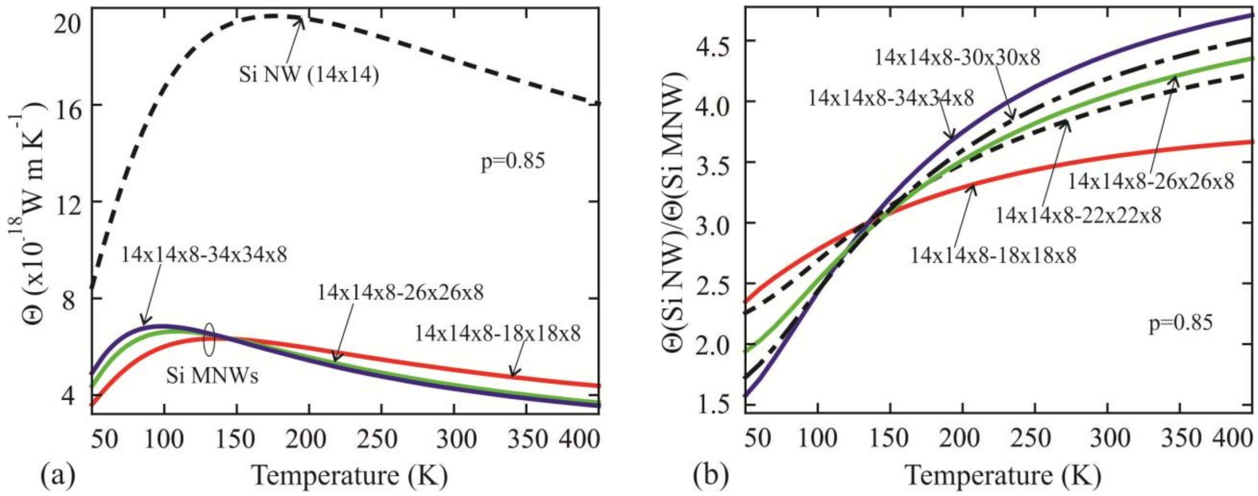

Fig. 3.12. (a) Temperature dependence of the thermal flux for Si NW (dashed line) and Si MNWs with dimensions 14 ML × 14 ML × 8 ML/ 18 ML × 18 ML × 8 ML, 14 ML × 14 ML × 8 ML/ 26 ML × 26 ML × 8 ML and 14 ML × 14 ML × 8 ML/ 34 ML × 34 ML × 8 ML. (b) Temperature dependence of the ratio between thermal fluxes in Si NW and Si MNWs.

The maxima on the thermal flux curves are determined by the interplay between the three-phonon Umklapp and the phonon-boundary scattering. At low temperatures, the boundary scattering dominates; the thermal flux increases with temperature due to the population of high-energy phonon modes and approaches the maximum value when $\tau_U \sim \tau_B$. A subsequent rise of temperature leads to an enhancement of the Umklapp scattering and diminution of the thermal flux. An increase of the cross-section of the MNW wide segments attenuates the phonon-boundary scattering, and the maximum of the thermal flux curves shifts to lower temperatures: from $T$ = 190 K for Si NW #1 to $T$ = 100 K for Si MNW #6. Therefore, at low temperatures ($T$<120 K) the thermal flux reduction is stronger in MNWs with the smaller cross-sections. Numerous high energy phonon modes in MNWs are trapped in the wide segments and possess a low group velocity. The population of these modes with increasing temperature almost does not increase the thermal flux. Thus, at medium and high temperatures the Umklapp-limited thermal flux in MNWs reduces stronger than that in the generic NW. The ratio of the thermal fluxes in NW and MNW $\eta = \Theta(\text{Si NW})/\Theta(\text{Si MNW})$ increases with temperature, and reaches the values of 3.5 to 4.5 depending on the MNW cross-section (see Figure 3.12(b)). For these temperatures, the increase of the MNW cross-section makes the reduction of the thermal flux stronger due to the corresponding rise of the number of the trapped high-energy phonon modes, which do not carry heat in MNWs. This is distinct from the case of NWs. The strong modification of the phonon energy spectra and phonon group velocities in MNWs in comparison with NWs also increases the Umklapp phonon scattering in MNWs as compared with NWs. The latter is an additional reason for the thermal flux reduction in MNWs.

An important quantity, which determines the thermal conductivity and thermal flux, is the mode-dependent phonon mean free path (MFP) $\Lambda_s(q_z)$ [122]. In our model $\Lambda_s(q_z)$ is given by:

$$1/\Lambda_s(q_z) = \sum_{r=B,U} 1/\Lambda_{r,s}(q_z), \tag{3.16}$$

where $\Lambda_{r,s}(q_z) = \tau_{r,s}(q_z)\cdot \upsilon_{z,s}(q_z)$ and $r$ = $B$ or $U$. The dependence of the average phonon MFP $\langle\Lambda\rangle(\omega) = g(\omega)/\sum_{s(\omega)}(1/\Lambda_s)$ on the phonon energy is presented in Figure 3.13 for the NW #1 (solid black line) and MNWs #7 with $N_z$ = 4 (solid red line) ML and $N_z$ = 12 (dashed blue line).

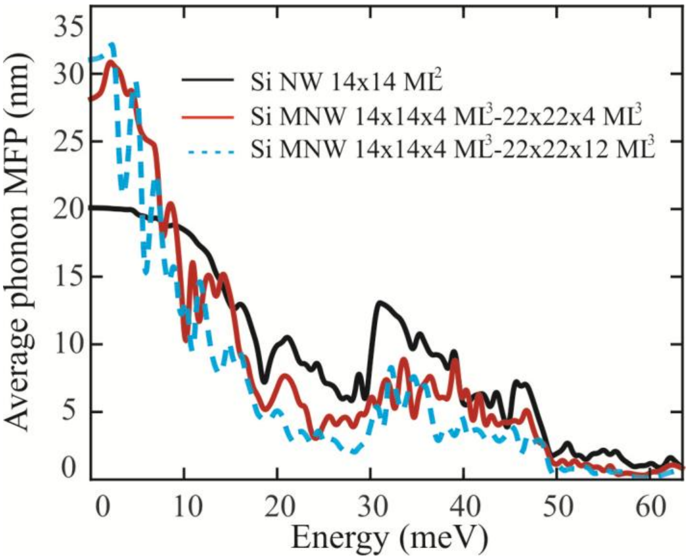

Fig. 3.13. Dependence of the average phonon mean free path on the phonon energy in Si NW #1 (solid black) and Si MNWs #8 (solid red line) and #9 (dashed blue line).

The interplay between $\Lambda_{B,s}(q_z)$ and $\Lambda_{U,s}(q_z)$ is insightful. The Umklapp-limited phonon MFPs $\Lambda_{U,s}(q_z)$ in MNWs are significantly smaller than those in NWs due to both reduction of the group velocity and enhancement of the phonon scattering. The boundary-limited MFPs $\Lambda_{B,s}(q_z)$ are larger in MNWs due to the larger average cross-section of MNW in comparison with that in NW (see equations (3.12-3.13)). As a result, at small energies when the Umklapp scattering is weaker than the boundary scattering $\langle\Lambda\rangle^{MNW} > \langle\Lambda\rangle^{NW}$, while for $\hbar\omega$>5 meV $\langle\Lambda\rangle^{MNW} << \langle\Lambda\rangle^{NW}$. Nevertheless, the integrand in equation (3.15) averaged over all phonon branches is smaller in MNWs for all energies due to the multiplication of $\Lambda_s(q_z)$ by $\upsilon_{z,s}(q_z)$. The augmentation of $l_z^2$ decreases $\langle\Lambda\rangle^{MNW}$ for almost all energies. The energy-averaged phonon MFP calculated from Figure 3.13 constitutes ~ 9.25 nm for the Si NW, ~ 8.4 nm for the MNW # 8 and ~ 6.9 nm for the MNW #9. The increase in the average MNW cross-section at fixed $l_z^1$ and $l_z^2$ attenuates boundary scattering and increases the thermal flux.

In Figure 3.14 we show the dependence of the ratio $\eta$ of the thermal fluxes in Si NW #1 and Si MNW #3 on temperature for different values of the specularity parameter $p$ = 0.0, 0,3, 0.6, and 0.9.

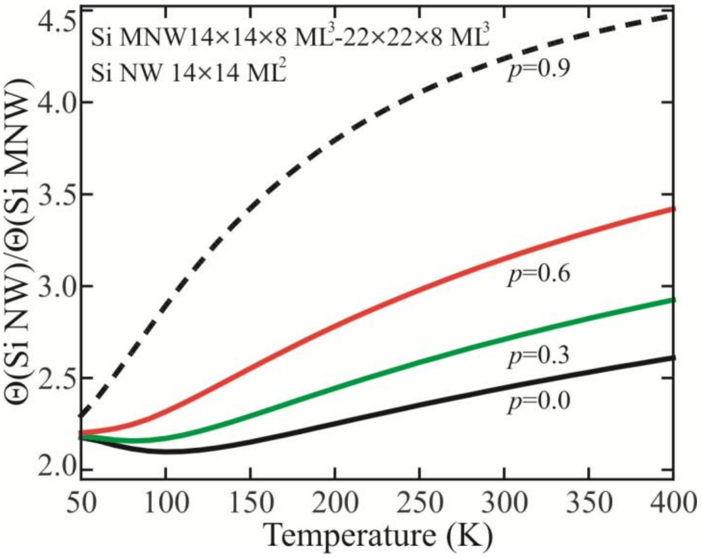

Fig. 3.14. Temperature dependence of the ratio of thermal fluxes in Si NW and Si MNWs. The results are shown for different values of the specularity parameter $p$ = 0.0, 0.3, 0.6 and 0.9.

For the interpretation of the data in Figure 3.14, it were calculated separately the thermal flux $\theta_B$ carried out by the long-wavelength phonon modes ($s$,$q_z$), which are mainly scattered at the boundaries and described by the inequality $\tau_U(s,q_z) \geq \tau_B(s,q_z)$, and the thermal flux $\theta_U$ carried out by the rest of the phonons, the total thermal flux being $\Theta = \Theta_B + \Theta_U$. The results show that for all values of $p$ under consideration, the RT flux $\Theta_B$ is by a factor of ~ 5 lower in MNW than that in NW due to the phonon trapping. An increase of $p$ decreases $\Theta_B$ and strongly enhances $\Theta_U$ in NW due to attenuation of the boundary scattering of the high-energy phonon modes. These modes in MNW do not participate in the heat transfer because of their localization in the wide segments. For this reason, the ratio between thermal fluxes in the NW and the MNW appreciably depends on $p$: for $p$ = 0.0 $\Theta_U(\text{NW})/\Theta_U(\text{MNW}) \sim$ 1, while for $p$ = 0.9 $\Theta_U(\text{NW})/\Theta_U(\text{MNW}) \sim 3.$ As a result, the flux ratio increases with increasing $p$ in a wide range of temperatures from 100 K to 400 K. The RT thermal conductivity of the rough Si NWs [54] is already by a factor of 100 lower than the corresponding bulk value. The obtained results suggest that the cross-section modulation of the rough NWs allows for an additional decrease of the thermal conductivity by a factor of 2 to 2.5 with a subsequent increase of $ZT$.

The dependence of the ratio $\eta$ of the thermal fluxes in Si NW #1 and Si MNW #7 on $N_z$ for the temperatures $T$ = 100 K, $T$ = 200 K, $T$ = 300 K and $T$ = 400 K and $p$ = 0.85 is presented in Figure 3.15. The calculated points for $N_z$ = 2,4,6,…,18 are joined by the smooth curves as guides for an eye.

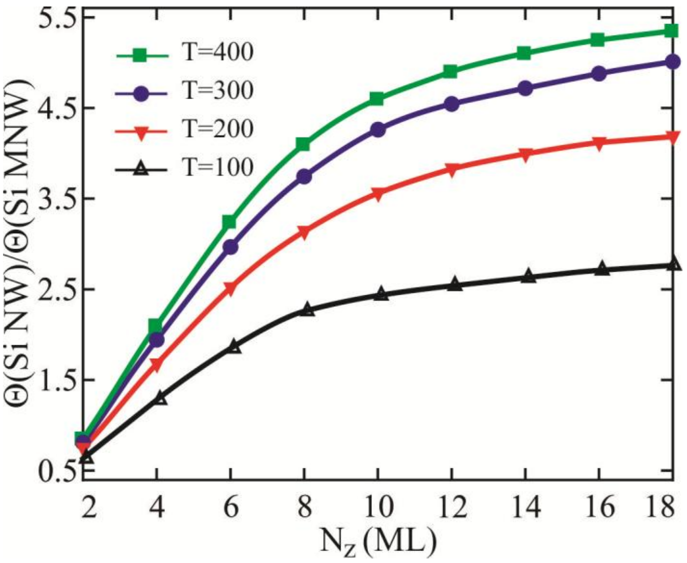

Fig. 3.15. Ratio of thermal fluxes in Si NW and Si MNWs as a function of $N_z$. The results are shown for different temperatures $T$ = 100 K, 200 K, 300 K and 400 K.

The overall trend of these curves is determined by the interplay of two effects: (i) the phonon modes trapping, which suppresses the heat flux and (ii) augmentation of the MNW average cross-section, which enhances the heat flux due to the emergence of additional phonon modes for heat propagation and attenuation of the phonon-boundary scattering. In Si MNW with the ultra-narrow segments $N_z$ = 2 ML, the trapping of phonon modes is weak and the thermal flux is larger than that in Si NW ($\eta$ <1) due to the weakening of the phonon-boundary scattering in MNW in comparison with NWs. The rise of $N_z$ enhances the trapping, and for all temperatures under consideration the flux ratios rapidly increase with $N_z$ rising up to the values 8 ML to 12 ML, and reach their maximum values at around $N_z$ = 16 ML to 18 ML. It is expected that a subsequent rise of $N_z$ should decrease $\eta$ due to augmentation of the MNW average cross-section.

The following NWs were considered: Si/Ge core/shell MNWs with $14\times 14\times N_z - 22\times 22\times N_z$ ML Si core and different $d_{Ge}$ (denoted as MNW # $N_z$ - $d_{Ge}$), Si MNWs with dimensions $14\times 14\times N_z - 22\times 22\times N_z$ ML (denoted as MNW # $N_z$) and Si NW with the cross-section area $d_x \times d_y$ = 14×14 ML, which are equal to the cross-section area of a thin Si segment of MNWs (denoted as NW #1).

The dependence of thermal conductivity on temperature, $T$, for Si NW#1, Si MNW#8, Si/Ge MNWs #8-1, #8-3, #8-7 and #8-10 is presented in Figure 3.16.

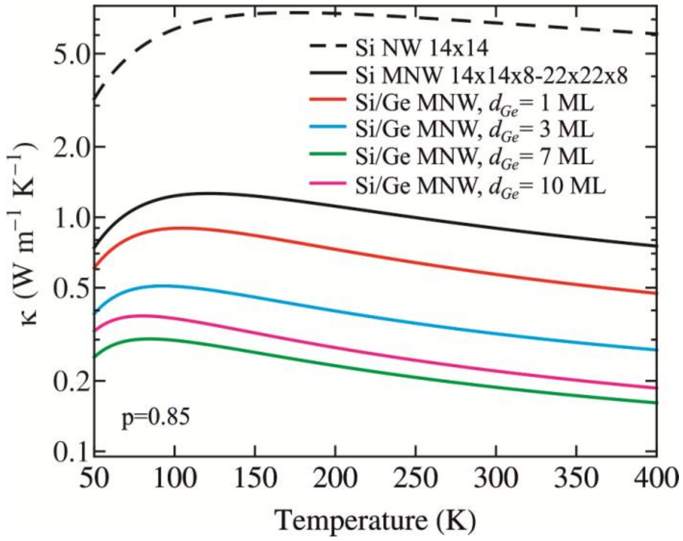

Fig. 3.16. Phonon thermal conductivity as a function of the absolute temperature. Results are presented for Si NW#1, Si MNW#8 and Si/Ge MNW#8- $d_{Ge}$ with different $d_{Ge}$.

The thermal conductivity of Si MNW#8 is lower by a factor of 4.3 – 8.1 than that in Si NW#1, depending on $T$. Additional strong decrease of κ is reached in Si/Ge MNWs. Increasing the thickness of Ge shell to $d_{Ge}$ = 7 ML leads to κ decrease by a factor of 2.9 – 4.8 in comparison with that in Si MNW#8, and by a factor of 13 – 38 in comparison with that in Si NW#1. The reduction in κ of Si/Ge MNWs is substantially stronger than that reported for core/shell nanowires without cross-sectional modulation [118, 144, 156-159]. In the generic core/shell nanowires, the κ decrease is due to phonon hybridization, which results in changes in the phonon DOS and group velocity. In the considered core/shell MNWs, κ reduction is reinforced due to localization of some phonon modes in wider MNW segments. The localization completely removes such phonons from the heat transport.

A comparison of κ of nanowires with the same cross-sections is sufficient to make a conclusion about their abilities to conduct heat. A lower κ means lower heat transfer. In the case of nanowires with various cross-sections, a nanowire with the minimum κ may not necessarily possess the minimum thermal transfer properties due to the difference in the cross-section areas. Therefore, in this case, a comparison of TF is more illustrative. The dependence of the ratio of TF at RT for MNWs and Si NW on $d_{Ge}$ is presented in Figure 3.17 for $N_z$ = 4, 6, 8, 12. Two points for $N_z$ = 20 and 28 at $d_{Ge}$ = 4 ML are also shown. All curves demonstrate a maximum between $d_{Ge}$ = 3 ML and $d_{Ge}$ = 6 ML. The increase in $N_z$ leads to a shift of the maximum to lower values of $d_{Ge}$.

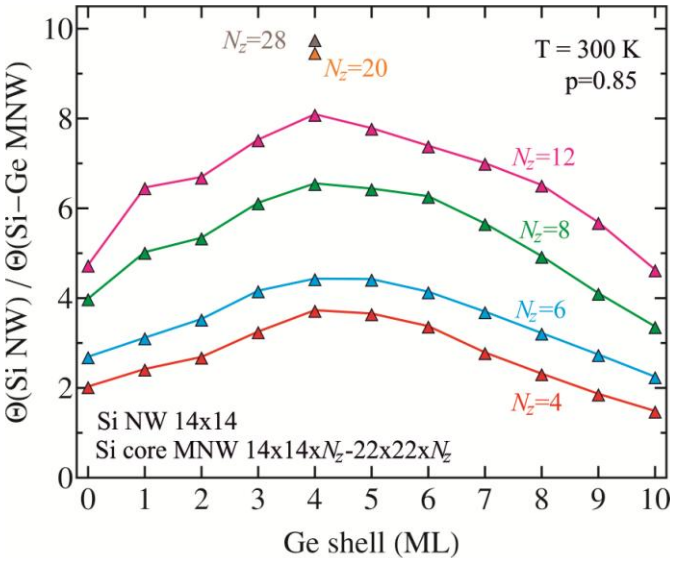

Fig. 3.17. Ratio of thermal fluxes in Si NW and Si/Ge MNWs as a function of $d_{Ge}$ for different values of $N_z$.

In order to explain the non-monotonic behavior of the ratio curves in Figure 3.17 it was calculated the spectral density of TF $\phi(\omega)$, determined by the equation $\Theta = \int_0^{\omega_{\max}} \phi(\omega) d\omega$, as a function of the phonon energy for Si NW, Si MNW and Si/Ge MNWs. The results show that in Si MNWs without Ge cladding, TF is strongly suppressed in comparison with Si NW due to redistribution of phonon energy spectra leading to the reduction of the phonon group velocities and localization of phonon modes in nanowire segments. The influence of Ge shell on the spectral density of MNWs is two-fold: (i) it reinforces the decrease in the spectral density in Si/Ge MNWs as compared with Si MNWs owing to a stronger decrease of the phonon velocities and stronger phonon localizations; (ii) it increases TF due to appearance of additional channels for heat transfer through the Ge shell and attenuation of the phonon boundary scattering of propagating and cladding-like phonons. An interplay of these two opposite effects explains the non-monotonic dependence of the TF ratio on $d_{Ge}$ shown in Figure 3.17. The difference between TF in MNWs and NWs becomes larger with growing $N_z$ and it reaches the maximum values of 10-11 at $N_z$ ~ 28 ML – 32 ML. For $N_z$>32 ML, TF ratio starts to decrease due to redistribution of the phonon energy spectra and heat conduction through Ge shell.

The energy-dependent localization of the phonon modes in the narrow segments of MNWs $\xi_{narrow} = (\xi^1_{core} + \xi^1_{shell}) \times 100\%$ is shown in Figure 3.18 for Si NW (dashed line), Si/Ge MNW#8-2 (red triangles) and MNW#8-7 (blue circles).

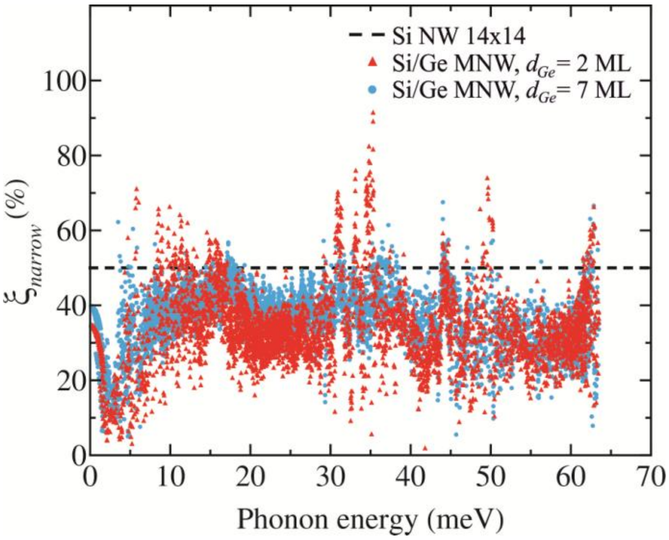

Fig. 3.18. Phonon modes localization as a function of the phonon energy in narrow segment of MNW. The results are presented for Si NW#1 (dashed line), Si/Ge MNW#8-2 (red triangles) and Si/Ge MNW#8-7 (blue circles).

Approximately, half of the phonon modes are concentrated in the wide segments of MNW and have $\xi_{narrow}$<30%, i.e. less than 30% of the atomic vibrations of these modes take place in the narrow segments of MNW. Many low-energy phonons in MNWs with $\hbar\omega \leq 15\,\mathrm{meV}$ are concentrated in Ge shell and possess $\xi_{Si} = (\xi^1_{core} + \xi^2_{core}) \times 100\% \leq 20\%$ (not shown in the Figure 3.18). It means that more than 80% of atomic vibrations in these modes occur in Ge shell. The number of the modes localized in Ge-shell increases with increasing shell thickness. The demonstrated localization of certain phonons in Ge shell or wide segments of MNWs is one of the reasons for the strong inhibition of κ in Si/Ge MNWs.

For ideally smooth interfaces when all phonon scattering events are specular $p$ =1. In the present calculations was used $p$=0.85, which corresponds to smooth NW surfaces with small average roughness height $\Delta \sim 1\mathrm{ML}$. The estimated $\Delta$ from averaging the mode-dependent specular parameter $\tilde{p}(q,\Delta) = \exp(-2q^2\Delta^2)$ [36, 115, 124, 160] over all $q$ is: $p$ = $\int_0^{q_{z,\max}} \tilde{p}(q)dq / q_{z,\max}$. The small roughness of NWs and MNWs interfaces is beneficial for both maintaining high electron mobility [161-162] and for suppression of the phonon heat conduction in MNWs [37]. It was already demonstrated (see section 3.2.5 and Ref. [37]) that increase of $p$ leads to faster growth of the thermal flux in Si NW than in Si MNWs without claddings. This effect is attributed to the fact that the higher energy phonons in MNW are excluded from thermal transport while they participate in the heat transfer in NWs. As a result the ratio between TF in Si NW and Si MNWs increases with increasing $p$.

### 3.3. Electron-phonon interaction in Si-based modulated nanowires

Here the electron-phonon interaction in Si-based modulated nanowires is treated in the deformation potential approach [163]. The deformation potential is given by relation [163-164]:

$$W_d = c_d \vec{\nabla} \vec{u}(\vec{r}), \tag{3.17}$$

where $c_d$ – deformation interaction constant and $\vec{u}$ – atomic displacement.

In a modulated nanowire electrons and phonons can propagate only along the wire axis *Z*, therefore their wavevectors have only one non-zero component i.e. $\vec{k} = (0,0,k_z)$ and $\vec{q} = (0,0,q_z)$. The atomic dispacement in a modulated nanowire in a second quantization formalism is determined by the equation:

$$\vec{u}(x,y,z) = \sum_{q_z}\sum_{s}\sum_{j=1}^{N}\sqrt{\frac{\hbar}{2L_z\bar{\rho}(s,q_z)\omega(s,q_z)}}\vec{e}(s,q_z,x,y,z)\left(b(s,q_z)+b^{+}(s,-q_z)\right)\exp\left(iq_z j\right), \tag{3.18}$$

where $\vec{e}(s,q_z,x,y,z)$ – polarization vector of $(s,q_z)$ phonon mode at $\vec{r} = (x,y,z)$, $b$ and $b^{+}$ – phonon annihilation and creation operators, respectively. Index $j$ numerates translational elements of modulated nanowire. The total length of nanowire is $L_z = N \times L_z^0$, where *N* – number of translation elements along the wire axis and $L_z^0$ – length of one translational element i.e. modulation period. The $\bar{\rho}(s,q_z)$ in equation (3.18) is the density of the material averaged over one modulation period:

$$\bar{\rho}(s,q_z) = \iiint \vec{e}(s,q_z,x,y,z)\rho(x,y,z)\vec{e}^{\,*}(s,q_z,x,y,z)dxdydz\,. \tag{3.19}$$

Electron-phonon coupling Hamiltonian [163-164]:

$$H_{e-ph} = \int \Psi^{+}(\vec{r})W_d(\vec{r})\Psi(\vec{r})d^3r\,, \tag{3.20}$$

where electron wavefunctions are given by the operator: $\hat{\Psi}(x,y,z) = \sum_{n,k_z} a_n(k_z)\psi(j,n,k_z,x,y,z)$, with $a$ and $a^{+}$ – electron annihilation and creation operators, respectively.

Taking into account equations (3.17) and (3.18) the electron-phonon interaction Hamiltonian takes the form:

$$\begin{gathered} H_{e-ph} = \sum_{k_z,q_z,s,n,n'}\sum_{s}\sqrt{\frac{\hbar}{2L_z\bar{\rho}(s,q_z)\omega(s,q_z)}}I(n,k_z,n',k_z',s,q_z)\times \\ \times\left(a_n(k_z)a_{n'}^{+}(k_z')b_s(q_z) - a_n(k_z)a_{n'}^{+}(k_z')b_s^{+}(q_z)\right)\left(\frac{1}{N}\sum_{j=1}^{N}\exp\left(\mathbf{i}(k_z \pm q_z - k_z')jL_z^0\right)\right) \end{gathered}, \tag{3.21}$$

where $I(n,k_z,n',k_z',s,q_z)$ – overlap integral of the electron-phonon interaction:

$$I(n,k_z,n',k_z',s,q_z)=\iiint\varphi(n,k_z,x,y,z)\Phi(s,q_z,x,y,z)\varphi^*(n',k_z',x,y,z)dxdydz\,, \tag{3.22}$$

with $\varphi(n,k_z,x,y,z)$ – electron wavefunction amplitudes and $\Phi(s,q_z,x,y,z)$ – deformation potential interaction function:

$$\Phi(s,q_z,x,y,z)=d_c\left(\frac{\partial e_x(s,q_z,x,y,z)}{\partial x}+\frac{\partial e_y(s,q_z,x,y,z)}{\partial y}+\frac{\partial e_z(s,q_z,x,y,z)}{\partial z}\right). \tag{3.23}$$

The matrix element of the electron-phonon interaction by definition is:

$$M_{el-ph}(i\to f)=\langle f|H_{el-ph}|i\rangle\,. \tag{3.24}$$

The initial state $|i\rangle$ is determined by electron wavefunction $\psi(j,n,k_z,x,y,z)=\frac{1}{\sqrt{N}}\varphi(n,k_z,x,y,z)\exp(\mathbf{i}k_z jL_z^0)$ and phonon occupation number $N^0(s,q_z)$. Amplitudes $\varphi(n,k_z,x,y,z)$ are the solutions of the three-dimensional stationary Schrodinger equation. The final state $\langle f|$, after absorption or emission of a phonon $(s,q_z)$ is determined by electron wavefunction $\psi(j,n',k_z',x,y,z)$ and phonon occupation number $N^0(s,q_z)+\frac{1}{2}\pm\frac{1}{2}$, where '+' superscript corresponds to the phonon absorption, while '–' subscript to the phonon emission. The difference between energies of the final and initial states equals to:

$$E_f-E_i=\varepsilon(n,k_z)\pm\hbar\omega(s,q_z)-\varepsilon(n',k_z')\,, \tag{3.25}$$

where $\varepsilon(n,k_z)$ – energy of the *n*-th quantized electron level with wavevector $k_z$ and $\hbar\omega(s,q_z)$ – energy of phonon $(s,q_z)$. Therefore, one can obtain for the matrix element of the electron-phonon interaction in a modulated nanowire the following relation:

$$M_{el-ph}(n,k_z,n',k_z',s,q_z)=\sqrt{\frac{\hbar\left(N^0(s,q_z)+\frac{1}{2}\pm\frac{1}{2}\right)}{2N\bar{\rho}(s,q_z)\omega(s,q_z)}}I(n,k_z,n',k_z',s,q_z)\delta_{k_z',k_z\pm q_z}\,, \tag{3.26}$$

where Kronecker delta resulted from the summation:

$$\frac{1}{N}\sum_{j=1}^{N}\exp\left(\mathbf{i}(k_z\pm q_z-k_z')jL_z^0\right)=\delta_{k_z',k_z\pm q_z}\,. \tag{3.27}$$

In order to obtain the electron-phonon interaction scattering rate from the Fermi golden rule: $\tau_{el-ph}^{-1}(E_i)=\frac{2\pi}{\hbar}\sum_f\left|M_{el-ph}(i\to f)\right|^2\delta(E_f-E_i)$ one needs to summarize over variables $n',s,q_z$. One should keep in mind, that the summation over electron wavevectors $k_z'$ of the final states is unnecessary due to the momentum conservation law $k_z'=k_z\pm q_z$. Thus, one can obtain:

$$\tau^{-1}_{el-ph}(\varepsilon(n,k_z)) = \sum_{n',s,q_z} \frac{\pi\left(N^0(s,q_z)+\frac{1}{2}\pm\frac{1}{2}\right)}{N\bar{\rho}(s,q_z)\omega(s,q_z)}\left|I(n,k_z,n',k'_z,s,q_z)\right|^2 \times . \qquad (3.28)$$
$$\times\delta_{k'_z,k_z\pm q_z}\delta\left(\varepsilon(n,k_z)\pm\hbar\omega(s,q_z)-\varepsilon(n',k'_z)\right)$$

In equation (3.28) one can substitute the summation over $q_z$ with integration using the rule $\sum_{q_z} \to \frac{L_z^0 N}{2\pi}\int dq_z$ :

$$\tau^{-1}_{el-ph}(\varepsilon(n,k_z)) = \sum_{n',s}\int_0^{q_z^{\max}} L_z^0 \frac{N^0(s,q_z)+\frac{1}{2}\pm\frac{1}{2}}{2\bar{\rho}(s,q_z)\omega(s,q_z)}\left|I(n,k_z,n',k'_z,s,q_z)\right|^2 \times . \qquad (3.29)$$
$$\times\delta_{k'_z,k_z\pm q_z}\delta\left(\varepsilon(n,k_z)\pm\hbar\omega(s,q_z)-\varepsilon(n',k'_z)\right)dq_z$$

For the numerical calculations the equation (3.29) is poorly suited due to the delta-function. One can greatly simplify the numerical problem if considers one of the well-known properties of the delta-function: $\int f(x)\delta(g(x))dx = \sum_l \frac{f(x_l)}{\left|g'(x_l)\right|}$, where $x_l$ are the roots of the equation $g(x)=0$.

Thus, for the electron-phonon scattering rate in a modulated nanowire one can finally obtain:

$$\tau^{-1}_{el-ph}(\varepsilon(n,k_z)) = \sum_{n',s}\sum_l \frac{\Gamma(n,k_z,n',s,q_{z,l})}{\left|g(q_{z,l})\right|}, \qquad (3.30)$$

where

$$\Gamma(n,k_z,n',s,q_z) = L_z^0 \frac{N^0(s,q_z)+\frac{1}{2}\pm\frac{1}{2}}{2\bar{\rho}(s,q_z)\omega(s,q_z)}\left|I(n,k_z,n',k_z\pm q_z,s,q_z)\right|^2, \qquad (3.31)$$

and

$$g(q_z) = \frac{\partial\left(\varepsilon(n,k_z)\pm\hbar\omega(s,q_z)-\varepsilon(n',k_z\pm q_z)\right)}{\partial q_z}. \qquad (3.32)$$

In Figure 3.19(a-b) are presented the RT electron-phonon scattering rates with emission and absorption of a phonon for the electron ground state calculated using confined electron and phonon dispersion relations. Due to the ultra-low dimensions of the considered nanowires (limited by available calculation resources) the electron quntization energy for the few lowest levels is much larger than the maximal phonon energy, which constitutes ~ 65 meV. Therefore, only the intrasubband transitions within the electron ground state level were accounted in calculations.

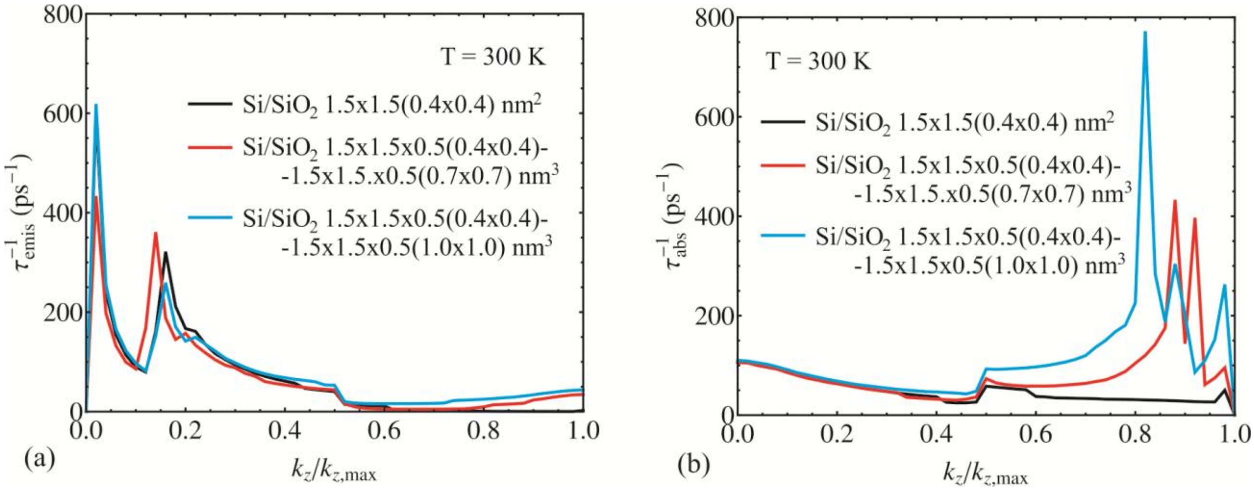

Fig. 3.19. Electron-phonon scattering rate with emission (a) and absorption (b) of a phonon in $Si/SiO_2$ core/shell modulated nanowires at RT.

The numerical analysis of the obtained results together with the derived analytical expressions (see equations (3.31-3.32)) showed that electron-phonon scattering processes associated with an emission of a phonon are characterized by two pronounced peaks at low electron wavevectors and are practically insensitive to the modulated profile of the investigated $Si/SiO_2$ core/shell nanowires. In case of the electron-phonon scattering processes with phonon absorption the scattering rate has few pronounced maximums at high electron wavevectors for the modulated $Si/SiO_2$ nanowires, while is almost constant for all $k_z$ in case of a non-modulated $Si/SiO_2$ nanowire.

## 3.4. Conclusions to chapter 3

In this chapter the effective mass method was applied for investigation of electron energy spectra and electron wave functions in core/shell $Si/SiO_2$ nanowires with constant and periodically modulated cross-section. It was shown, that cross-section modulation strongly influences the electron energy spectra and electron wave functions in Si nanowires. For ground state there appear an inhomogeneity in the wave function distribution along the wire’s axis, namely, the main part of the wave function modulus being localized in the wide segments of the modulated wire.

The lattice dynamics BvK model and the Boltzmann transport equation were applied for investigation of phonon and thermal processes in Si nanowires, Si cross-section modulated nanowires and Si/Ge core/shell cross-section modulated nanowires.

For Si cross-section modulated nanowires it was theoretically demonstrated that phonon heat flux can be significantly suppressed in comparison with the generic uniform cross-section Si nanowires. Redistribution of the phonon energy spectra in the cross-section modulated nanowires leads to a strong decrease of the average phonon group velocities and a corresponding suppression of the phonon thermal flux. This effect was explained by the exclusion of the phonon modes trapped in cross-section modulated nanowires segments from the heat flow. As a result, an up to 5 times drop of the phonon heat flux at RT is predicted for Si cross-section modulated nanowires in comparison with uniform Si nanowires.

For Si/Ge core/shell cross-section modulated nanowires it was found theoretically that a combination of cross-section modulation and acoustic mismatch between Si and Ge materials can lead to an even more drastic reduction of the thermal conductivity. The performed calculations indicate that the RT thermal conductivity of Si/Ge core/shell cross-section modulated nanowires is almost three orders of magnitude lower than that of bulk Si. Thermal flux in the modulated nanowires is suppressed by an order of magnitude in comparison with generic Si nanowires. The effect is explained by modification of the phonon spectra in modulated nanowires leading to decrease of the phonon group velocities and localization of certain phonon modes in narrow or wide nanowire segments.

The analytical expression for the electron-phonon scattering rate with emission and absorption of a phonon in Si/$SiO_2$ core/shell modulated nanowires was derived in the deformation potential approach. It was shown that cross-section modulation of the Si core results in a substantial modification of the RT electron-phonon scattering rate with phonon absorption.

The obtained theoretical results demonstrate that geometry modulation is an efficient instrument in engineering electrons and phonons in Si-based nanowires, which proved to be excellent candidates for thermoelectric and thermal insulator applications due to extremely low values of thermal conductivity.

All numerical simulations presented in this chapter were carried out entirely by the author, while theoretical derivations and data analysis was done in close collaboration and under supervision of scientifc advisor. The results of these investigations were published in the research articles [37, 165].

# 4. PHONON PROCESSES IN MULTILAYER GRAPHENE WITH DIFFERENT ATOMIC STACKING

## 4.1. Theoretical model for phonons in multilayer graphene

Graphene i.e. a single layer of carbon atoms arranged in a pristine honeycomb pattern, is a promising material for future electronics because of its unique electrical [84], thermal [86-87] and optical [166-167] properties. The high electrical [84, 165] and thermal [86-87] conductivities of graphene are crucial for its proposed applications in field-effect transistors [168], sensors [169], solar cells [170], resonators [171] and thermal management of ultra-large scale integrated circuits and high-power-density devices [87, 172-174]. Multi-layer graphene flakes, which are easy to produce, also posses unusual physical properties: depending on the stacking configuration Bernal or rhombohedral, they demonstrate metallic- or semiconductor-like behavior [175]. Thermal properties of Bernal stacked multi-layer graphene are highly sensitive to the number of layers [95]: the RT thermal conductivity decreases from ~2800 to ~1300 $\mathrm{Wm^{-1}K^{-1}}$ as the number of layers increases from 2 to 4 [95], which is explained by the changes in the phonon energy spectra and phonon scattering space [176-177].

Despite of the fact that numerous scientific studies of the thermal properties in Bernal stacked multi-layer graphene (ABA, ABAB, ABABA, etc.) have been carried out in the last few years, the phonon and thermal properties in multi-layer graphene with rhombohedral stacking order (ABC, ABCA, ABCAB, etc.) as well as in twisted graphene, when parallel carbon layers are rotated relatively to one another in a specific manner [178], were not studied yet. This investigation is very important and timely because change in the phonon properties in rhombohedral stacked or twisted multi-layer graphene in comparison with generic Bernal stacking may significantly modify its thermal properties.

In order to study the phonon processes in single- and multi-layer graphene it was developed a lattice dynamics model in framework of the BvK lattice dynamics theory [38]. Within the BvK model the set of equations of motion for atoms can be written in a harmonic approximation as:

$$m_k \ddot{u}_\alpha(jk) = -\sum_{\beta, j', k'} \Phi_{\alpha\beta}(jk, j'k') u_\beta(j'k') \qquad \alpha, \beta = x, y, z\,, \tag{4.1}$$

where $m_k$ and $u(jk)$ is the mass and displacement of the $k$-th atom in the $j$-th unit cell respectively, $\Phi_{\alpha\beta}(jk, j'k')$ is the interatomic force constants describing the interaction between atoms $jk$ and $j'k'$. The unit cell of single-layer graphene contains 2 atoms (any pair of nearest-neighbor “blue” and “red” atoms in Figure 4.1 below), while unit cell of multi-layer graphene with Bernal or rhombohedral stacking contains *2n* atoms, where *n* is number of graphene layers. Thus, the total number of equations of motion is *6n*. The solution of differential equations (4.1) represents a superposition of plane waves with frequency $\omega$ and wave vector $\vec{q}$:

$$u_\alpha(jk) = \frac{1}{\sqrt{m_k}} \sum_{\vec{q}} e_{k,\alpha}(\vec{q}) \exp\left(\mathbf{i}\left(\vec{q}\vec{r}_j - \omega t\right)\right), \tag{4.2}$$

where $\vec{e}_k$ is the *k*-th atom vector of displacement amplitudes and $\vec{r}_j$ is the radius vector of the *j*-th unit cell. Substituting equation (4.2) into the equations of motion (4.1), one obtains:

$$\omega^2 e_{k,\alpha}(\vec{q}) = \sum_{\beta,k'} D_{\alpha\beta}(kk';\vec{q}) e_{k',\beta}(\vec{q}), \tag{4.3}$$

with the dynamic matrix:

$$D_{\alpha\beta}(kk';\vec{q}) = \frac{1}{\sqrt{m_k m_{k'}}} \sum_{j'} \Phi_{\alpha\beta}(jk, j'k') \exp\left(\mathbf{i}\left(\vec{r}_{j'} - \vec{r}_j\right)\vec{q}\right). \tag{4.4}$$

After the dynamic matrix (4.4) is constructed, the eigenvalues (i.e. phonon frequencies) and eigenvectors (i.e. atomic displacement amplitudes) are obtained by solving the secular equation:

$$\left|\omega^2 - D(\vec{q})\right| = 0. \tag{4.5}$$

In calculations it was taken into account four nearest-neighbor atomic spheres of the intralayer interaction and two nearest-neighbor spheres of the interlayer interaction. A schematic view of the in-plane atomic spheres is presented in Figure 4.1.

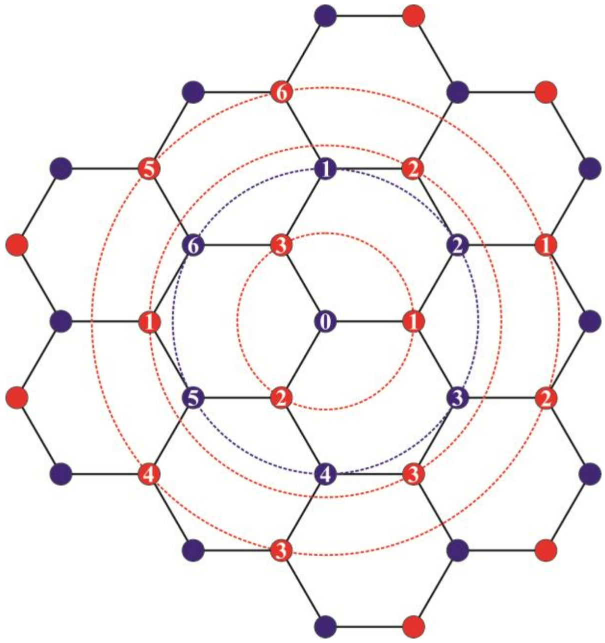

Fig. 4.1. Four nearest atomic spheres in a graphene plane.

The coordination vectors $\vec{r}_{j'}-\vec{r}_j$ of atoms from the four atomic spheres of a “blue” atom are listed in Table 4.1. The vectors $\vec{r}_{j'}-\vec{r}_j$ of the atoms from the four atomic spheres of a “red” atom can be found by the rotation of the corresponding vector from Table 4.1 by the angle $\pi$ around the (0,0)-point.

Table 4.1. Coordination vectors of atoms in a graphene plane.

| Atom # (*j'*) | 1st sphere | 2nd sphere | 3rd sphere | 4th sphere |
|---|---|---|---|---|
| 1 | $(a,0)$ | $(0,\sqrt{3}a)$ | $(-2a,0)$ | $(5a/2,\sqrt{3}a/2)$ |
| 2 | $(-a/2,-\sqrt{3}a/2)$ | $(3a/2,\sqrt{3}a/2)$ | $(a,\sqrt{3}a)$ | $(5a/2,-\sqrt{3}a/2)$ |
| 3 | $(-a/2,\sqrt{3}a/2)$ | $(3a/2,-\sqrt{3}a/2)$ | $(a,-\sqrt{3}a)$ | $(-a/2,-3\sqrt{3}a/2)$ |
| 4 | – | $(0,-\sqrt{3}a)$ | – | $(-2a,-\sqrt{3}a)$ |
| 5 | – | $(-3a/2,-\sqrt{3}a/2)$ | – | $(-2a,\sqrt{3}a)$ |
| 6 | – | $(-3a/2,\sqrt{3}a/2)$ | – | $(-a/2,3\sqrt{3}a/2)$ |

Note that *z*th component of all atoms is omitted in the notations, since different parallel graphene planes posses the same hexagonal symmetry. In the considered multi-layer graphene structures the graphene sheets can only be shifted (as in Bernal or rhombohedral stacking) or rotated (as in twisted stacking) in the graphene plane, relative to one another.

Since the components of the dynamic matrix are determined by the interatomic force constants (see equation (4.4)), the main problem in obtaining the phonon data within a BvK model of lattice dynamics is the corresponding choice of the set of force constant matrices $\Phi$. The force constant matrix describing the interaction of an atom with its $s^{\text{th}}$ nearest-neighbor intralayer sphere has the form: $\Phi_s=-\begin{pmatrix}\alpha_s & 0 & 0\\ 0 & \beta_s & 0\\ 0 & 0 & \gamma_s\end{pmatrix}$. The force constant matrices for all atoms from four neighbor atomic spheres can be found from $\Phi_s$ using the rotations around *Z*-axis by an angle $\varphi$ in a clock-wise direction $R_\varphi=\begin{pmatrix}\cos\varphi & \sin\varphi & 0\\ -\sin\varphi & \cos\varphi & 0\\ 0 & 0 & 1\end{pmatrix}$ and the reflections in *XZ*-plane:

$\sigma_y = \begin{pmatrix} 1 & 0 & 0 \\ 0 & -1 & 0 \\ 0 & 0 & 1 \end{pmatrix}$. In Table 4.2 we present a list of corresponding symmetry operations which map the matrix $\Phi_s$ into force constant matrices for all atoms from the first four atomic spheres.

Table 4.2. Force constant matrices of intralayer interaction.

| Atom # (*j'*) | 1st sphere | 2nd sphere | 3rd sphere | 4th sphere |
|---|---|---|---|---|
| 1 | $\Phi_1$ | $\Phi_2$ | $\Phi_3$ | $\sigma_y\left(R_{\pi/6}\Phi_4R_{\pi/6}^{-1}\right)\sigma_y^{-1}$ |
| 2 | $R_{2\pi/3}\Phi_1R_{2\pi/3}^{-1}$ | $\sigma_y\left(R_{2\pi/3}\Phi_2R_{2\pi/3}^{-1}\right)\sigma_y^{-1}$ | $R_{2\pi/3}\Phi_3R_{2\pi/3}^{-1}$ | $R_{\pi/6}\Phi_4R_{\pi/6}^{-1}$ |
| 3 | $R_{4\pi/3}\Phi_1R_{4\pi/3}^{-1}$ | $R_{2\pi/3}\Phi_2R_{2\pi/3}^{-1}$ | $R_{4\pi/3}\Phi_3R_{4\pi/3}^{-1}$ | $\sigma_y\left(R_{4\pi/3}\Phi_4R_{4\pi/3}^{-1}\right)\sigma_y^{-1}$ |
| 4 | – | $\sigma_y\Phi_2\sigma_y^{-1}$ | – | $R_{2\pi/3}\Phi_4R_{2\pi/3}^{-1}$ |
| 5 | – | $R_{4\pi/3}\Phi_2R_{4\pi/3}^{-1}$ | – | $\sigma_y\left(R_{2\pi/3}\Phi_4R_{2\pi/3}^{-1}\right)\sigma_y^{-1}$ |
| 6 | – | $\sigma_y\left(R_{4\pi/3}\Phi_2R_{4\pi/3}^{-1}\right)\sigma_y^{-1}$ | – | $R_{4\pi/3}\Phi_4R_{4\pi/3}^{-1}$ |

The intralayer interaction for each atomic sphere is described by three independent force constants: $\alpha_s$, $\beta_s$ and $\gamma_s$. In BvK model these constants have a clear physical meaning. A displacement of an atom induces a force towards its *s*th neighbor. The force constant $\alpha$ describes the longitudinal component of the force while constants $\beta$ and $\gamma$ describe the in-plane and out-of-plane transverse components, respectively.

The force constant matrix describing the interaction of an atom with its 1st nearest-neighbor interlayer sphere has the form: $\Phi = -\begin{pmatrix} \hat{\alpha}_1 & 0 & 0 \\ 0 & \hat{\alpha}_1 & 0 \\ 0 & 0 & \hat{\gamma}_1 \end{pmatrix}$ and for the 2nd nearest-neighbor interlayer sphere: $\Phi = -\begin{pmatrix} \hat{\alpha}_2 & 0 & 0 \\ 0 & \hat{\alpha}_2 & 0 \\ 0 & 0 & 0 \end{pmatrix}$. Therefore, the total number of the force constants in the proposed model is 15, i.e. 12 for the intralayer interaction and 3 for the interlayer interaction. One should note here, that in the case of single-layer graphene the interlayer interaction, obviously, should not be taken into account since it is only one layer thick and the number of force constants is reduced to 12 in this case.

In calculations were used the force constants fitted in Ref. [179] to density functional theory results, which are in a good agreement with experimental phonon dispersion frequencies of bulk graphite. The numerical values of the force constants are listed in Table 4.3.

Table 4.3. Interatomic force constants obtained from a fit to experimental phonon frequencies of graphite (in units N/m).

| Intralayer | | | interlayer |
|---|---|---|---|
| $\alpha_1 = 398.7$ | $\beta_1 = 172.8$ | $\gamma_1 = 90.0$ | $\hat{\alpha}_1 = -4.0$ |
| $\alpha_2 = 72.9$ | $\beta_2 = 46.1$ | $\gamma_2 = -0.8$ | $\hat{\gamma}_1 = 5.8$ |
| $\alpha_3 = -15.0$ | $\beta_3 = 33.1$ | $\gamma_3 = 0.8$ | $\hat{\alpha}_2 = 0.55$ |
| $\alpha_4 = 1.0$ | $\beta_4 = 7.9$ | $\gamma_4 = -6.3$ | |

## 4.2. Phonon processes in single-layer, two-layer, three-layer graphene and graphite

### 4.2.1. Energy spectra and vibrational properties

The schematic view of the single-layer, AB two-layer, ABA (Bernal) three-layer and ABC (rhombohedral) three-layer graphene is shown in Figure 4.2.

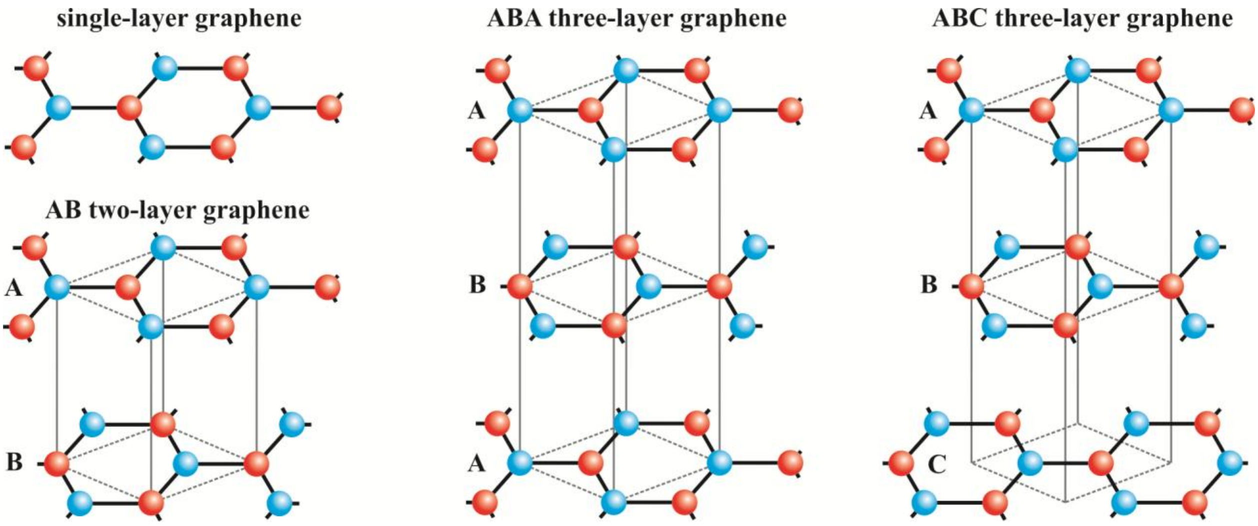

Fig. 4.2. Schematics of single-, two- and three-layer graphene.

In Figures 4.3-4.4 is presented the phonon energy spectrum for single-layer and two-layer graphene, obtained within BvK model of lattice dynamics.

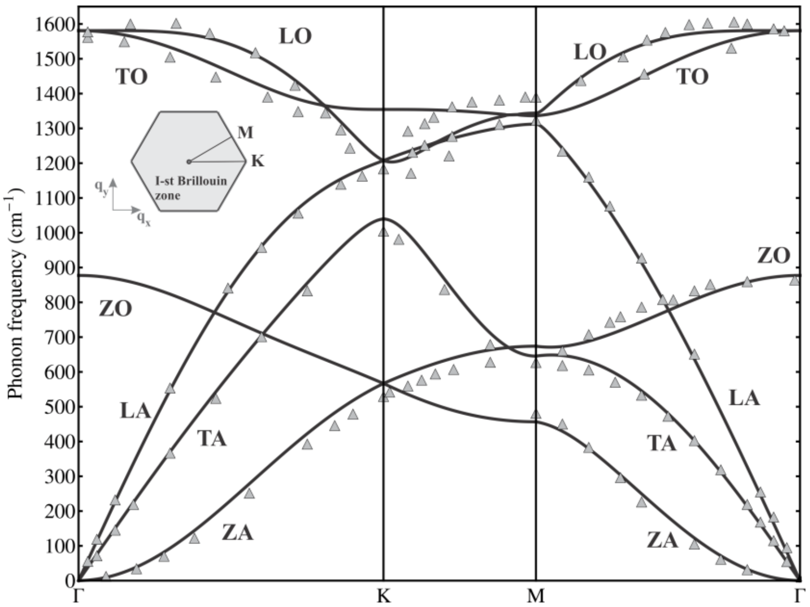

Fig. 4.3. Vibrational spectrum of the monolayer graphene. Symbols $\Gamma$, $\mathrm{K}$ and $\mathrm{M}$ denote high symmetry points of the first BZ. Experimental data points (gray triangles) for graphite from Refs. [176-177] are also shown for comparison.

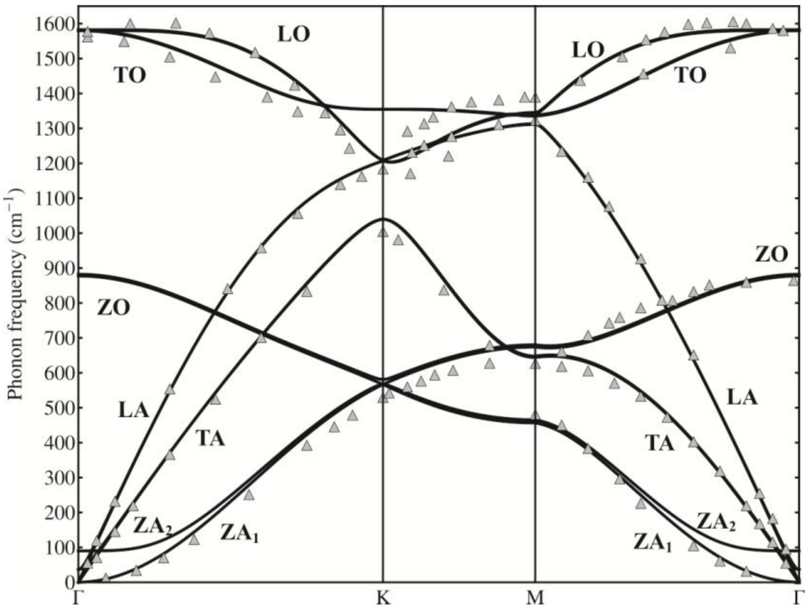

Fig. 4.4. Vibrational spectrum of the AB-stacked two-layer graphene. Experimental data points (gray triangles) for graphite from Refs. [176-177] are also shown for comparison.

As can be seen from the figures, our calculated results are in a good agreement with experimental data from Refs. [176-177] for all phonon branches: in-plane acoustic branches (LA and TA), in-plane optic branches (LO and TO), out-of-plane acoustic (ZA) and optic (ZO) branches. A weak interlayer coupling between graphene layers (see Table 4.3, where interlayer force constants are much less than intralayer ones) results in appearance of almost doubly degenerate phonon branches in the case of two-layer graphene compared with monolayer result. The only exception constitutes the low-frequency $ZA_2$ mode with frequency of about 90 cm$^{-1}$ at $\Gamma$, which arises from interlayer movement (see also Figure 4.6(b) below). An interesting behavior demonstrates out-of-plane acoustic ZA branch, in contrast to the linear dispersion near the $\Gamma$ point for the in-plane TA and LA branches, it shows a $q^2$ dispersion, which is a characteristic feature for layered crystals [118, 180].

In Figure 4.5 we show the atomic displacements in graphene and two-layer graphene structures, which correspond to different types of acoustic vibrations at $\Gamma$ point.

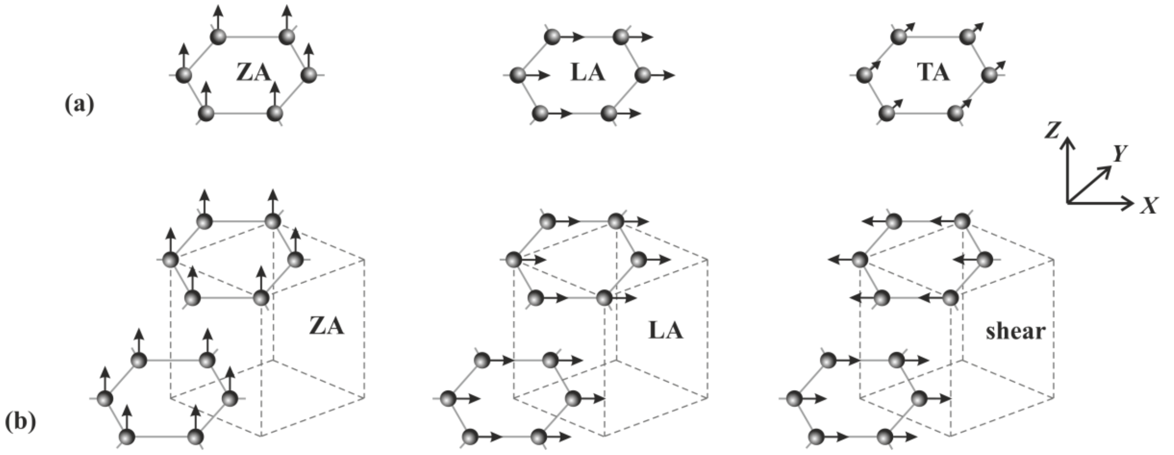

Fig. 4.5. Acoustic vibrational motion in graphene (a) and AB-stacked two-layer graphene (b).

In single-layer graphene there is only three types of acoustic modes at $\Gamma$ point: out-of-plane (ZA), longitudinal in-plane (LA) and transversal in-plane (TA). As number of graphene layers increases from 1 to 2 (Figure 4.5(b)) additional vibrational mode appears – in-plane shear, in which parallel graphene layers slide one over another in opposite directions. An important thing to note here is that acoustic shear mode has non-zero frequency of about 36 cm$^{-1}$ at the zone center and it has $E_g$ symmetry type, which makes it Raman active and thus it can be observed experimentally.

Besides acoustic phonons, that are main heat carriers in graphene [87, 95], optical phonon modes are also of a fundamental importance. It was demonstrated experimentally [181-183], that optical zone-center modes provide significant information about the layer number and the stacking geometry of graphene layers. The numerical values of optical phonon frequencies calculated within BvK model are listed in Table 4.4.

Table 4.4. High-frequency optical phonons (in units cm$^{-1}$) at $\Gamma$ for single-layer graphene, two-layer graphene and graphite. In parenthesis are indicated the mode symmetries.

|  | Graphene (BvK model) | Graphene (VFF model [88]) | AB bilayer graphene (BvK model) | Graphite (experiment [176-177]) |
|---|---|---|---|---|
| $\Gamma$ | 1581 ($E_{2g}$) | 1554 ($E_{2g}$) | 1580 ($E_g$)<br>1582 ($E_u$) | 1580 ($E_{2g}$) |

As can be seen from the Table 4.4 BvK value for frequency of $E_{2g}$ mode of graphene (1581 cm$^{-1}$) is much closer to the experimental value of graphite (1580 cm$^{-1}$) than the value obtained within VFF lattice dynamics model (1554 cm$^{-1}$ [88]). This can be attributed to the difference in fitting precision, since the number of fitting parameters in the proposed BvK model is two times larger than in Valence Force Field model. Also, compared with the monolayer result, in AB-stacked two-layer graphene one can observe a splitting of the highest optical mode: $E_{2g}$ mode in the monolayer evolves into $E_g$ and $E_u$ modes for AB two-layer. The splitting is due to the weak interlayer coupling and constitutes about 2 cm$^{-1}$. Moreover, the group theory predicts that $E_{2g}$ and $E_g$ modes are Raman active, while $E_u$ is infrared active. Therefore, a combination of Raman and infrared spectroscopic measurements can provide a complete picture of zone-center optical modes.

In Figure 4.6 is shown the schematic atomic displacements of zone-center optical vibrations in graphene and two-layer graphene.

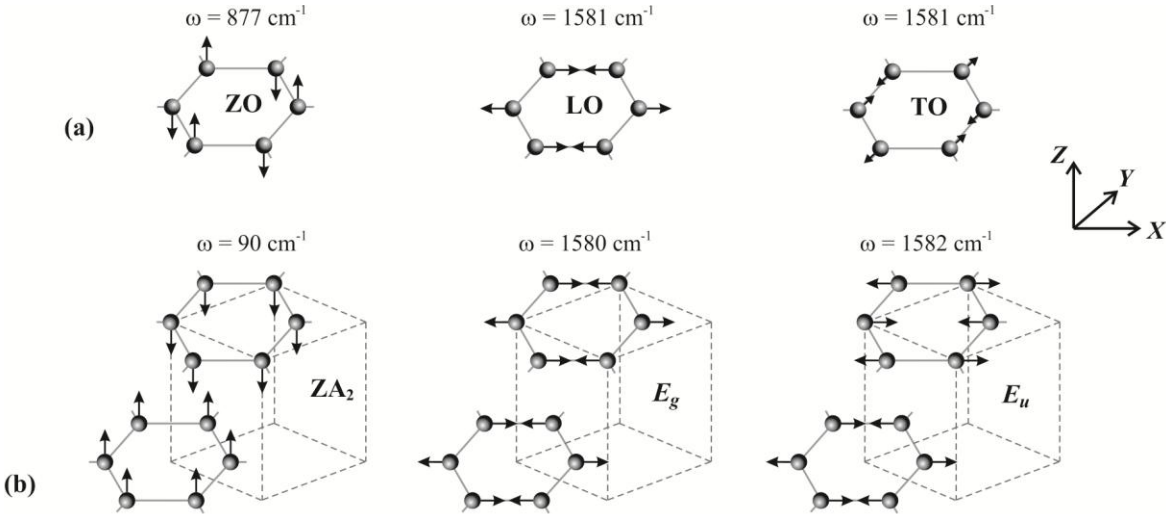

Fig. 4.6. Optical vibrations in graphene (a) and AB-stacked two-layer graphene (b).

As in the case of acoustic vibrations, in graphene exist three types of optical vibrational motion at $\Gamma$ point (Figure 4.6(a)): out-of-plane (ZO), longitudinal in-plane (LO) and transversal in-plane (TO). In two-layer graphene system, because of the 4 atoms in one unit cell, the zone-center optical vibration is more complex. In Figure 4.6(b) are presented few types of optical eigenmodes with different frequencies. It is clearly seen from the figure that two splitted high frequency optical modes $E_g$ and $E_u$ are characterized by the in-plane vibrations, while the low-frequency ZA$_2$ mode arises from the interlayer motion along the $Z$-axis. Since in ZA$_2$ mode the top and bottom layers move in opposite directions, it results in compression of graphene bilayer.

In Figure 4.7 is presented the phonon energy spectrum of three-layer graphene with ABA stacking order, obtained within BvK model of lattice dynamics.

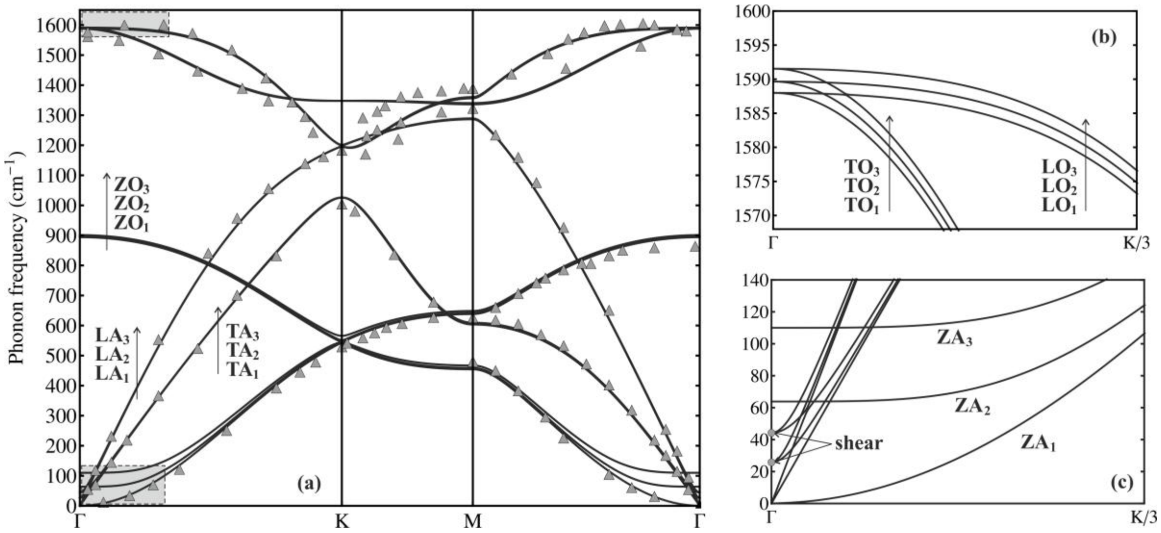

Fig. 4.7. Vibrational spectrum of the three-layer ABA graphene. Symbols $\Gamma$, K and M denote high symmetry points of the first BZ. Experimental data points (gray triangles) for graphite from Refs. [176-177] are also shown for comparison.

Calculations of phonon spectrum for ABC three-layer graphene gave the same result, with a difference in phonon frequencies less than 1 cm$^{-1}$. Therefore one can conclude, that phonon spectrum of three-layer graphene is practically insensitive to the stacking geometry. However, that does not mean that vibrational properties are also the same, since the different phonon modes can posses different symmetries and can interact differently with electrons, photons, etc.

One can see from Figures 4.7(a-c) that in three-layer graphene there is almost threefold degeneracy of phonon branches, with a small splitting ~2 cm$^{-1}$ because of the weak interlayer coupling. The only exception constitutes low-frequency ZA modes, which are characterized by out-of-plane vibrations (see Figure 4.8 below) and thus are very sensitive to the number of layers and interlayer interaction. Analyzing the evolution of the ZA modes from single-layer to two-layer graphene (Figure 4.3 and 4.4), and from two-layer to three-layer graphene, we can reach to the conclusion that number of ZA phonons is uniquely determined by the number of graphene layers, namely the number of ZA branches is equal to the number of graphene layers. This statement is confirmed by the recent doubly resonant Raman measurements of out-of-plane phonons in high-quality multilayer graphene [184]. Moreover, it was obtained a good agreement between calculated values of ZA phonon frequencies in three-layer graphene and corresponding experimental values from Ref. [184], the discrepancy constitutes only a few cm$^{-1}$.

In Figure 4.8 are presented the schematic atomic displacements in three-layer graphene with ABA and ABC stacking order, which correspond to out-of-plane vibrations at $\Gamma$ point.

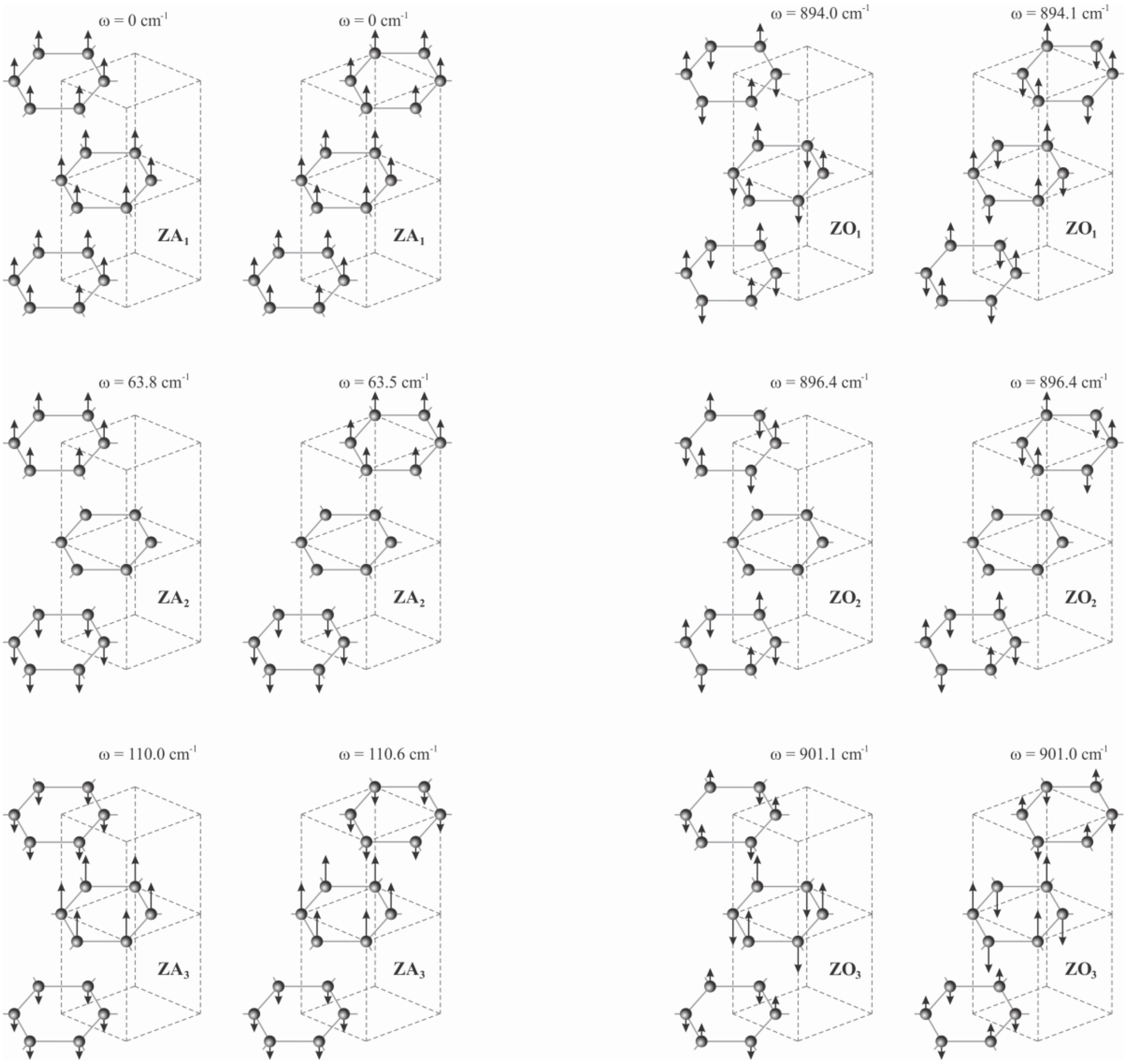
ω = 0 cm-1
ω = 0 cm-1
ω = 894.0 cm-1
ω = 894.1 cm-1
ZA1
ZA1
ZO1
ZO1
ω = 63.8 cm-1
ω = 63.5 cm-1
ω = 896.4 cm-1
ω = 896.4 cm-1
ZA2
ZA2
ZO2
ZO2
ω = 110.0 cm-1
ω = 110.6 cm-1
ω = 901.1 cm-1
ω = 901.0 cm-1
ZA3
ZA3
ZO3
ZO3

Fig. 4.8. Different types of out-of-plane vibrations in ABA and ABC three-layer graphene.

From Figure 4.8 one can see that in ABA and ABC three-layer graphene there is three acoustic out-of-plane modes: $ZA_1$, $ZA_2$, $ZA_3$ and three optic out-of-plane modes: $ZO_1$, $ZO_2$, $ZO_3$. All these modes can be classified by symmetry type according to the group theory and thus can be predicted whenever a mode is Raman/IR active or silent. For instance, from Figure 4.8 one can observe that in $ZA_2$ mode the top and bottom layers move in opposite directions while the middle layer remains unmoved, therefore this mode is symmetric and according to the group theory it is Raman active. The $ZA_3$ modes are not symmetric and should not be observable in Raman measurements, since the top and bottom layers in these modes move in the same direction, while the movement of the middle layer is opposite to them. However, recent experiments on ZA phonons in graphene multilayers [184] demonstrate that all of the low-frequency ZA modes can be observed in Raman spectroscopy, leaving the question of correct theoretical and experimental interpretation of ZA modes in few-layer graphene to be still open.

Another interesting feature of few-layer graphene is the existence of the in-plane zone-center shear modes (see Figure 4.7(c) and Figure 4.9 below), in which parallel graphene layers slide one over another. Although these vibrations appear to be acoustic-like and take place only in the plane of the graphene layers, they demonstrate a nonlinear behavior close to the BZ center and have a non-zero frequency about ~26 $\text{cm}^{-1}$ and ~44 $\text{cm}^{-1}$ in the case of three-layer graphene. The schematic view of the atomic displacements from the shear modes is presented in Figure 4.9.

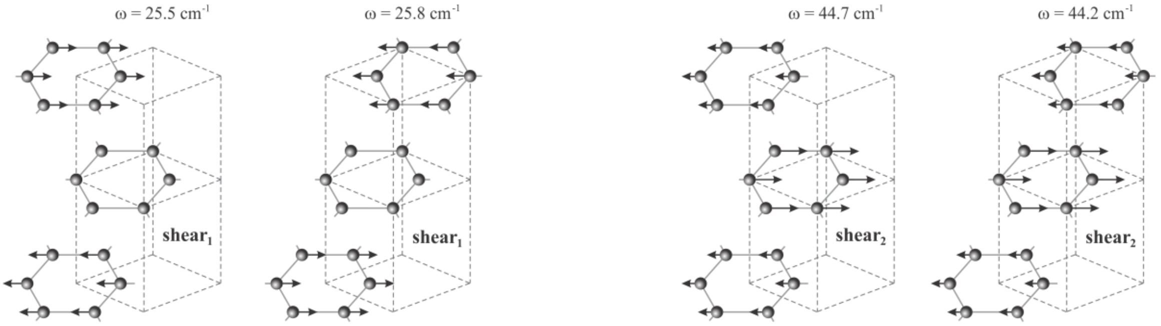

Fig. 4.9. Shear vibrational modes in ABA and ABC three-layer graphene.

Since these low-lying shear modes have a non-zero frequency at the $\Gamma$ point, their position is determined by the interlayer coupling and thus they can be used for probing directly the interlayer interaction strength in multilayer graphene.

### 4.2.2. Phonon scattering processes and thermal properties

Phonon scattering in graphene is determined by three basic mechanisms: (i) phonon – phonon umklapp scattering, (ii) phonon – point-defect scattering, i.e. phonons being scattered by a point defect within a graphene lattice, and (iii) phonon – boundary scattering where phonons are scattered by the boundaries of the graphene sample. All three mechanisms are treated within a relaxation rate approach, thus the total phonon relaxation time is given by:

$$\tau_{tot,s}^{-1}(q)=\tau_{U,s}^{-1}(q)+\tau_{pd,s}^{-1}(q)+\tau_{b,s}^{-1}(q)\,, \tag{4.6}$$

where $\tau_U$, $\tau_{pd}$ and $\tau_b$ are relaxation times in umklapp, point-defect and boundary scattering, respectively.

In the case of Umklapp scattering, only three-phonon scattering processes were taken into account and the phonon relaxation time was calculated using the Klemens's approach from [88], applied to the single-layer graphene case:

$$\tau_{U,s}^{-1}(q) = \frac{k_B T \bar{\gamma}_s^2}{m\upsilon_s^2(q)} \frac{\omega_s^2(q)}{\omega_{\max,s}} . \tag{4.7}$$

Here $m$ = 19.9442 x $10^{-27}$ kg is the mass of a carbon atom, $\bar{\gamma}_s$ is the average Gruneisen parameter for phonon branch $s$ ($\bar{\gamma}_{ZA} = -5.0$; $\bar{\gamma}_{TA} = 1.0$; $\bar{\gamma}_{LA} = 2.0$; $\bar{\gamma}_{ZO} = -1.0$; $\bar{\gamma}_{TO} = 2.2$; $\bar{\gamma}_{LO} = 2.0$) [185] and $\omega_{\max,s}$ is the maximal phonon frequency of the branch $s$.

Scattering of phonons on point-defects was modeled by the following expression [88]:

$$\tau_{pd,s}^{-1}(q) = \frac{S_0 G}{4} \frac{\omega_s^2(q)}{\upsilon_s(q)} q , \tag{4.8}$$

where $S_0 = \frac{a^2}{4}$ is the cross-section area per one atom in the graphene lattice ($a$ is the smallest carbon-carbon distance), $G$ is the measure of the strength of the point-defect scattering. In present calculations was used a fixed value of the parameter $G = 0.1$ taken from Ref. [88].

The scattering of phonons on graphene boundaries were studied using the Ziman model [88, 122]:

$$\tau_{b,s}^{-1}(q) = \frac{1-p}{1+p} \frac{|\upsilon_s(q)|}{d} , \tag{4.9}$$

where $d$ is the width of a graphene layer and $p$ is the specularity parameter, which depends on the roughness of the graphene edges. Specularity parameter can take values between 0 (fully diffusive scattering) and 1 (fully specular scattering).

Thermal conductivity in graphene has been investigated both theoretically and experimentally. Experimental studies of the thermal conductivity were carried out using optothermal [86-87, 95] or electrical self-heating methods [93, 186]. It was found experimentally that single-layer graphene possess a record-high thermal conductivity in the range 3000–5000 $\mathrm{Wm^{-1}K^{-1}}$ [86, 172] at the RT. Since the main heat carriers in graphene are phonons, it is their unusual properties which determine its extremely high thermal conduction parameters.

Theoretical investigations of graphene's thermal properties employed different models of molecular dynamics simulations and BTE approach [88, 172-174, 187-189]. Within the BTE approach in the relaxation time approximation [88] the thermal conductivity of a graphene flake is defined by the following equation:

$$\kappa^{graphene} = \frac{1}{4\pi k_B T^2 h} \sum_s \int \left(\hbar\omega_s(q)\upsilon_s(q)\right)^2 \tau_{tot,s}(q) \frac{exp\left(\hbar\omega_s(q)/k_B T\right)}{\left(exp\left(\hbar\omega_s(q)/k_B T\right)-1\right)^2} q dq . \tag{4.10}$$

Here $k_B$ - Boltzmann's constant, $T$ – temperature, $h$ is the thickness of graphene flake (e.g. $h$=0.35 nm for single-layer graphene), $s$ enumerates phonon branches, $\hbar$ - Planck's constant, $q$ – phonon wave vector, $\omega$ - phonon frequency, $\upsilon$ - phonon group velocity, $\tau_{tot}$ - total phonon relaxation time determined by equations (4.6)-(4.9).

In Figure 4.10 is presented the phonon energy spectrum along $\Gamma - \mathrm{K}$ direction in BZ and mode-by-mode contributions to the room-temperature thermal conductivity in 10μm-wide graphene layer.

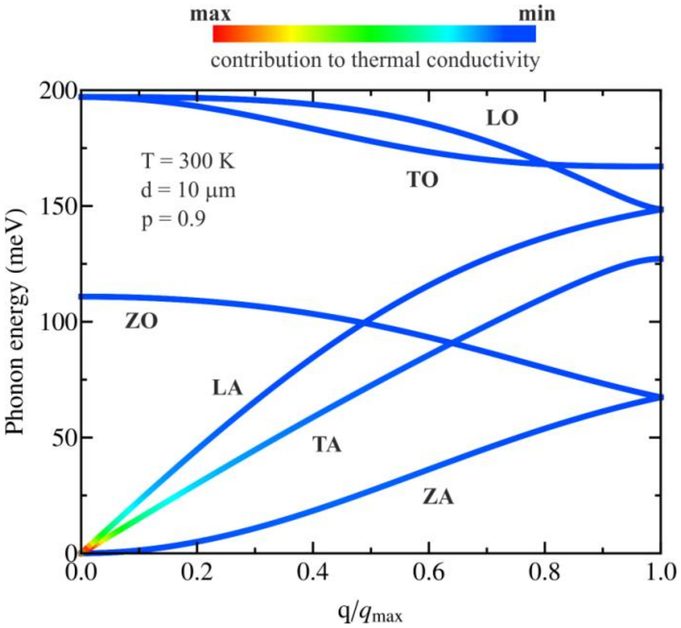

Fig. 4.10. Phonon energy spectrum and mode-specific contributions to thermal conductivity in single-layer graphene.

From Figure 4.10 can be observed that a vast majority of the heat (~99%) is transferred by low-energy in-plane acoustic phonons LA and TA, while the contribution to the thermal transport from other phonon modes is significantly reduced. This result is mainly caused by the difference in average Gruneisen parameters and group velocities. Indeed, at the RT all phonon modes are excited and umklapp scattering is a dominant mechanism of phonon relaxation. From equation (4.7) we can see that characteristic time of umklapp scattering process is proportional to $\tau_{U,s} \sim \left( \frac{\upsilon_s}{\bar{\gamma}_s} \right)^2$ and thus, LA and TA phonons which posses very large group velocities (respectively 20.4 km/s and 13.5 km/s near BZ center) and a relatively small Gruneisen parameters, have significantly larger lifetimes, while the other acoustic phonon – ZA, due to a very small group velocity (less than 0.3 km/s near zone center) and a large Gruneisen parameter, is strongly scattered and therefore eliminated from the heat transfer. Contribution from optical phonon modes is also strongly suppressed due to very low group velocities. However, we would like to note here that the question of the relative contribution of different phonon polarization is still open, since some of the recent theoretical results, based on the exact solution of BTE and molecular dynamics simulations [187-188], suggest that ZA phonons could be the main heat carriers in graphene due to additional selection rules imposed on the phonon-phonon scattering space.

In Figure 4.11 are shown temperature dependencies of thermal conductivity in graphene for different layer widths: $d$ = 1,5,10 and 15 μm. All calculations were performed for a fixed value of specular parameter $p$ = 0.9.

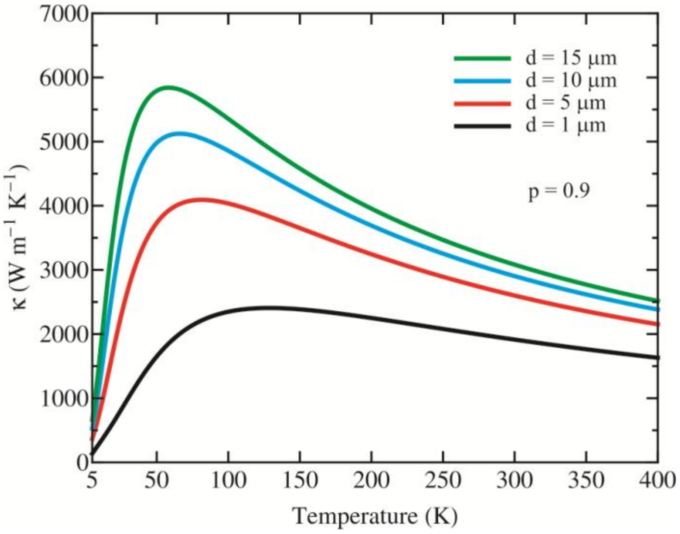

Fig. 4.11. Phonon thermal conductivity of single-layer graphene as a function of temperature for different layer widths.

One can see from Figure 4.11 that graphene layers of larger width have larger thermal conductivity in all temperature range due to a weaker boundary scattering from layer edges, which indicates that besides phonon-phonon umklapp scattering processes boundary scattering also plays an important role in limiting the heat transfer through graphene layers. The maximum thermal conductivity value of ~6000 $Wm^{-1}K^{-1}$ is reached for 15-μm-wide layer at 60 K. An interesting behavior demonstrates the position of maximum on the temperature dependence curves. The maximum thermal conductivity shifts to higher temperatures with decrease of $d$, from $T$ ~ 60 K for 15-μm-wide layer to $T$ ~ 120 K for 1-μm-wide layer. This behavior can be explained as follows: the position of the thermal conductivity maximum separates the low-temperature region, where phonon scattering is mainly due to the boundary, from the high-temperature region, where umklapp scattering is dominant. In a narrower layer the boundary scattering is stronger in a comparison with a wider one (see equation (4.9)) and dominates up to higher temperatures, therefore the position of the maximum shifts to the right. Also, the contribution of the phonon – point-defect scattering processes with parameter $G = 0.1$ has a much weaker influence on thermal conductivity of graphene than the two above mentioned scattering mechanisms.

Another interesting question is the influence of the quality of the graphene boundary edges on its thermal conductivity. In Figure 4.12 is plotted the RT thermal conductivity as a function of layer width for different values of specularity parameter *p*.

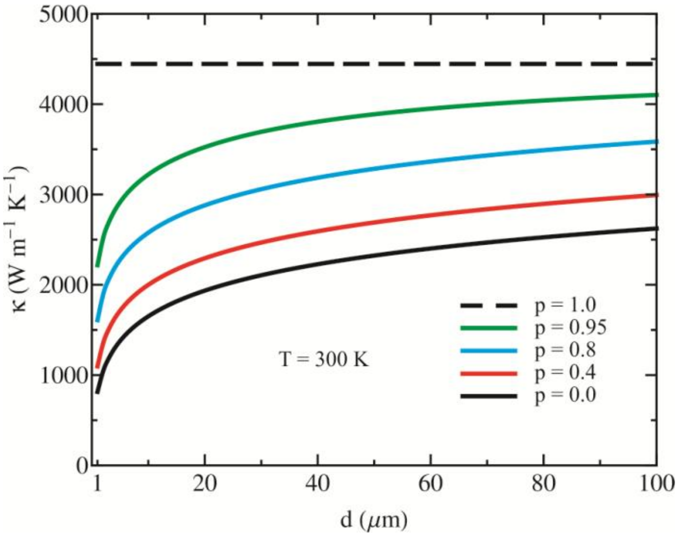

Fig. 4.12. Room temperature phonon thermal conductivity as a function of graphene layer width for different values of boundary roughness parameter *p*.

The parameter *p* is explicitly related to the edge roughness: *p* = 0 means maximum roughness and *p* = 1 means no roughness (smoothness). The rise of the thermal conductivity with increase of layer width is explained by the reduction of the phonon boundary scattering rate. In Figure 4.12 the black dashed line corresponds to a specular boundary scattering (*p*=1) which does not add to thermal resistance, so umklapp and point-defect scattering are the only mechanisms limiting the thermal conductivity in this case. When *p* is approaching 0 the boundary scattering starts to play a dominant role, resulting in a strong decrease of thermal conductivity, e.g. for a 10-μm-wide graphene layer thermal conductivity reduces by almost 40% from 2580 Wm$^{-1}$K$^{-1}$ for *p* = 0.8 to 1650 Wm$^{-1}$K$^{-1}$ for *p* = 0.0.

In Figure 4.13 is presented the phonon energy spectrum along $\Gamma - \mathrm{K}$ direction and mode-by-mode contributions to the RT thermal conductivity of AB two-layer graphene with 10μm width.

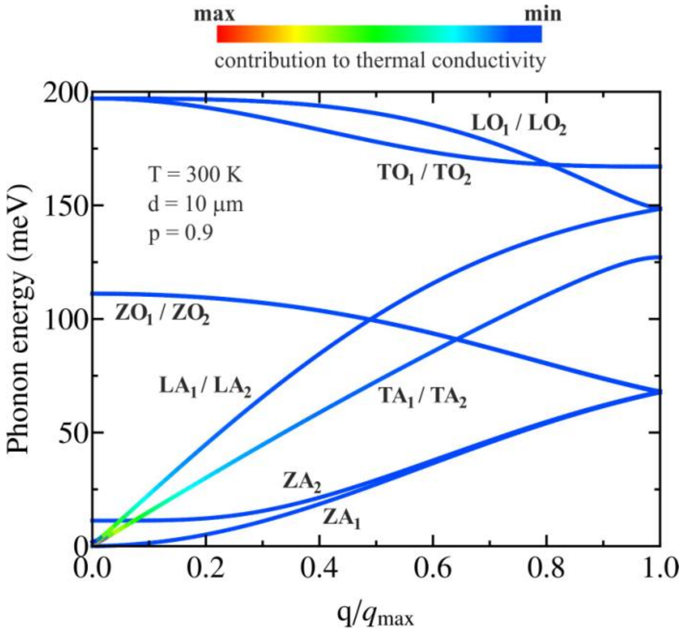

Fig. 4.13. Phonon energy spectrum and mode-specific contributions to thermal conductivity in two-layer graphene with AB stacking.

In Figure 4.13 maximum contribution to the heat transport corresponds to red color, while minimum contribution to blue color. The performed calculations show that low-energy in-plane acoustic LA and TA phonons carry ~ 99% of the heat, while optic phonons together with out-of-plane acoustic ZA phonons carry less than 1% of the total heat energy. The same result is obtained for two-layer AA graphene, three-layer ABA and ABC graphene. Comparing the obtained results with the same data for single-layer graphene, it can be concluded that polarization-dependent behavior of heat transport in graphene is practically insensitive to the number of layers and stacking geometry. It means that phonons of the same polarization together carry an almost constant portion of the heat with respect to its total amount. However, the absolute value of the thermal conductivity strongly depends on the number of layers, as well as their width, quality of the boundaries and temperature.

In Figure 4.14 is shown the temperature dependence of thermal conductivity in single-layer graphene, AB two-layer graphene and ABA three-layer graphene for two different layer widths: $d$ = 1 and 10 μm. All calculations were performed for a fixed value of specular parameter $p$ = 0.9.

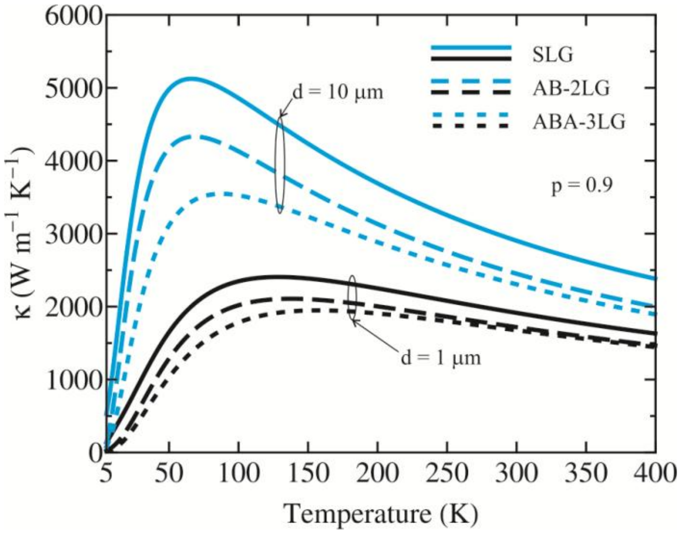

Fig. 4.14. Phonon thermal conductivity of single-layer graphene, two-layer AB graphene and three-layer ABA graphene as a function of temperature for different layers width.

One can see from the figure that with increasing of the number of layers the thermal conductivity decreases in the whole considered temperature range and for different layers width. The reason of this reduction can be understood from the following picture. There are two major factors that determine the dependence of the thermal conductivity on the layer number, these are: (i) number of heat carrying phonons and (ii) value of the $\frac{1}{h}$ term in the equation for the thermal conductivity (see equation (4.10)). Here $h$ is the thickness of the graphene flake. The total thickness of the graphene multilayer increases directly proportional to the number of layers, e.g. the three-layer graphene is three times thicker than the monolayer graphene. Although the dependence of the total number of phonon branches on the number of layers is analogous (e.g. there are three times more phonon branches in three-layer graphene than in monolayer), the number of heat carrying phonons is different. The translational symmetry of the graphene lattice imposes that the number of zone-center in-plane phonons with zero energy (denoted as $TA_1$ and $LA_1$ in Figure 4.13) equals to 2 and does not depend on the number of layers. The additional (quantified) $TA_2$/$LA_2$, $TA_3$/$LA_3$, etc., phonons of multi-layer graphene have an almost zero group velocity in the direct vicinity of the BZ center and thus are practically excluded from the heat transfer. However, in-plane acoustic phonons of the same polarization but farther from the zone-center have almost the same group velocity and contribute equally to the heat transport. When number of layer increases, the above mentioned mechanisms act opposite to one another, with a more stronger influence of the mechanism (ii) in comparison with mechanism (i), resulting in an overall decrease of the thermal conductivity. Moreover, the calculations suggest that this picture takes place regardless of the stacking geometry.

## 4.3. Twisted two-layer graphene. Engineering phonons with atomic plane rotations

In recent years the interest of the physics community has been shifting toward investigation of the T-FLG systems. When two graphene layers are placed on top of each other they can form a Moiré pattern [108, 178, 190]. In this case, one layer is rotated relative to another layer by a specific angle. The synthesis of T-FLG was experimentally demonstrated using the chemical vapor deposition, mechanical exfoliation or growth on the carbon terminated SiC surface [178, 191-193]. Although twisting only weakly affects the interlayer interaction, it breaks symmetry of the Bernal stacking resulting in an intriguing dependence of the electronic and phonon properties on the rotation angle (RA).

The electronic structure of the T-BLG with relatively small RAs was theoretically studied using both the continuum approach [108] and the density functional theory [194-195]. Experimentally, the specifics of the electronic transport in T-FLG were investigated using the surface X-ray diffraction [191], scanning tunneling microscopy [191-192] and Raman spectroscopy [190]. It was observed that twisted multilayer graphene grown on the carbon terminated face of 4H-SiC reveals single-layer graphene electronic properties [191]. More recently, this observation was confirmed by an independent Raman spectroscopy study [190]. While the electronic properties of T-FLG have been intensively investigated both theoretically and experimentally the phonon properties of T-FLG remain largely unexplored. Therefore, there is a strong need for an accurate theory and computation of the phonon energy, dispersion and DOS in T-BLG for the purpose of interpretation of experimental data.

Let us consider a bilayer graphene structure with a relative rotation angle $\theta$ between parallel graphene sheets and let us define the initial stacking configuration with $\theta = 0°$ as AB stacking. If one rotates one atomic layer of carbon atoms relative to another layer by an angle $\theta$ one will obtain a twisted graphene, as shown for example in Figure 4.15(a). Due to hexagonal symmetry the chosen scheme limits our consideration to rotational angles between $\theta = 0°$ and $\theta = 60°$, which corresponds to AA stacking configuration.

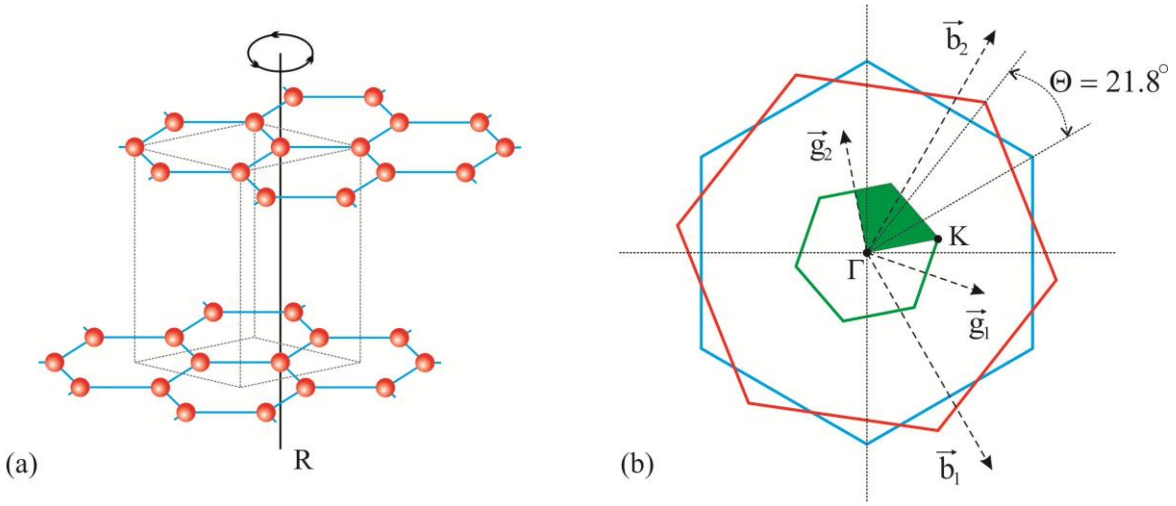

Fig. 4.15. (a) Rotational scheme. Note that rotational axis R passes through atoms which lie exactly above each other. (b) BZ of T-BLG with $\theta = 21.8°$. $\Gamma$ and $\mathrm{K}$ denote two high-symmetry points of T-BLG BZ.

Commensurate structures, i.e. structures with translation symmetry, exist for a certain rotational angles only, determined by the following condition: $\cos\theta(p,n) = (3p^2 + 3pn + n^2/2)/(3p^2 + 3pn + n^2)$, where $p$ and $n$ are coprime positive integer numbers. The basis vectors of Bravais lattice $\vec{t}_1$ and $\vec{t}_2$ for the commensurate T-BLG are given by the expression:

$$\begin{pmatrix} \vec{t}_1 \\ \vec{t}_2 \end{pmatrix} = \begin{pmatrix} p & p+n \\ -(p+n) & 2p+n \end{pmatrix} \begin{pmatrix} \vec{a}_1 \\ \vec{a}_2 \end{pmatrix}, \tag{4.11}$$

where $\vec{a}_1 = (3a/2, -\sqrt{3}a/2)$ and $\vec{a}_2 = (3a/2, \sqrt{3}a/2)$ are the basis vectors of Bravais lattice for the single-layer graphene, $a$=0.142 nm is the carbon-carbon bond length. The number of atoms in the commensurate cell is equal to the ratio between the volumes of the rotated and unrotated cells multiplied by a number of atoms in the unrotated cell:

$$N = 4\frac{\left|\left[\vec{t}_1 \times \vec{t}_2\right] \cdot \vec{z}\right|}{\left|\left[\vec{a}_1 \times \vec{a}_2\right] \cdot \vec{z}\right|}, \tag{4.12}$$

where $\vec{z}$ is the unitary vector normal to the graphene plane. Substituting equations (4.11) into equation (4.12) one can obtain for $N$:

$$N = 4\left(\left(p+n\right)^2 + p\left(2p+n\right)\right). \tag{4.13}$$

The unit cells of T-BLG with larger indices ($p$,$n$) contain larger number of carbon atoms. For instance, the unit cell of T-BLG with $\theta(1,1) = 21.8°$ contains the smallest possible number of atoms $N$ = 28, while a rotation by $\theta(2,1) = 13.2°$ increases this number to $N$ = 76.

In order to construct the BZ of the T-BLG with the angle of rotation $\theta(p,n)$ one should determine the corresponding reciprocal space. The reciprocal vectors of T-BLG $\vec{g}_1$ and $\vec{g}_2$ are related to the real space vectors $\vec{t}_1$ and $\vec{t}_2$ as: $\vec{g}_1 = 2\pi \frac{\left[\vec{t}_2 \times \vec{z}\right]}{\left|\left[\vec{t}_1 \times \vec{t}_2\right] \cdot \vec{z}\right|}$ ; $\vec{g}_2 = 2\pi \frac{\left[\vec{z} \times \vec{t}_1\right]}{\left|\left[\vec{t}_1 \times \vec{t}_2\right] \cdot \vec{z}\right|}$. Using these relations and equations (4.11) one can obtain:

$$\begin{pmatrix} \vec{g}_1 \\ \vec{g}_2 \end{pmatrix} = \frac{1}{(p+n)^2 + p(2p+n)} \times \begin{pmatrix} 2p+n & p+n \\ -(p+n) & p \end{pmatrix} \begin{pmatrix} \vec{b}_1 \\ \vec{b}_2 \end{pmatrix}, \tag{4.14}$$

where $\vec{b}_1 = (2\pi/3a, -2\pi/\sqrt{3}a)$ and $\vec{b}_2 = (2\pi/3a, 2\pi/\sqrt{3}a)$ are the basis vectors of the reciprocal lattice of the single layer graphene. The BZ of the T-BLG with $\theta(1,1) = 21.8°$ is shown in Figure 4.15(b) as a green hexagon.

In the case of the intralayer coupling the hexagonal symmetry of the interatomic interaction is preserved for different $\theta$, while in the interlayer coupling, the atomic configuration and force constant matrices are dependent on the rotational angle. In this case, one can describe the interlayer interactions with the Lennard-Jones potential $V(r) = 4\varepsilon\left((\sigma/r)^{12} - (\sigma/r)^6\right)$. The parameters $\varepsilon$ = 4.6 meV and $\sigma$ = 0.3276 nm were taken from Ref. [196]. They reproduce the experimental values of the interlayer space and phonon dispersion along the $\Gamma - \mathrm{A}$ direction of bulk graphite. Thus, the force constant matrix of interlayer interaction is:

$$\Phi^{ij}_{\alpha\beta}(n;\theta) = -\delta(r(\theta)) \times \frac{r_\alpha(n;\theta) r_\beta(n;\theta)}{\left|\vec{r}(n;\theta)\right|^2}, \tag{4.15}$$

where $\delta(r(\theta)) = 4\varepsilon\left(\frac{156\sigma^{12}}{r^{14}(\theta)} - \frac{42\sigma^6}{r^8(\theta)}\right)$ is the force constant of the interlayer coupling, $r(\theta)$ is the distance between the interacting atoms from a given atomic configuration corresponding to angle $\theta$.

The phonon dispersions in T-BLG with the rotation angles $\theta = 21.8°$ and $\theta = 13.2°$ are shown in Figure 4.16(a-b) along *Γ-K* direction in BZ. The phonon frequencies were calculated from equations (4.3) for each phonon wave number $q$ from the interval 0 to $q_{\max}(\theta)$, where $q_{\max}(\theta) = 2q_{\max}(\theta = 0)\sin(\theta/2) = 8\pi\sin(\theta/2)/(3\sqrt{3}a)$.

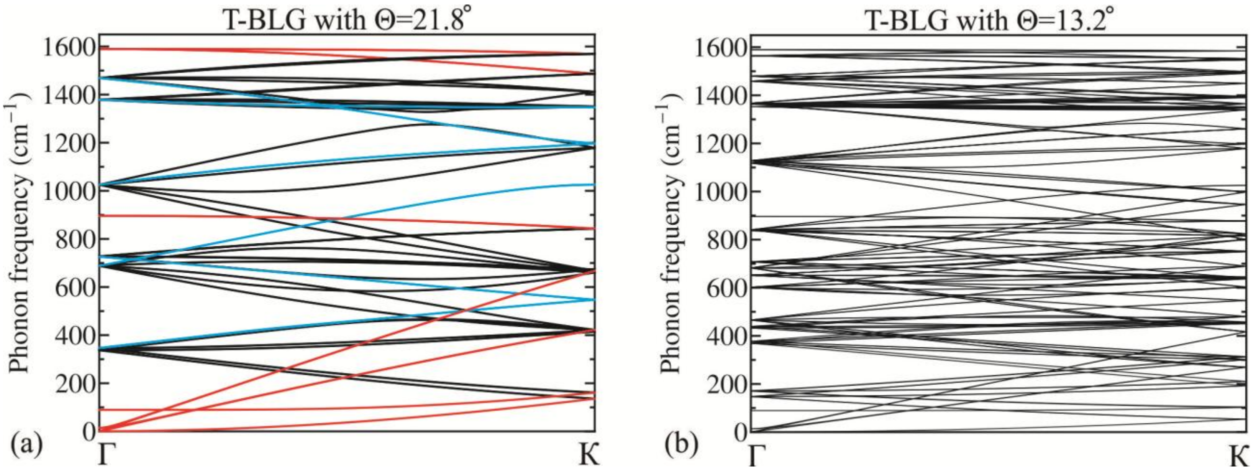

Fig. 4.16. Phonon energy dispersions in twisted bilayer graphene with $\theta = 21.8°$ (a) and $\theta = 13.2°$ (b).

The directions in BZ of T-BLG depend strongly on the rotational angle and do not coincide with the directions in BZ of bilayer graphene without a twist (BLG). As shown in Figure 4.15 (b), the $\Gamma$-$K$ direction in BZ of T-BLG is rotated relative to that in BZ of BLG. Therefore, the phonon curves in Figure 4.16(a-b) are shown for different directions in BZ of BLG. However, the $\Gamma$- and $K$-points in BZ of T-BLG correspond to those in BZ of BLG and the change of the phonon modes in these points is a direct effect of the twisting. The number of atoms in the unit cell of T-BLG with $\theta = 21.8°$ ($\theta = 13.2°$) increases by a factor of 7 (19) as compared with BLG. The number of phonon branches increases to 84 for T-BLG with $\theta = 21.8°$ and to 228 for T-BLG with $\theta = 13.2°$. The number of phonon modes at $\Gamma$- and $K$-points in BZ of T-BLG increases correspondingly. In addition to the degenerate TO/LO phonon modes of BLG at $\Gamma$-point with the frequency $\omega \sim 1589.5$ cm$^{-1}$, the new in-plane phonon modes appear in T-BLG. The frequencies of these modes depend strongly on the rotational angle and their number increases with decreasing $\theta$. In T-BLG with $\theta = 21.8°$, there appear additional phonon modes at the $\Gamma$-point related to the in-plane optical phonons with the frequencies $\omega \sim 1378.6$ cm$^{-1}$, 1468.8 cm$^{-1}$ and 1589.5 cm$^{-1}$. In T-BLG with $\theta = 13.2°$ one can observe new phonon modes with six different frequencies: $\omega \sim 1353.0$ cm$^{-1}$, 1363.1 cm$^{-1}$, 1367.2 cm$^{-1}$, 1458.8 cm$^{-1}$, 1479.3 cm$^{-1}$ and 1564.1 cm$^{-1}$. Analogously, at $K$-point of BZ instead of the in-plane phonon modes with $\omega \sim 1197.3$ cm$^{-1}$ and 1347.4 cm$^{-1}$, which are observed in BLG, one finds the phonon modes with the frequencies $\omega \sim 1197.4$ cm$^{-1}$, 1347.4 cm$^{-1}$, 1350.7 cm$^{-1}$, 1411.6 cm$^{-1}$, 1486.8 cm$^{-1}$ and 1569 cm$^{-1}$ in T-BLG with $\theta = 21.8°$. In T-BLG with $\theta = 13.2°$ the number of different frequencies of $K$-point phonons rises to 14: $\omega \sim 1197.4$ cm$^{-1}$, 1260.5 cm$^{-1}$, 1339.8 cm$^{-1}$, 1347.4 cm$^{-1}$, 1351.4 cm$^{-1}$, 1365.2 cm$^{-1}$, 1390.4 cm$^{-1}$, 1395.6 cm$^{-1}$, 1449.6 cm$^{-1}$, 1491.5 cm$^{-1}$, 1498.2 cm$^{-1}$, 1547.3 cm$^{-1}$, 1552.8 cm$^{-1}$ and 1584.7 cm$^{-1}$. Overall the phonon spectrum of twisted bilayer graphene becomes much more complicated.

The twisting influences the phonon spectra of BLG owing to two reasons: (i) modification of the weak van der Waals interlayer interaction and (ii) alteration of a size of a BZ leading to the phonon momentum change. To investigate these effects separately in Figure 4.17(a-b) it is plotted the phonon dispersions in AA-BLG along $\Gamma_0$-$K_0$ (red curves) and $\Gamma_1$-$K_1$ (blue curves) direction in BZ of AA-BLG.

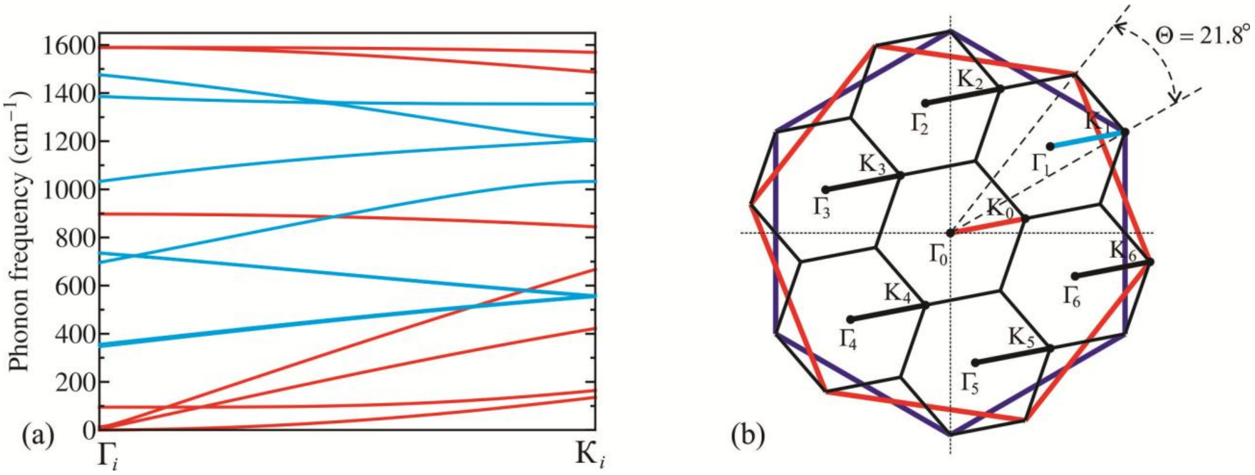

Fig. 4.17. Phonon energy dispersions in AA-stacked bilayer graphene shown for $\Gamma_0$-$K_0$ and $\Gamma_1$-$K_1$ (a) directions of the BZ of AA-BLG. (b) BZs in AA-BLG and T-BLG with $\theta = 21.8^\circ$.

In BZ of AA-BLG there are seven directions $\Gamma_i$-$K_i$ (i = 0,...,6) which are equivalent to the direction $\Gamma_0$-$K_0$ in BZ of T-BLG (see Figure 4.15(b), where the BZs for the BLG and T-BLG are shown). The phonon dispersion in T-BLG with $\theta = 21.8^\circ$, shown in Figure 4.16(a), corresponds to the phonon dispersions along $\Gamma_i$-$K_i$ (i = 0,...,6) directions in BZ of AA-BLG. Thus, in the twisted bilayer graphene appear hybrid folded phonon branches resulting from mixing of different directions from BLG BZ: $\Gamma_0$-$K_0$, $\Gamma_1$-$K_1$, .., $\Gamma_6$-$K_6$. The red and blue curves in Figure 4.16(a) appear in the phonon spectra of T-BLG from $\Gamma_0$-$K_0$ and $\Gamma_1$-$K_1$ direction in BZ of AA-BLG. The difference in the frequencies of the phonon modes shown in Figures 4.16(a) (red and blue curves) and Figure 4.17(a-b) is a manifestation of the twisting. In T-BLG the difference between the phonon frequencies of all corresponding modes is small due to weak interlayer interaction.

The frequencies of the shear (LA$_2$, TA$_2$) and flexural (ZA$_2$) phonons are affected stronger by the twisting. The specific properties of these modes in T-BLG with $\theta = 21.8^\circ$ (red curves) and T-BLG with $\theta = 13.2^\circ$ (blue curves) as well as in AA-BLG (black curves) are presented in Figure 4.18.

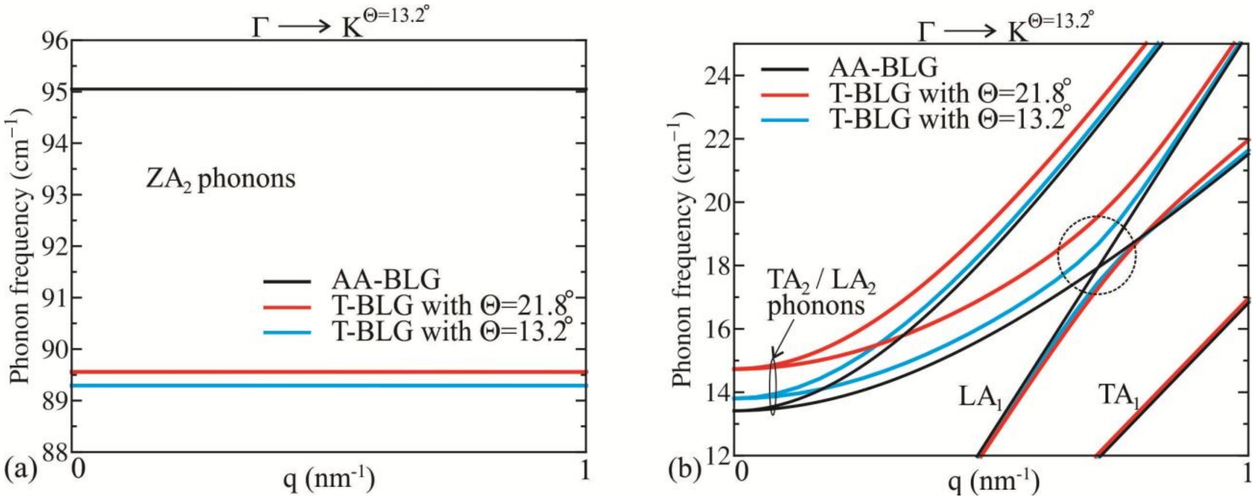

Fig. 4.18. Zone-center phonon dispersions of the out-of-plane (a) and in-plane (b) acoustic modes in AA-BLG (black curves), T-BLG with $\theta = 21.8°$ (red curves) and T-BLG with $\theta = 13.2°$ (blue curves). The region where anti-crossing of LA$_1$ and TA$_2$ hybrid folded phonon branches occurs are shown by dashed circle.

At $\Gamma$ – point, the twisting increases the frequency of the shear modes by 1 – 2 cm$^{-1}$ and decreases the frequency of ZA$_2$ modes by ~ 5 – 5.5 cm$^{-1}$ depending on $\theta$ (see Figure 4.18(a)). In AA-BLG, the phonon branches LA$_1$ and TA$_2$ intersect at $q$ ~ 0.7 nm$^{-1}$. Twisting changes the interaction between these phonons in T-BLG and leads to anti-crossing of LA$_1$ and TA$_2$ hybrid folded phonon branches (see Figure 4.18(b)).

Specific heat, $C$, is one of the key parameters that characterize the phonon and thermal properties of materials. It is defined as $C = \delta Q / \delta T$, where $\delta Q$ is the change in energy density of a material when temperature changes by $\delta T$ [122]. For calculation of the phonon specific heat in T-BLG it is used the following formula [122, 189]:

$$c_V(T) = \frac{3N_A}{k_B T^2} \int_0^{\omega_{\max}} \frac{\exp(\frac{\hbar\omega}{k_B T})}{[\exp(\frac{\hbar\omega}{k_B T}) - 1]^2} (\hbar\omega)^2 f(\omega) d\omega, \tag{4.16}$$

where $\omega$ is the phonon frequency, $\omega_{\max}$ is the maximum phonon frequency, $f$ is the 2D normalized phonon DOS, $T$ is the temperature, $N_A$ is the Avogadro constant, $k_B$ is the Boltzmann constant and $\hbar$ is the Planck constant. The normalized phonon DOS is given by:

$$f(\omega) = g(\omega) \Big/ \int_0^{\omega_{\max}} g(\omega) d\omega, \tag{4.17}$$

where $g(\omega)$ is the 2D phonon DOS given by the relation:

$$g(\omega) = \int_{q_x} \sum_{s(\omega,q_x)} \sum_{q_y(s,\omega,q_x)} \left| \frac{\partial \omega(q_x, q_y, s)}{\partial q_y} \right|^{-1} dq_x \,. \tag{4.18}$$

Here *s* numerates phonon branches. In order to calculate $g(\omega)$ we applied a 200×200 2D grid to a 1/4th part of BZ of T-BLG (shown as a green segment in Figure 4.15(b)), and then calculated phonon frequencies for every ($q_x$,$q_y$) point in this grid.

The dependence of specific heat on temperature for single-layer graphene and AB-BLG is presented in Figure 4.19(a). The experimental values of graphite heat capacity reported in Ref. [197] are also shown for comparison by the blue triangles.

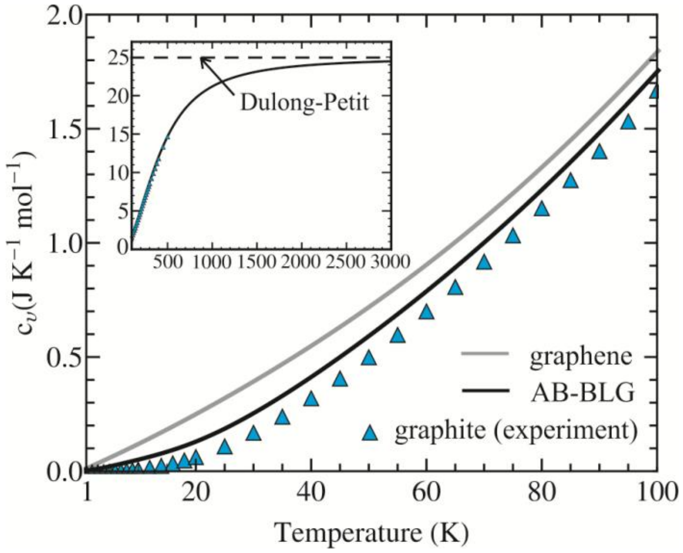

Fig. 4.19. Dependence of the specific heat at constant volume on temperature in single-layer graphene (gray curve) and AB-BLG (black curve). The blue triangles represent the experimental results for graphite, reported in Ref. [197]. The inset shows the results plotted for a wide temperature range 100 K – 3000 K.

The low-temperature heat capacity of single-layer graphene is higher than that in graphite due to inequality of 2D and 3D phonon DOS. The difference in the heat capacity of single-layer graphene, BLG and graphite diminishes with temperature rise. The heat capacities become identical within 0.01% deviation for $T > 2000$ K. At temperatures $T > 2500$ K, all heat capacities approach the classical Dulong-Petit limit $c_V = 24.94$ J K$^{-1}$ mol$^{-1}$. At small frequencies, ZA phonons demonstrate a quadratic dispersion $\omega \sim q^2$, leading to $c_V(ZA) \sim T$, while TA and LA phonons possess linear dispersions $\omega \sim q$, resulting in $c_V(LA,TA) \sim T^2$. We found that total heat capacity in single-layer graphene varies with temperature as $T^n$, where $n = 1$ for $T \leq 15$ K; $n = 1.1$ for 15 K $< T \leq 35$ K; $n = 1.3$ for 35 K $< T \leq 70$ K and $n = 1.5$ for 70 K $< T \leq 240$ K. The power factor *n* increases with temperature not only due to greater contribution of LA and TA phonons but also due to the deviation of ZA phonon frequency dispersion from the quadratic law, leading to nearly linear dependence of ZA DOS on frequency for $\omega > 100$ cm$^{-1}$. Our results for heat capacity in single-layer graphene are qualitatively similar to those described in Refs. [198-199] with the exception of the power factor values $n = 1$ [198] and $n = 1.1$ [199] for $T <$ 100 K. This discrepancy is explained by the fact that in Refs. [198-199] the authors did not take into account the non-parabolicity of ZA dispersion for $\omega > 100$ cm$^{-1}$. In AA-BLG or AB-BLG $c_V \sim T^{1.6}$ for wide temperature range $T \leq 170$ K due to the changes in DOS in comparison with those in single-layer graphene.

In Figure 4.20 we plot a difference between the specific heat in AB-BLG and T-BLG as a function of temperature: $\Delta c_v(\theta) = c_v(AB) - c_v(\theta)$ for $\theta = 21.8°$, $\theta = 13.2°$ and $\theta = 9.4°$.

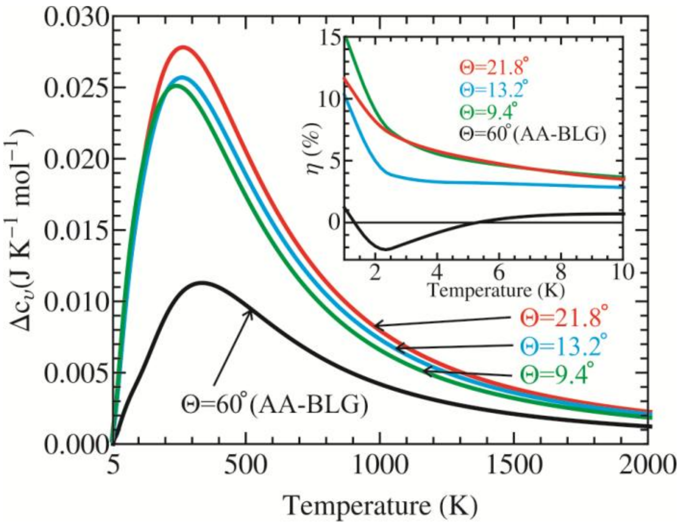

Fig. 4.20. Dependence of the deviation $\Delta c_v(\theta)$ of the specific heat in T-BLG from that in AB-BLG on the temperature. The inset shows the relative deviation $\eta$ between AB-BLG and T-BLG specific heats as a function of temperature.

The change in the specific heat due to twisting is relatively weak in a wide temperature range 20 K - 2000 K. It attains its maximum value ~ 0.028 J K$^{-1}$ mol$^{-1}$ at $T \sim 250$ K. At the same time, at low temperatures the relative difference between specific heat in AB-BLG and T-BLG $\eta = (1 - c_V(\theta)/c_V(AB)) \times 100\%$ constitutes substantial 10-15% at $T = 1$ K and ~ 3-6% at $T = 5$ K in dependence on $\theta$ (see blue, red and green curves from the inset to Figure 4.20). The low temperatures specific heat depends stronger on the twist angle because twisting affects the low-frequency ZA phonon modes the most [38]. A somewhat similar effect of modulation of the specific heat was recently reported for single-layer graphene under strain [104]. The authors found that a stronger modification of the specific heat occurs at temperatures below 1 K. The temperature dependence of low-temperature specific heat in T-BLG with $\theta = 21.8°$ differs from single-layer or bilayer graphene: $c_V \sim T^{1.3}$ for T < 10 K and $\sim T^{1.6}$ for 10 K $\leq T \leq$ 100 K. One should expect that twisting can produce stronger effects on the specific heat of the T-FLG with the larger number of the atomic planes rotated with respect to each other as well as in van der Waals materials with stronger interlayer coupling. The results suggest a possibility of phonon engineering of phonon and thermal properties of layered materials by twisting the atomic planes.

### 4.4. Conclusions to chapter 4

The main scientific results of this chapter are:

- A BvK model of lattice dynamics for single-, two-layer and three-layer graphene as well as for twisted bilayer graphene with different angles of rotation was developed.
- Phonon energy spectra of these structures in all high-symmetry crystallographic directions were calculated. The obtained results for phonon frequencies of single-layer and non-rotated few-layer graphene are in a very good agreement with experimental data of bulk graphite.
- It was found that, since many of the zone-center acoustic and optical vibrational modes of non-rotated few-layer graphene are Raman or infrared active, they can provide important information on layer number and stacking configuration of graphene multilayers.
- It was found that middle- and high-frequency phonons in twisted bilayer graphene are practically independent on the twisting angle, while the low-frequency phonons strongly depend on it.
- A phonon mode-specific contribution to the thermal transport of single-, two- and three-layer graphene was established, suggesting that high-velocity in-plane acoustic LA and TA phonons are the main heat carriers in these structures.
- It was demonstrated, that in single- and non-rotated few-layer graphene umklapp and boundary scattering are the dominant scattering mechanisms, limiting correspondingly its thermal conductivity in a wide range of temperatures and layer widths.
- It was found, that in non-rotated few-layer graphene phonons of the same polarization together carry an almost constant portion of the heat with respect to its total amount, irrespective to the number of layers and stacking geometry.
- It was shown that a new type of hybrid folded rotationally-dependent phonon modes appear in the twisted bilayer graphene due to reduction of the BZ size and changes in the interaction between graphene layers. These modes can manifest themselves in Raman or

infrared measurements and, thus, can be used for the non-contact characterization of twisted bilayer graphene.

- The phonon specific heat in single-layer, bilayer and twisted bilayer graphene was studied. It was found that at temperature $T$<15 K, specific heat varies with temperature as $T^n$, where $n$ = 1 for graphene, $n$ = 1.6 for bilayer graphene and $n$ = 1.3 for the twisted bilayer graphene.

All numerical simulations presented in this chapter were carried out entirely by the author, while theoretical derivations and data analysis was done in close collaboration and under supervision of scientifc advisor. The results of the investigation of the phonon processes in graphene and twisted bilayer graphene were published in the research articles [38, 44, 196, 200].

# GENERAL CONCLUSIONS AND RECOMMENDATIONS

Below the summary of the results obtained in the Thesis is given.

1. A three-parameter Born-von Karman type model of lattice dynamics for nanolayers and planar superlattices with diamond crystal lattice was developed. The Boltzmann transport equation approach was used for investigation of the phonon and thermal processes in Si nanolayers and Si/Ge planar superlattices. For nanometer-wide silicon nanolayers was obtained a good agreement between theoretical calculations and the experimental data for 20-nm-thick and 30-nm-thick silicon nanolayers. It was demonstrated that optical phonons contribution to the thermal conductivity of silicon nanolayers under consideration constitutes only a few percent.
2. The perturbation theory and second quantization formalism were used in order to model the scattering of phonons on interfaces in Si/Ge planar superlattices. It was concluded that interface mass-mixing scattering of phonons plays an extremely important role in limiting the total phonon lifetime in Si/Ge planar superlattices and can lead to a peculiar behavior of phonon thermal conductivity of these structures owing to the non-trivial dependence of interface scattering rate on the amplitudes of the atomic displacements. For a wide temperature range from 50 K to 400 K a good agreement between theoretical and experimental phonon thermal conductivity was obtained for Si(35ML)/Ge(9ML) planar superlattice when phonon-phonon scattering was not taken into account, indicating that the interface mass-mixing scattering can be the dominant mechanism of phonon scattering in real Si/Ge planar superlattices.
3. The effective mass method was applied for investigation of electron energy spectra and electron wave functions in core/shell Si/$SiO_2$ nanowires with constant and periodically modulated cross-section. It was shown, that cross-section modulation strongly influences the electron energy spectra and electron wave functions in Si nanowires. For ground state there appear an inhomogeneity in the wave function distribution along the wire's axis, namely, the main part of the wave function modulus being localized in the wide segments of the modulated wire.
4. The lattice dynamics Born – von Karman model and the Boltzmann transport equation were applied for investigation of phonon and thermal processes in Si nanowires, Si cross-section modulated nanowires and Si/Ge core/shell cross-section modulated nanowires. For Si cross-section modulated nanowires it was theoretically demonstrated that phonon heat flux can be significantly suppressed in comparison with the generic uniform cross-section Si nanowires. Redistribution of the phonon energy spectra in the cross-section modulated nanowires leads to a strong decrease of the average phonon group velocities and a corresponding suppression of the phonon thermal flux. An up to 5 times drop of the phonon heat flux at room temperature is

predicted for Si cross-section modulated nanowires in comparison with uniform Si nanowires. For Si/Ge core/shell cross-section modulated nanowires it was found theoretically that a combination of cross-section modulation and acoustic mismatch between Si and Ge materials can lead to an even more drastic reduction of the thermal conductivity. The performed calculations indicate that the room temperature thermal conductivity of Si/Ge core/shell cross-section modulated nanowires is almost three orders of magnitude lower than that of bulk Si.

5. The analytical expression for the electron-phonon scattering rate with emission and absorption of a phonon in Si/$SiO_2$ core/shell modulated nanowires was derived in the deformation potential approach. It was shown that cross-section modulation of the Si core results in a substantial modification of the room temperature electron-phonon scattering rate with phonon absorption.

6. A Born – von Karman model of lattice dynamics for single-, two-layer and three-layer graphene as well as for twisted bilayer graphene with different angles of rotation was developed. Phonon energy spectra of these structures in all high-symmetry crystallographic directions were calculated. The obtained results for phonon frequencies of single-layer and non-rotated few-layer graphene are in a very good agreement with experimental data of bulk graphite. It was found that, since many of the zone-center acoustic and optical vibrational modes of non-rotated few-layer graphene are Raman or infrared active, they can provide important information on layer number and stacking configuration of graphene multilayers. It was found that middle- and high-frequency phonons in twisted bilayer graphene are practically independent on the twisting angle, while the low-frequency phonons strongly depend on it. Thus, *an important scientific problem was solved* in the Thesis namely it was demonstrated the possibility to control the phonon processes in two-layer graphene by rotation of graphene layers one against another around the axis perpendicular to the graphene plane.

7. It was shown that a new type of hybrid folded rotationally-dependent phonon modes appear in the twisted bilayer graphene due to reduction of the BZ size and changes in the interaction between graphene layers. These modes can manifest themselves in Raman or infrared measurements and, thus, can be used for the non-contact characterization of twisted bilayer graphene. The phonon specific heat in single-layer, bilayer and twisted bilayer graphene was studied. It was found that at temperature $T<15$ K, specific heat varies with temperature as $T^n$, where $n = 1$ for graphene, $n = 1.6$ for bilayer graphene and $n = 1.3$ for the twisted bilayer graphene.

Based on the conclusions presented above, the following recommendations can be made:

1. The Si/Ge planar superlattices with atomic intermixing at interfaces are perspective candidates for phonon filtering applications.

2. The acoustically-mismatched Si-based core/shell modulated nanowires with suppressed phonon heat transport are perspective for thermoelectric and thermal insulator applications.
3. The twisted bilayer graphene with different angles of rotation can be recommended for heat spreading and heat management applications owing to their unusual angle-dependent phonon processes.

The obtained theoretical results contribute to a better understanding of the electron and phonon processes in graphene and silicon-based nanostructures and are important for the design and practical realization of novel nanomaterials with optimized and properly engineered electron and phonon properties.

# REFERENCES

[1] Haug H. and Koch S.W. Quantum Theory of the Optical and Electronic Properties of Semiconductors. World Scientific, 1994. 473 p.

[2] Cahay M. Quantum Confinement VI: Nanostructured Materials and Devices: Proceedings of the International Symposium. The Electrochemical Society, 2001. 398 p.

[3] Slater J. C. and Koster G. F. Simplified LCAO Method for the Periodic Potential Problem. In: Phys. Rev., 2004, vol. 94, p. 1498–1524.

[4] Vogl P., Hjalmarson H. P. and Dow J. D. A Semi-empirical tight-binding theory of the electronic structure of semiconductors. In: J. Phys. Chem. Solids, 1983, vol. 44, p. 365–378.

[5] Jancu J. M. et.al. Empirical spds* tight-binding calculation for cubic semiconductors: General method and material parameters. In: Phys. Rev. B, 1998, vol. 57, p. 6493–6507.

[6] Boykin T. B., Klimeck G. and Oyafuso F. Valence band effective-mass expressions in the $sp^3d^5s^*$ empirical tight-binding model applied to a Si and Ge parameterization. In: Phys. Rev. B, 2004, vol. 69, 115201.

[7] Luisier M. et.al. Atomistic simulation of nanowires in the $sp^3d^5s^*$ tight-binding formalism: From boundary conditions to strain calculations. In: Phys. Rev. B, 2006, vol. 74, 205323.

[8] Klimeck G. et.al. Development of a Nanoelectronic 3-D (NEMO 3-D) Simulator for Multimillion Atom Simulations and Its Application to Alloyed Quantum Dots. In: Computer Modeling in Engineering and Science (CMES), 2002, vol. 3, p. 601–642.

[9] Klimeck G. et.al. Si tight-binding parameters from genetic algorithm fitting. In: Superlattices and Microstructures, 2000, vol. 27, p. 77–88.

[10] Boykin T. B. et.al. Strain-induced, off-diagonal, same-atom parameters in empirical tight-binding theory suitable for [110] uniaxial strain applied to a silicon parameterization. In: Phys. Rev. B, 2010, vol. 81, p. 125202.

[11] Martin M. Electronic Structure: Basic Theory and Practical Methods. Cambridge University Press, 2008. 647 p.

[12] von Barth U. Basic Density-Functional Theory – an Overview. In: Phys. Scr., 2004, vol. 9, T109.

[13] Capelle K. A bird’s-eye view of density-functional theory. In: Braz. J. Phys., 2006, vol. 36, no. 4a.

[14] Jones R. O. Introduction to density functional theory and exchange correlation energy functionals. In: Computational Nanoscience, 2006, vol. 31, p. 45-70.

[15] Cui Y. et.al. High Performance Silicon Nanowire Field Effect Transistors. In: Nano Lett., 2003, vol. 3, p. 149.

[16] Koo S. et.al. Enhanced Channel Modulation in Dual-Gated Silicon Nanowire Transistors. In: Nano Lett., 2005, vol. 5, p. 2519.

[17] Goldberger J. et.al. Silicon Vertically Integrated Nanowire Field Effect Transistor. In: Nano Lett., 2006, vol. 6, p. 973.

[18] Xiang J. et.al. Ge/Si Nanowire Heterostructures as High-performance Field-Effect Transistors. In: Nature Letters, 2006, vol. 441, p. 489.

[19] Han G. et.al. Silicon-based tunneling field-effect transistor with elevated germanium source formed on (110) silicon substrate. In: Appl. Phys. Lett., 2011, vol. 98, p. 153502.

[20] Hamid F. et.al. The effect of effective channel length on a silicon nanowire fin field effect transistor. In: J. Comput. Theor. Nanosci., 2013, vol. 10, p. 964.

[21] Barbagiovanni E. G. et.al. Quantum confinement in Si and Ge nanostructures. In: J. Appl. Phys., 2012, vol. 111, p. 034307.

[22] Nolan M. et.al. Silicon nanowire band gap modification. In: Nano Lett., 2007, vol. 7, p. 34.

[23] Santiago-Perez D. et.al. Electron-phonon deformation potential interaction in core-shell Ge-Si and Si-Ge nanowires. In: arXiv:1409.7314v2, 2014, http://arxiv.org/abs/1409.7314v2.

[24] Shchepetov A. et.al. Ultra-thin free-standing single crystalline membranes with strain control. In: Appl. Phys. Lett., 2013, vol. 102, p. 192108.

[25] Boykin T. B. et.al. Valley splitting in strained silicon quantum wells. In: Appl. Phys. Lett., 2004, vol. 84, p. 115.

[26] Perim E. et.al. One-dimensional silicon and germanium nanostructures with no carbon analogues. In: Phys. Chem. Chem. Phys., 2014, vol. 16, p. 24570.

[27] Healy N. et.al. Extreme electronic bandgap modification in laser-crystallized silicon optical fibers. In: Nature Materials, 2014, vol. 13, p. 1122.

[28] Debye P. The theory of specific heats. In: Ann. Phys. (Lpz.), 1912, vol. 39, p. 789.

[29] Born M. and Karman Th. Über Schwingungen in Raumgittern (On fluctuations in spatial grids). In: Physikalische Zeitschrift, 1912, vol. 13, p. 297-309.

[30] Born M. Dynamik der Krystallgitter (Dynamics of Crystal Lattices). Teubner: Leipzig, 1915. 122 p.

[31] Stroscio M. and Dutta M. Phonons in nanostructures. Cambridge University Press, 2001. 282 p.

[32] Pokatilov E., Nika D. and Balandin A. Acoustic-phonon propagation in rectangular semiconductor nanowires with elastically dissimilar barriers. In: Phys. Rev. B, 2005, vol. 72, 113311.

[33] Nika D., Zincenco N. and Pokatilov E. Lattice thermal conductivity of ultra-thin freestanding layers: Face-centered cubic cell model versus continuum approach. In: J. Nanolectron. Optoelectron., 2009, vol. 4, p. 170-173.

[34] Born M. On the space lattice theory of diamond. In: Ann. Phys. (Lpz.), 1914, vol. 44, p. 605.

[35] Born M. and Huang K. Dynamical Theory of Crystal Lattices. Oxford University Press, 1954. 293 p.

[36] Cocemasov A. and Nika D. Phonons and phonon thermal conductivity in silicon nanolayers. In: J. Nanoelectron. Optoelectron., 2012, vol. 7, p. 370-375.

[37] Nika D. et.al. Suppression of phonon heat conduction in cross-section-modulated nanowires. In: Phys. Rev. B, 2012, vol. 85, 205439.

[38] Cocemasov A., Nika D. and Balandin A. Phonons in twisted bilayer graphene. In: Phys. Rev. B, 2013, vol. 88, 035428.

[39] Musgrave M. and Pople J. General valence force field for diamond. In: Proc. R. Soc. A, 1962, vol. 268, p. 474.

[40] Weber W. Adiabatic bond charge model for phonons in diamond, Si, Ge, and α-Sn. In: Phys. Rev. B, 1977, vol. 15, p. 4789.

[41] Paul A., Luisier M. and Klimeck G. Modified valence force field approach for phonon dispersion: from zinc-blende bulk to nanowires. In: J. Comput. Electron., 2010, vol. 9, p. 160-172.

[42] Yip S. and Chang Y. Phonon dispersion relations in semiconductor superlattices in the adiabatic bond-charge model. In: Superlatt. Microstruct., 1985, vol. 1, p. 165-171.

[43] Cocemasov A. Lattice dynamics with empirical potentials (in russian). In: Studia Universitatis, Seria “Ştiinţe Exacte şi Economice”, 2012, nr.7 (57), p. 47-55.

[44] Cocemasov A. Force constant matrices from Keating interatomic potential: Application to graphene. In: Studia Universitatis Moldaviae, Seria “Ştiinţe Exacte şi Economice”, 2014, nr.2 (72), p. 78-83.

[45] Stillinger F. and Webber T. Computer simulation of local order in condensed phases of silicon. In: Phys. Rev. B, 1985, vol. 31, p. 5262-5271.

[46] Svizhenko A. et.al. Electron interaction with confined acoustic phonons in quantum wires subjected to a magnetic field. In: Phys. Rev. B, 1998, vol. 57, p. 4687.

[47] Vasko F. and Mitin V. Emission of transverse acoustic phonons by two-dimensional electrons due to heterointerface vibrations. In: Phys. Rev. B, 1995, vol. 52, p. 1500.

[48] Nishiguchi N. Electron scattering by surface vibration in a rectangular quantum wire. In: Physica E, 2002, vol. 13, no. 1, p. 1-10.

[49] Balandin A. Thermal properties of semiconductor low-dimensional structures. In: Phys. Low.-Dim. Structures, 2000, ½, 1.

[50] Zebarjadi M. et.al. Perspectives on thermoelectrics: from fundamentals to device applications. In: Energy Environ. Sci., 2012, vol. 5, p. 5147-5162.

[51] Cahill D. et.al. Nanoscale thermal transport. In: Applied Physics Reviews, 2014, vol. 1, p. 011305.

[52] Zhao L.-D. et.al. The panoscopic approach to high performance thermoelectrics. In: Energy Environ. Sci., 2014, vol. 7, p. 251-268.

[53] Li D. et.al. Thermal conductivity of individual silicon nanowires. In: Appl. Phys. Lett., 2003, vol. 83, p. 2934-2936.

[54] Hochbaum A. et.al. Enhanced thermoelectric performance of rough silicon nanowires. In: Nature, 2008, vol. 451, p. 163-167.

[55] Boukai A. et.al. Silicon nanowires as efficient thermoelectric materials. In: Nature, 2008, vol. 451, p. 168-171.

[56] Chang C. et.al. Breakdown of Fourier’s law in nanotube thermal conductors. In: Phys. Rev. Lett., 2008, vol. 101, 075903.

[57] Johnson J. et.al. Direct measurement of room-temperature nondiffusive thermal transport over micron distances in a silicon membrane. In: Phys. Rev. Lett., 2013, vol. 110, 025901.

[58] Poudel B. et.al. High-thermoelectric performance of nanostructured bismuth antimony telluride bulk alloys. In: Science, 2008, vol. 320, p. 634-638.

[59] Biswas K. et.al. High-performance bulk thermoelectrics with all-scale hierarchical architectures. In: Nature, 2012, vol. 489, p. 414-418.

[60] Chowdhury I. et.al. On-chip cooling by superlattice-based thin-film thermoelectrics. In: Nature Nanotechnology, 2009, vol. 4, p. 235-238.

[61] Chavez-Angel E. et.al. Reduction of the thermal conductivity in free-standing silicon nano-membranes investigated by non-invasive Raman thermometry. In: APL Materials, 2014, vol. 2, p. 012113.

[62] Cuffe J. et.al. Lifetimes of confined acoustic phonons in ultrathin silicon membranes. In: Phys. Rev. Lett., 2013, vol. 110, 095503.

[63] Daly B. et.al. Picosecond ultrasonic measurements of attenuation of longitudinal acoustic phonons in silicon. In: Phys. Rev. B, 2009, vol. 80, 174112.

[64] Bruchhausen A. et.al. Subharmonic resonant optical excitation of confined acoustic modes in a free-standing semiconductor membrane at GHz frequencies with a high-repitition-rate femtosecond laser. In: Phys. Rev. Lett., 2011, vol. 106, 077401.

[65] Hepplestone S. and Srivastava G. Phononic gaps in thin semiconductor superlattices. In: J. Appl. Phys., 2010, vol. 107, p. 043504.

[66] Luckyanova M. et.al. Coherent phonon heat conduction is superlattices. In: Science, 2012, vol. 338, p. 936.

[67] Dechaumphai E. and Chen R. Thermal transport in phononic crystals: The role of zone folding effect. In: J. Appl. Phys., 2012, vol. 111, p. 073508.

[68] Karamitaheri H., Neophytou N. and Kosina H. Anomalous diameter dependence of thermal transport in ultra-narrow Si nanowires. In: J. Appl. Phys., 2014, vol. 115, p. 024302.

[69] Xie G. et.al. Phonon surface scattering controlled length dependence of thermal conductivity of silicon nanowires. In: Phys. Chem. Chem. Phys., 2013, vol. 15, p. 14647.

[70] Maldovan M. Narrow low-frequency spectrum and heat management by thermocrystals. In: Phys. Rev. Lett., 2013, vol. 110, 025902.

[71] Maldovan M. Sound and heat revolutions in phononics. In: Nature, 2013, vol. 503, p. 209-217.

[72] Chang C. et al. Solid-state thermal rectifier. In: Science, 2006, vol. 314, p. 1121.

[73] Casati G. Device physics: The heat is on – and off. In: Nature Nanotech., 2007, vol. 2, p. 23.

[74] Chen J. et. al. Heat conduction in graphene flakes with inhomogeneous mass interface. In: J. Stat. Mech., 2011, P10031.

[75] Terraneo M. et. al. Controlling the energy flow in non-linear lattices: A model for a thermal rectifier. In: Phys. Rev. Lett., 2002, vol. 88, 094302.

[76] Lei W. and Li B. Thermal logic gates: Computation with phonons. In: Phys. Rev. Lett., 2007, vol. 99, 177208.

[77] Hu J. et. al. Thermal conductivity and thermal rectification in graphene nanoribbons: A molecular dynamics study. In: Nano Lett., 2009, vol. 9, p. 2730.

[78] Ouyang T. et. al. Ballistic thermal rectification in asymmetric three-terminal graphene nanojunctions. In: Phys. Rev. B, 2010, vol. 82, 245403.

[79] Yang N., Zhang G. and Li B. Thermal rectification in asymmetric graphene ribbons. In: Appl. Phys. Lett., 2009, vol. 95, p. 033107.

[80] Rajabpour A. et. Al. Study on the thermal resistance in secondary particles chain of silica aerogel by moldecular dynamics simulation. In: Appl. Phys. Lett., 2011, vol. 99, p. 051917.

[81] Zhang G. and Zhang H. Thermal conduction and rectification in few-layer graphene Y junctions. In: Nanoscale, 2011, vol. 3, p. 4604.

[82] Hu M., Keblinski P. and Li B. Thermal rectification at silicon-amorphous polyethylene interface, Appl. Phys. Lett., 2008, vol. 92, p. 211908.

[83] Li N. et.al. Phononics: Manipulating heat flow with electronic analogs and beyond. In: Rev. Mod. Phys., 2012, vol. 84, p. 1045-1066.

[84] Novoselov K. et.al. electric field effect in atomically thin carbon films. In: Science, 2004, vol. 306, p. 666.

[85] Novoselov K. et.al. Two-dimensional gas of massless Dirac fermions in graphene. In: Nature, 2005, vol. 438, p. 197.

[86] Balandin A. et. al. Superior thermal conductivity of single-layer graphene. In: Nano Letters, 2008, vol. 8, p. 902.

[87] Ghosh S. et. al. Extremely high thermal conductivity of graphene: Prospects for thermal management applications in nanoelectronic circuits. In: Appl. Phys. Lett., 2008, vol. 92, p. 151911.

[88] Nika D. et. al. Phonon thermal conduction in graphene: Role of Umklapp and edge roughness scattering. In: Phys. Rev. B, 2009, vol. 79, 155413.

[89] Nika D. et. al. Lattice thermal conductivity of graphene flakes: Comparison with bulk graphite. In: Appl. Phys. Lett., 2009, vol. 94, p. 203103.

[90] Lindsay L. et. al. Flexural phonons and thermal transport in graphene. In: Phys. Rev. B, 2010, vol. 82, 115427.

[91] Klemens P. Theory of the A-plane thermal conductivity of graphite. In: J. Wide Bandgap Mater., 2000, vol. 7, p. 332-339.

[92] Klemens P. Theory of thermal conduction in the ceramic films. In: Int. J. Thermophys., 2001, vol. 22, p. 265-275.

[93] Seol J. et. al. Two-dimensional phonon transport in supported graphene. In: Science, 2010, vol. 328, p. 213.

[94] Jang W. et. al. Thickness-dependent thermal conductivity of encased graphene and ultrathin graphite. In: Nano Letters, 2010, vol. 10, p. 3909.

[95] Ghosh S. et al. Dimensional crossover of thermal transport in few-layer graphene. In: Nature Materials, 2010, vol. 9, p. 555-558.

[96] Klemens P. and Pedraza D. Thermal conductivity of graphite in basal plane. In: Carbon, 1994, vol. 32, p. 735-741.

[97] Lindsay L., Broido D. and Mingo N. Diameter dependence of carbon nanotube thermal conductivity and extension to the graphene limit. In: Phys. Rev. B, 2010, vol. 82, 161402.

[98] Singh D., Murthy J. and Fisher T. Mechanism of thermal conductivity reduction in few-layer graphene. In: J. Appl. Phys., 2011, vol. 110, p. 044317.

[99] Qiu B. and Ruan X. Reduction of spectral phonon relaxation times from suspended to supported graphene. In: Appl. Phys. Lett., 2012, vol. 100, p. 193101.

[100] Kang K. et.al. Lifetimes of optical phonons in graphene and graphite by time-resolved incoherent anti-Stokes Raman scattering. In: Phys. Rev. B, 2010, vol. 81, 165405.

[101] Wang H. et.al. Ultrafast relaxation dynamics of hot optical phonons in graphene. In: Appl. Phys. Lett., 2010, vol. 96, p. 081917.

[102] Calizo I. et.al. Graphene-on-sapphire and graphene-on-glass: Raman spectroscopy study. In: Appl. Phys. Lett., 2007, vol. 91, p. 201904.

[103] Wang Z et.al. Brillouin scattering study of low-frequency bulk acoustic phonons in multilayer graphene. In: Carbon, 2008, vol. 46, p. 2133.

[104] Ma F. et.al. Strain effect on lattice vibration, heat capacity, and thermal conductivity of graphene. In: Appl. Phys. Lett., 2012, vol. 101, p. 111904.

[105] Wang L. and Li B. Thermal memory: A storage of phononic information. In: Phys. Rev. Lett., 2008, vol. 101, 267203.

[106] Lopes dos Santos J.M.B. et.al. Graphene bilayer with a twist: Electronic structure. In: Phys. Rev. Lett., 2007, vol. 99, 256802.

[107] Yan W. et.al. Angle-dependent van Hove singularities in a slightly twisted graphene bilayer. In: Phys. Rev. Lett., 2012, vol. 109, 126801.

[108] He R. et.al. Observation of low energy Raman modes in twisted bilayer graphene. In: Nano Letters, 2013, vol. 13, p. 3594-3601.

[109] Saha S. et.al. Phonons in few-layer graphene and interplanar interaction: A first principles study. In: Phys. Rev. B, 2008, vol. 78, 165421.

[110] Tan P. et.al. The shear mode of multilayer graphene. In: Nature Materials, 2012, vol. 11, p. 294.

[111] Electronic archive. New semiconductor materials, characteristics and properties. Ioffe Physico-Technical Institute. http://www.ioffe.ru/SVA/NSM/Semicond/Si/basic.html (visited 12.12.2014).

[112] Electronic archive. New semiconductor materials, characteristics and properties. Ioffe Physico-Technical Institute. http://www.ioffe.ru/SVA/NSM/Semicond/Si/mechanic.html (visited 12.12.2014).

[113] Gianozzi P. et.al. *Ab initio* calculation of phonon dispersions in semiconductors. In: Phys. Rev. B, 1991, vol. 43, p. 7231-7242.

[114] Patel C., Sherman W., Wilkinson G. Reinvestigation of the lattice dynamics of diamond on the basis of a Born-von Karman model. In: J. Phys. C: Solid State Phys., 1984, vol. 17, p. 6063-6070.

[115] Balandin A., Wang K. Significant decrease of the lattice thermal conductivity due to phonon confinement in a free-standing semiconductor quantum well. In: Phys. Rev. B, 1998, vol. 58, p. 1544-1549.

[116] Balandin A., Pokatilov E., Nika D. Phonon engineering in hetero- and nanostructures. In: J. Nanoelectron. Optoelectron., 2007, vol. 2, p. 140-170.

[117] Mingo N. Calculation of Si nanowire thermal conductivity using complete phonon dispersion relations. In: Phys. Rev. B, 2003, vol. 68, p. 113308.

[118] Nika D., Zincenco N., Pokatilov E. Engineering of Thermal Fluxes in Phonon Mismatched Heterostructures. In: J. Nanoelectron. Optoelectron., 2009, vol. 4, p. 180-185.

[119] Mingo N. et.al. Predicting the thermal conductivity of Si and Ge nanowires. In: Nano Lett., 2003, vol. 3, p. 1713-1716.

[120] Mingo N., Yang L. Phonon transport in nanowires coated with an amorphous material: An atomistic Green's function approach. In: Phys. Rev. B, 2003, vol. 68, p. 245406.

[121] Glassbrenner C., Slack G. Thermal Conductivity of Silicon and Germanium from 3°K to the Melting Point. In: Phys. Rev., 1964, vol. 134, p. A1058-A1069.

[122] Ziman J. Electrons and Phonons: The Theory of Transport Phenomena in Solids. New York: Oxford University Press, 1960. 554 p.

[123] Soffer S. Statistical Model for the Size Effect in Electrical Conduction. In: J. Appl. Phys., 1967, vol. 38, p. 1710-1715.

[124] Aksamija Z., Knezevic I. Anisotropy and boundary scattering in the lattice thermal conductivity of silicon nanomembranes. In: Phys. Rev. B, 2010, vol. 82, p. 045319.

[125] Nika D. et.al. Reduction of lattice thermal conductivity in one-dimensional quantum-dot superlattices due to phonon filtering. In: Phys. Rev. B, 2011, vol. 84, p. 165415.

[126] Liu W., Asheghi M. Thermal conduction in ultrathin pure and doped single-crystal silicon layers at high temperatures. In: J. Appl. Phys., 2005, vol. 98, p. 123523.

[127] Electronic archive. New semiconductor materials, characteristics and properties. Ioffe Physico-Technical Institute. http://www.ioffe.ru/SVA/NSM/Semicond/Ge/basic.html (visited 12.12.2014).

[128] Electronic archive. New semiconductor materials, characteristics and properties. Ioffe Physico-Technical Institute. http://www.ioffe.ru/SVA/NSM/Semicond/Ge/mechanic.html (visited 12.12.2014).

[129] Nilsson G., Nelin G. Phonon dispersion relations in Ge at 80 K. In: Phys. Rev. B, 1971, vol. 3, p. 364-369.

[130] Srivastava G. The physics of phonons. Bristol: Adam Hilger, 1990. 438 p.

[131] Lee S.-M., Cahill D., Venkatasubramanian R. Thermal conductivity of Si-Ge superlattices. In: Appl. Phys. Lett., 1997, vol. 70, p. 2957-2959.

[132] Sulka G., Brzozka A., Liu L. Fabrication of diameter-modulated and ultrathin porous nanowires in anodic aluminum oxide templates. In: Electrochemical Acta, 2011, vol. 56, p. 4972-4979.

[133] Zhou X. et.al. One-dimensional zigzag gallium nitride nanostructures. In: J. Appl. Phys., 2005, vol. 97, p. 104315.

[134] Caroff P. et.al. Controlled polytypic and twin-plane superlattices in III-V nanowires. In: Nat. Nanotechnol., 2009, vol. 4, p. 50-55.

[135] Fu L.-T. et.al. Fabrication and visible emission of single-crystal diameter-modulated gallium phosphide nanochains. In: J. Appl. Phys., 2010, vol. 107, p. 124321.

[136] Zhong Z. et.al. Periodic pillar structures by Si etching of multilayer GeSi/Si islands. In: Appl. Phys. Lett., 2005, vol. 87, p. 263102.

[137] Cahangirov S., Ciraci S. Confinement of electrons in size-modulated silicon nanowires. In: Phys. Rev. B, 2009, vol. 80, p. 075305.

[138] Cleland A., Schmidt D., Yung C. Thermal conductance of nanostructured phononic crystals. In: Phys. Rev. B, 2001, vol. 64, p. 172301.

[139] Zianni X. Diameter-modulated nanowires as candidates for high thermoelectric energy conversion efficiency. In: Appl. Phys. Lett., 2010, vol. 97, p. 233106.

[140] Zianni X. Efficient thermoelectric energy conversion on quasi-localized electron states in diameter modulated nanowires. In: Nanoscale Res. Lett., 2011, vol. 6, p. 286.

[141] Weber L., Gmelin E. Transport properties of silicon. In: Appl. Phys. A, 1991, vol. 53, p. 136-140.

[142] Martin P. et.al. Reduced thermal conductivity in nanoengineered rough Ge and GaAs nanowires. In: Nano Lett., 2010, vol. 10, p. 1120.

[143] Shelley M., Mostofi A. Prediction of high ZT in thermoelectric silicon nanowires with axial germanium heterostructures. In: Europhysics Letters, 2011, vol. 94, p. 67001.

[144] Hu M. et.al. Significant reduction of thermal conductivity in Si/Ge core-shell nanowires. In: Nano Lett., 2011, vol. 11, p. 618-623.

[145] Chen X., Wang Y., Ma Y. High thermoelectric performance of Ge/Si core-shell nanowires: First-principles prediction. In: J. Phys. Chem. C, 2010, vol. 114, p. 9096-9100.

[146] Peng X.-F., Chen K.-Q. Ballistic thermal transport in quantum wire modulated with two coupled quantum dots. In: Physica E, 2010, vol. 42, p. 1968-1972.

[147] Pokatilov E. et.al. Size-quantized oscillations of the electron mobility limited by the optical and confined acoustic phonons in the nanoscale heterostructures. In: J. Appl. Phys., 2007, vol. 102, p. 054304.

[148] Nika D., Pokatilov E. Balandin A. Phonon-engineered mobility enhancement in the acoustically mismatched silicon/diamond transistor channels. In: Appl. Phys. Lett., 2008, vol. 93, p. 173111.

[149] Wang J.-S., Wang J., Lu J. Quantum thermal transport in nanostructures. In: Eur. Phys. J. B, 2008, vol. 62, p. 381-404.

[150] Kundu A. et.al. Role of light and heavy embedded nanoparticles on the thermal conductivity of SiGe alloys. In: Phys. Rev. B, 2011, vol. 84, p. 125426.

[151] Volz S., Chen G. Molecular dynamics simulation of thermal conductivity of silicon nanowires. In: Appl. Phys. Lett., 1999, vol. 75, p. 2056-2058.

[152] Qiu B., Ruan X. Molecular dynamics simulation of lattice thermal conductivity of bismuth telluride using two-body interatomic potentials. In: Phys. Rev. B, 2009, vol. 80, p. 165203.

[153] Ladd A., Moran B., Hoover W. Lattice thermal conductivity: A comparison of molecular dynamics and anharmonic lattice dynamics. In: Phys. Rev. B, 1986, vol. 34, p. 5058-5064.

[154] Ward A., Broido D. Intrinsic phonon relaxation times from first-principles studies of the thermal conductivities of Si and Ge. In: Phys. Rev. B, 2010, vol. 81, p. 085205.

[155] Pokatilov E., Nika D., Balandin A. A phonon depletion effect in ultrathin heterostructures with acoustically mismatched layers. In: Appl. Phys. Lett., 2004, vol. 85, p. 825-827.

[156] Zincenco N. et.al. The size-quantized oscillations of the optical-phonon-limited electron mobility in AlN/GaN/AlN nanoscale heterostructures. In: J. Phys. Conf. Series, 2007, vol. 92, p. 012086.

[157] Bi K. et.al. The thermal conductivity of SiGe heterostructure nanowires with different cores and shells. In: Phys. Lett. A, 2012, vol. 376, p. 2668-2671.

[158] Wingert M. et.al. Thermal conductivity of Ge and Ge-Si core-shell nanowires in the phonon confinement regime. In: Nano Lett., 2011, vol. 11, p. 5507-5513.

[159] Crismari D., Nika D. Thermal conductivity reduction in Si/Ge core/shell nanowires. In: J. Nanoelectron. Optoelectron., 2012, vol. 7, p. 701-705.

[160] Aksamija Z., Knezevic I. Lattice thermal conductivity of graphene nanoribbons: Anisotropy and edge roughness scattering. In: Appl. Phys. Lett., 2011, vol. 98, p. 141919.

[161] Ramayya E. et.al. Electron transport in silicon nanowires: The role of acoustic phonon confinement and surface roughness scattering. In: J. Appl. Phys., 2008, vol. 104, p. 063711.

[162] Jin S., Fischetti M., Tang T-W. Modeling of electron mobility in gated silicon nanowires at room temperature: Surface roughness scattering, dielectric screening, and band nonparabolicity. In: J. Appl. Phys., 2007, vol. 102, p. 083715.

[163] Pokatilov E., Nika D., Balandin A., Confined electron – confined phonon scattering rates in wurtzite AlN/GaN/AlN heterostructures. In: J. Appl. Phys., 2004, vol. 95, p. 5626.

[164] Davydov A. Theory of solids. Moscow: Nauka, 1980. 646 p.

[165] Nika D. et.al. Thermal conductivity inhibition in phonon engineered core-shell cross-section modulated Si/Ge nanowires. In: Appl. Phys. Lett., 2013, vol. 102, p. 213109.

[166] Nair R. et.al. Fine structure constant defines visual transparency of graphene. In: Science, 2008, vol. 320, p. 1308.

[167] Mak K., Shan J., Heinz T. Seeing many-body effects in single- and few-layer graphene: Observation of two-dimensional saddle-point excitons. In: Phys. Rev. Lett., 2011, vol. 106, p. 046401.

[168] Gilje S. et.al. A chemical route to graphene for device applications. In: Nano Lett., 2007, vol. 7, p. 3394-3398.

[169] Ang P. et.al. Solution-gated epitaxial graphene as pH sensor. In: J. Am. Chem. Soc., 2008, vol. 130, p. 14392-14393.

[170] Liang M., Luo B., Zhi L. Application of graphene and graphene-based materials in clean energy-related devices. In: Int. J. Energy Res., 2009, vol. 33, p. 1161-1170.

[171] Bunch J. et.al. Electromechanical resonators from graphene sheets. In: Science, 2007, vol. 315, p. 490-493.

[172] Balandin A. Thermal properties of graphene and nanostructured carbon materials. In: Nature Mater., 2011, vol. 10, p. 569-581.

[173] Nika D., Balandin A. Two-dimensional phonon transport in graphene. In: J. Phys.: Cond. Matter., 2012, vol. 24, p. 233203.

[174] Balandin A., Nika D. Phononics in low-dimensional materials. In: Materials Today, 2012, vol. 15, p. 266-275.

[175] Latil S., Henrard L. Charge carriers in few-layer graphene films. In: Phys. Rev. Lett., 2006, vol. 97, p. 036803.

[176] Maultzsch J. et.al. Phonon dispersion in graphite. In: Phys. Rev. Lett., 2004, vol. 92, p. 075501.

[177] Mohr M. et.al. Phonon dispersion of graphite by inelastic x-ray scattering. In: Phys. Rev. B, 2007, vol. 76, p. 035439.

[178] Carozo V. et.al. Raman signature of graphene superlattices. In: Nano Lett., 2011, vol. 11, p. 4527-4534.

[179] Wirtz L., Rubio A. The phonon dispersion of graphite revisited. In: Solid State Commun., 2004, vol. 131, p. 141-152.

[180] Lifshitz I. On the thermal properties of chain and layered structures at low temperatures. In: Zh. Eksp. Teor. Fiz. 22, 475 (1952). (in Russian)

[181] Ferrari A. et.al. Raman spectrum of graphene and graphene layers. In: Phys. Rev. Lett., 2006, vol. 97, p. 187401.

[182] Gupta A. et.al. Raman scattering from high-frequency phonons in supported n-graphene layer films. In: Nano Lett., 2006, vol. 6, p. 2667-2673.

[183] Graf D. et.al. Spatially resolved Raman spectroscopy of single- and few-layer graphene. In: Nano Lett., 2007, vol. 7, p. 238-242.

[184] Lui C., Heinz T. Measurement of layer breathing mode vibrations in few-layer graphene. In: Phys. Rev. B, 2012, vol. 87, p. 121404(R).

[185] Mounet N., Marzari N. First-principles determination of the structural, vibrational and thermodynamic properties of diamond, graphite, and derivatives. In: Phys. Rev. B, 2005, vol. 71, p. 205214.

[186] Cai W. et.al. Thermal transport in suspended and supported monolayer graphene grown by chemical vapor deposition. In: Nano Lett., 2010, vol. 10, p. 1645-1651.

[187] Lindsay L., Broido D., Mingo N. Flexural phonons and thermal transport in multilayer graphene and graphite. In: Phys. Rev. B, 2011, vol. 83, p. 235428.

[188] Zhang H., Lee G., Cho K. Thermal transport in graphene and effects of vacancy defects. In: Phys. Rev. B, 2011, vol. 84, p. 115460.

[189] Nika D., Askerov A., Balandin A. Anomalous size dependence of the thermal conductivity of graphene ribbons. In: Nano Lett., 2012, vol. 12, p. 3238-3244.

[190] Poncharal P. et.al. Raman spectra of misoriented bilayer graphene. In: Phys. Rev. B, 2008, vol. 78, p. 113407.

[191] Hass J. et.al. Why multilayer graphene on 4H-SiC(0001) behaves like a single sheet of graphene. In: Phys. Rev. Lett., 2008, vol. 100, p. 125504.

[192] Luican A. et.al. Single-layer behavior and its breakdown in twisted graphene layers. In: Phys. Rev. Lett., 2011, vol. 106, p. 126802.

[193] Havener R. et.al. Angle-resolved Raman imaging of interlayer rotations and interactions in twisted bilayer graphene. In: Nano Lett., 2012, vol. 12, p. 3162-3167.

[194] Latil S., Meunier V., Henrard L. Massless fermions in multilayer graphitic systems with misoriented layers: Ab initio calculations and experimental fingerprints. In: Phys. Rev. B, 2007, vol. 76, p. 201402(R).

[195] Shallcross S., Sharma S., Pankratov O. Quantum interference at the twist boundary in graphene. In: Phys. Rev. Lett., 2008, vol. 101, p. 056803.

[196] Nika D., Cocemasov A., Balandin A. Specific heat of twisted bilayer graphene: Engineering phonons by atomic plane rotations. In: Appl. Phys. Lett., 2014, vol. 105, p. 031904.

[197] Nihira T., Iwata T. Temperature dependence of lattice vibrations and analysis of the specific heat of graphite. In: Phys. Rev. B, 2003, vol. 68, p. 134305.

[198] Popov V. Low-temperature specific heat of nanotube systems. In: Phys. Rev. B, 2002, vol. 66, p. 153408.

[199] Alofi A., Srivastava G. Thermal conductivity of graphene and graphite. In: J. Appl. Phys., 2012, vol. 112, p. 013517.

[200] Li H. et.al. Thermal conductivity of twisted bilayer graphene. In: Nanoscale, 2014, vol. 6, p. 13402-13408.

## Declarația privind asumarea răspunderii

Subsemnatul, declar pe răspundere personală că materialele prezentate în teza de doctorat sunt rezultatul propriilor cercetări și realizări științifice. Conștientizez că, în caz contrar, urmează să suport consecințele în conformitate cu legislația în vigoare.

Cocemasov Alexandr

Semnătura

Data

# CURRICULUM VITAE

**Name**: Cocemasov Alexandr

**Date of birth**: February 12, 1987

**Place of birth**: Chisinau, Republic of Moldova

**Citizenship**: Republic of Moldova

**Education:**

| | |
|---|---|
| 2010-2013 | PhD studies, Moldova State University, Department of Theoretical Physics, Specialty: Theoretical Physics. |
| 2008-2010 | Master studies, Moldova State University, Faculty of Physics, Specialty: Theoretical Physics. |
| 2004-2010 | Licentiate studies, Moldova State University, Faculty of Physics, Specialty: Physics and Informatics. |

**Internships:**

- NanoDevice Laboratory, University of California – Riverside, Riverside, CA, USA, February – March, 2015.
- Institute for Integrative Nanosciences, IFW, Dresden, Germany, September, 2013.
- III Higher Courses of CIS for young scientists, post-graduate and graduate students on advanced methods of research in nanosystems and materials (SYN-nano-2010), Joint Institute for Nuclear Research, Dubna, Russian Federation, July, 2010; Russian Scientific Center "Kurchatov Institute", Moscow, Russian Federation, July, 2010.

**Research interests:**

- Theory of acoustic, vibrational and thermal properties of nanostructures: quantum wells, wires, dots, superlattices and graphene.
- Numerical simulations and modeling of physical phenomena.
- Lattice dynamics and molecular dynamics models for different crystalline materials.

**Professional activity:**

| | |
|---|---|
| 2010-present | Scientific Researcher, E. Pokatilov Laboratory of Physics and Engineering of Nanomaterials, Moldova State University. |
| 2008-2010 | Engineer, E. Pokatilov Laboratory of Physics and Engineering of Nanomaterials, Moldova State University. |

**Participation in scientific projects:**

| | |
|---|---|
| 2014-2015 | Moldova State project for young researchers: 14.819.16.02F. |
| 2014-2015 | Moldova-STCU international project: 14.820.18.02.012 STCU.A/5937. |
| 2012-2013 | Moldova State project for young researchers: 12.819.05.18F. |
| 2011-2014 | Moldova State institutional project: 11.817.05.10F. |
| 2010-2011 | Moldova State project for young researchers: 10.819.05.02F. |
| 2008-2009 | Moldova-Russia bilateral project: 08.820.05.29RF. |

**Participation at conferences:**

- DPG Spring Meeting, Dresden, Germany, 2014.
- Lomonosov-2013, Moscow, Russia, 2013.
- 14-th International Conference on Modern Information and Electronic Technologies “MIET-2013”, Odesa, Ukraine, 2013.
- CECAM-Workshop: Nanophononics, University of Bremen, Bremen, Germany, 2013.
- 2012 EMN Open Access Week, Chengdu, China, 2012.
- Conference of Moldovan Physicists „CFM-2012”, Balti, Moldova, 2012.
- Lomonosov-2012, Moscow, Russia, 2012.
- 76th Annual Meeting of the DPG and DPG Spring Meeting, Berlin, 2012.
- 13-th International Conference on Modern Information and Electronic Technologies “MIET-2012”, Odesa, Ukraine, 2012.
- I-st All-Russian Congress of Young Scientists, Saint-Petersburg, Russia, 2012.
- 9th European Conference on Thermoelectrics, Thessaloniki, Greece, 2011.
- International Conference of Young Researchers, Chisinau, Republic of Moldova, editions 2009, 2010, 2011 and 2012.

**Scientific publications:** 11 research articles (including 6 in ISI journals) and 22 abstracts at national and international conferences.

**Honors, awards and scholarships:**

- Municipal Youth Award for Science (Physics), Chisinau, 2014.
- Excellence Scholarship of the Government of the Republic of Moldova, 2013.
- DAAD Scholarship for Young Researchers, Dresden, Germany, 2013.
- Award “For outstanding performances in the field of science and technology”, Ministry of Youth and Sports of the Republic of Moldova, 2013.
- National Scholarship of the World Federation of Scientists, Geneva, Switzerland, 2012.
- I-st, II-nd and III-rd Places at Moldova State University Scientific Conference Competitions 2010, 2009 and 2008.

**Knowledge of languages:**
Russian (native), Romanian (good), English (good).

**Contacts:**

| | |
|---|---|
| Address | A. Mateevici str. 60, bl. 4a, of. 216, Chisinau, MD-2009, Republic of Moldova. |
| Phone | (+373) 22 577712, (+373) 67 318183. |
| E-mail | kocemasov@live.ru |